Search for the $^{12}C(p,^{5}Li)^{8}Be$ Reaction at 38 MeV

by

Philip Y. W. Yee

May, 1977

A Thesis

Submitted to the Faculty of Graduate Studies

In Partial Fulfilment of the Requirements for

the Degree of Master of Science

Physics Department

University of Manitoba

Winnipeg, Manitoba

"SEARCH FOR

THE $^{12}C(p,^{5}Li)^{8}Be$ REACTION

AT 38 MeV"

by

PHILIP Y.W. YEE

A dissertation submitted to the Faculty of Graduate Studies of the University of Manitoba in partial fulfillment of the requirements of the degree of

MASTER OF SCIENCE

Abstract

The $^{12}C(p,^{5}Li)^{8}Be$ reaction has been studied at an incident proton energy of 38 MeV at three ^{5}Li angles. The protons and alpha particles coming from the breakup of ^{5}Li particles were detected in coincidence, the protons in a plastic scintillator, the alpha particles in a barrier detector telescope. The reaction was first studied using a Monte Carlo technique to simulate the experiment and in particular to calculate the efficiency of the detection system. The light collection efficiency of plastic scintillator was also studied for the proton detection system of this experiment so as to determine the effect of using various detector geometries. The $^{12}C(p,^{5}Li)^{8}Be$ reaction was then investigated experimentally by observing the proton and the alpha particle in coincidence from the breakup of the ^{5}Li. The upper limits on the cross section for ^{5}Li outgoing angles of 39°, 46°, and 54° for this reaction have been obtained.

Acknowledgements

The author is indebted to the participants of this project for their assistance and suggestions. These include Drs.M.Canty, N.Davison, P.Debenham, W.Falk, and J.Watson, and Mr. S.P.Kwan.

The continual guidance and encouragement offered by Dr. N.E.Davison for this project is also gratefully acknowledged.

Contents

List of Figures

List of Tables

I. Introduction

Light nuclei often seem to consist of two or more groups or clusters of nucleons. For nuclei with Z=N and A=4n (n=1,2, 3,...), the binding energy of an extra nucleon is often large compared to the binding energy of an extra alpha particle. In nuclei with A=4n+1, on the other hand, relatively small binding energies are found for single nucleons. These facts and the well known stability of the free alpha particle led to the cluster model. Within the framework of this cluster representation (SHE60, WIL58, WIL66) the shell-model wave functions can be written in cluster form, and the various clusters treated as single particles in a shell model calculation. Many of the results of this cluster model are identical with those derived from the usual shell model. Theoretical investigations (MAT63, BAL64, KUD65, BAL65, NEU65) have shown that even without residual interactions the independent particle model predicts large four nucleon parentages when the spins of these nucleons are coupled to a total spin $J^{\pi}=0^{+}$, thus justifying to some extent the basic approach of the cluster model.

Several experimental approaches have been used to investigate cluster phenomena in nuclei, but one of the most fruitful has been transfer reactions. Among the more important transfer reactions are direct reactions such as the " knock-out " reactions: $(p,p\alpha)$ (BAL64,

JAM63,SAK65, BER65, EPS71) and (α,2α) (SAK65, BER65, IGO63, DON64, BAU65) ; " pick-up " reactions such as (p,α) (CRA66), (p,^{6}Li) (BRA71), (d,^{6}Li) (DEN63, GEM64, DAE64, EIC70, DAE66, DEN65, DEN66, DRA71, MCG71), (d,^{7}Li) (DEN67), (d,^{7}Be) (DEN67), (α,^{5}He) (PIR74), (α,^{8}B) (BRO65), and (^{3}He,^{7}Be) (JAY68),and "stripping" reactions such as (^{7}Li,t) (BET67,MID68). In particular, the (d,^{6}Li) reactions have been widely used to obtain quantitative information about alpha particle clustering in nuclei. Since ^{6}Li has a large width for decay into an alpha particle and a deuteron (WIL66), the (d,^{6}Li) reactions selectively excite levels derived from the target by removal of an alpha particle-like cluster. In fact, the (d,^{6}Li) angular distributions exhibit features of direct reactions, and are amenable to analysis within the framework of the DWBA theory where the transfered alpha particle is assumed to be a single entity or " lump " particle.

In the present work the analogous (p,^{5}Li) reaction is considered. In particular, an attempt has been made to study the ^{12}C(p,^{5}Li)^{8}Be reaction. As ^{5}Li decays rapidly, the ^{12}C(p,^{5}Li)^{8}Be reaction has some unique features which are challenging. The ^{5}Li breaks up into an alpha particle and a proton in about 10^{-21} second; the ^{5}Li internal wavefunction has $J^{\pi}=3/2^{-}$, and the L=1 motion of the proton and the alpha particle necessitates finite

range calculations. Unlike recent experiments such as (p,^{5}He) and (α,^{5}He) (PIR74) which involve the detection of a neutron and an alpha particle in coincidence, the (p,^{5}Li) reaction involves the detection of a proton and an alpha particle in coincidence. Due to the large background of elastically scattered protons from the target, the (p,^{5}Li) reaction is experimentally more difficult. Finally with a ^{12}C target there is a large cross section for a four body final state consisting of a proton and three alpha particles. This makes the the detection of the (p,^{5}Li) reaction still more difficult.

The present work on the ^{12}C(p,^{5}Li)^{8}Be reaction involved the measurement of upper limits on the differential cross section at three angles at an incident proton energy of 38.23 MeV. In Chapter II are found discussions on kinematics, phase space, and the constraints on DWBA analysis for this reaction. Chapter III gives the design principles of the experimental apparatus including a description of the Monte Carlo calculations of light collection efficiency in plastic scintillators and simulation of the coincidence detection of the proton and alpha particle from the ^{5}Li breakup. Chapter IV describes the experiment. The layout of the cyclotron and the scattering chamber are briefly shown. The detection system and electronics are discussed in detail. Experimental procedure and data acquisition are also

included in this chapter. Chapter V gives the analysis of the data and the results. In the analysis, various projections of the data onto different axes are shown and discussed. From these projections the upper limits of the cross sections are obtained. The error associated with this upper limit is also discussed. Finally an outline of possible improvements in the experiment ends the thesis.

II. Theory

II.1 Kinematics

The following notations are adopted throughout this thesis for a reaction of the type

$$a+b \longrightarrow 1+2+3+4+\ldots+n \qquad \text{(Fig.2.1)}$$

E = total energy of the system

E_i = total energy of particle i

T_i = kinetic energy of particle i

M_i = rest mass of particle i

P_i = three-momentum of particle i

θ_i = polar angle of particle i

ϕ_i = azimuthal angle of particle i

Whenever any of these quantities is expressed in the centre of mass system, it will be denoted by a prime. The speed of light c is assumed to be unity, so that the rest energy of particle i can be written as M_i.

If the rest masses of all the particles are known, the final state is specified by n three-momentum vectors for a total of 3n kinematic variables. Since energy and momentum conservation provide four relations between these 3n quantities, the final state is completely determined if 3n-4 kinematic variables are measured. Such an experiment is called a kinematically complete experiment. In a particle-particle correlation experiment with two particles detected, the variables deter-

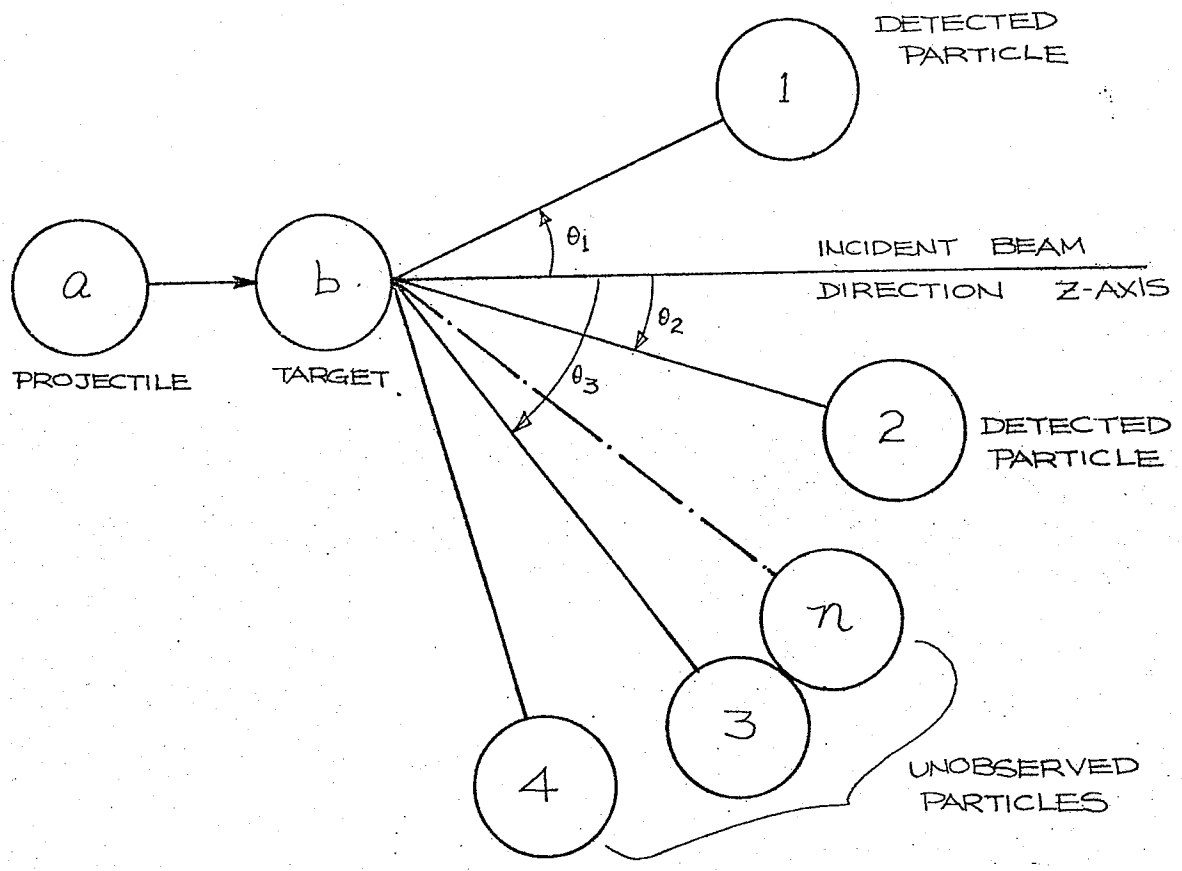

E = total energy of the system
E_i = total energy of particle i
T_i = kinetic energy of particle i
M_i = rest mass of particle i
P_i = three momentum of particle i
θ_i = polar angle of particle i
Φ_i = azimuthal angle of particle i

Fig.2.1 Convention adopted for the reaction
a+b $\longrightarrow$ 1+2+3+...+n

mined are usually the polar angles θ_1 and θ_2, the azimuthal angles ϕ_1 and ϕ_2, and the kinetic energies T_1 and T_2.

For a three body final state reaction the system is overdetermined when the above six variables are measured. In practice an overdetermination is used to discriminate between double valued solutions and to reduce background. For a four body final state reaction, however, a completly determined system requires 8 measurements. Thus, if only two of the particles are observed, the experiment is kinematically incomplete. The allowed events will form then a continuum in a T_1 vs T_2 plot with boundaries which follow directly from momentum and energy conservation (VAN73) :

$$\vec{P}_a + \vec{P}_b = \vec{P}_1 + \vec{P}_2 + \vec{P}_3 + \vec{P}_4 = \vec{P} \qquad (2.1)$$

and $$E_a + E_b = E_1 + E_2 + E_3 + E_4 = E \qquad (2.2)$$

Here $\vec{P}$ and E are the total momentum and energy. The $^5Li+^8Be$ system in fact can be treated as a resonance in a four body final state. Both ^5Li and ^8Be have short lifetimes of the order of about 10^{-21} seconds and 10^{-16} seconds respectively. The ^5Li breaks up into a proton and an alpha particle, while the ^8Be yields two alpha particles. However, if the ^5Li and ^8Be are considered as single entities for a brief period, then the $^5Li+^8Be$ system can be treated as a resonance as is dicussed in the following paragraphs.

If all the unobserved particles are emitted in the same direction with the same velocity, then the allowed events lie on the boundary of the four body continuum in the T_1 vs T_2 plane. This boundary can be shown to be the same as the locus of the kinematically allowed events for a three body final state in which the rest mass of the third particle is equal to the sum of the rest masses of the unobserved particle. The extremum of E_2 is then given by the solution of $A(E_2)=0$ with:

$$A(E_2) = (E-E_1-E_2)^2 - (\vec{P}-\vec{P}_3-\vec{P}_4)^2 - \left(\sum_{i=3}^{4} M_i\right)^2 \qquad (2.3)$$

Letting $\hat{P}_2$ be the extremum of $|\vec{P}_2|$, the solution is (VAN73):

$$E_2 = \frac{-BC \pm D\left[B^2 - m_2^2(c^2-D^2)\right]^{1/2}}{C^2-D^2}$$

where $B = W^2 - V^2 + m_2^2 - (m_3+m_4)^2$

$C = -2W$

$D = 2V\cos\alpha$ with $V = |\vec{V}|$

and $W = E-E_1$ $\qquad \vec{V} = \vec{P}-\vec{P}_1$

$$\alpha = \cos^{-1}\left[\frac{(\vec{P}-\vec{P}_1)\cdot\hat{P}_2}{|\vec{P}-\vec{P}_1|}\right]$$

For any reaction, the physically allowed events must satisfy the condition $P_2 \geq 0$ (or $E_2 \geq M_2$). The kinematically allowed range of values for $|P_1|$, given $\hat{P}_1$ and $\hat{P}_2$, (the extrema of $|P_1|$ and $|P_2|$), follows from the conservation of energy and momentum. The mimimum value of P_1 appears

when particle 2 and the centre of mass of particle 3 and 4 are emitted antiparallel with equal momenta. Obviously in this case P_1 has the value zero. The maximum momentum is obtained when the other three particles are emitted parallel to each other with the same velocity opposite to particle 1. This condition corresponds to:

$$B^2-M^2(C^2-D^2)\geq 0 \qquad (2.4)$$

This function can be solved easily by numerical methods, although it is a complicated function in E_1 and in general, cannot be solved analytically for E_1.

If there is a resonance, or if one "lump particle" exists in the four body final state, the reaction becomes a three body final state reaction. If there are two pairs of resonating particles, two body kinematic calculations can be applied. Fig.2.2 shows the four body continuum boundary for the $^{12}C(p,p\alpha)\alpha\alpha$ reaction along with the three body $^{12}C(p,p\alpha)^8Be$ kinematic locus and the range of T_p and T_α allowed in a two body calculation for $^{12}C(p,^5Li)^8Be$, the proton and alpha particle coming from the ^5Li breakup. The ranges of T_p and T_α for the two body case are discussed in the following chapter.

Fig.2.2

Boundary of the four body final state continuum, the three body final state locus, and the two body final state region associated with 38 MeV proton bombardment of ^{12}C. The finite size of the two body region is due to the mass uncertainty of ^{5}Li. The resulting uncertainty in Q-value of the $^{12}C(p,^{5}Li)^{8}Be$ reaction causes a spread in the outgoing ^{5}Li energies. In addition the angle of breakup of the ^{5}Li with respect to the direction of motion of the ^{5}Li causes a spread in proton and alpha particle energies. Since the breakup Q value of ^{8}Be is only 90 Kev, on this plot the three body locus is indistinguishable from the four body continuum boundary.

T_α vs T_p

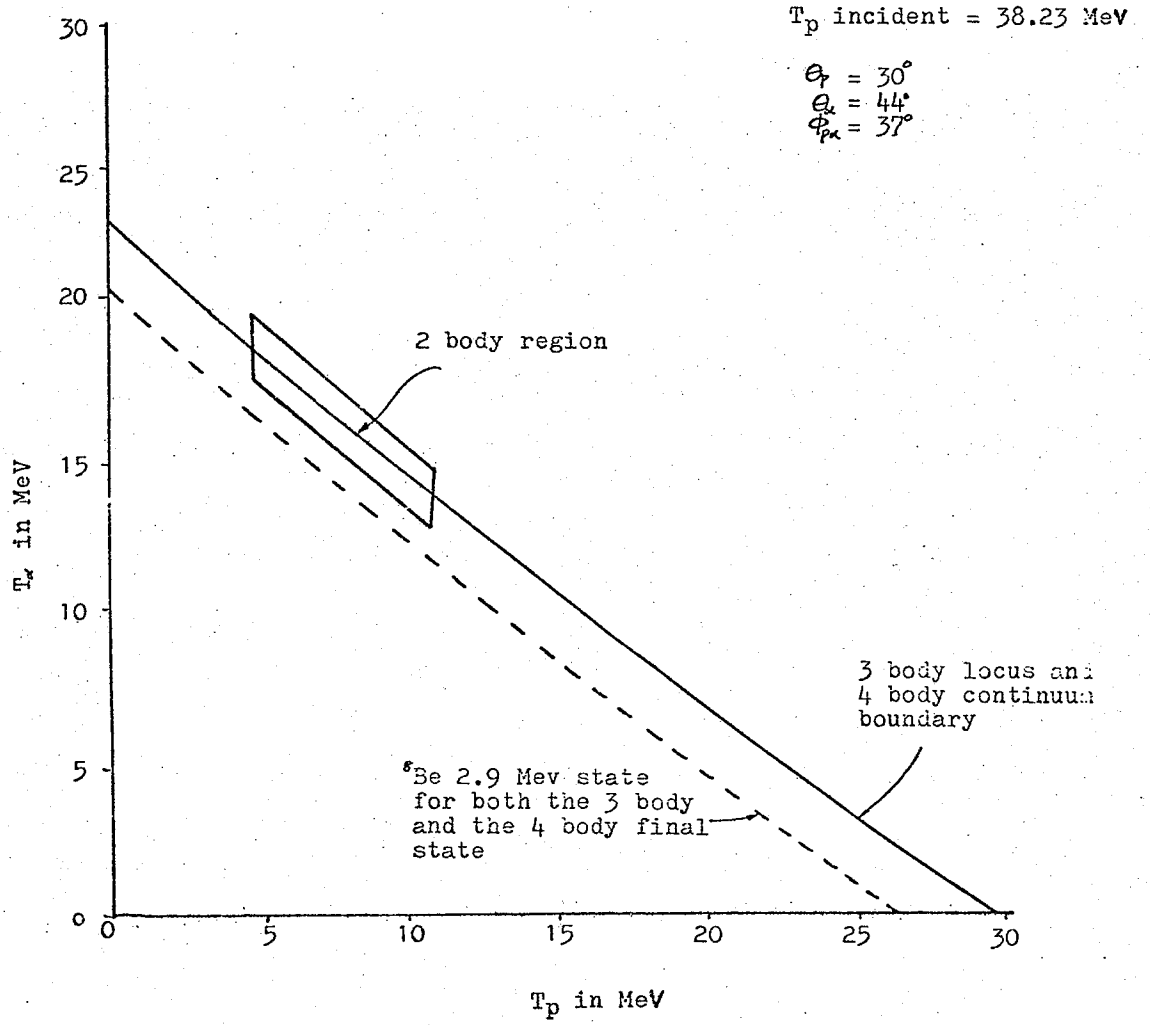
T_p incident = 38.23 MeV
$\theta_7 = 30°$
$\theta_\alpha = 44°$
$\phi_{p\alpha} = 37°$
2 body region
3 body locus and 4 body continuum boundary
^{6}Be 2.9 Mev state for both the 3 body and the 4 body final state
T_α in MeV
T_p in MeV
0
5
10
15
20
25
30

II.2 PHASE SPACE

II.2.a Introduction

The probability of obtaining a specific final state in a nuclear reaction is determined by two factors: the kinematic factor and the dynamic factor. The dynamic factor is the square of the matrix element for the reaction. According to the usual formalism for the dynamics of a nuclear reaction, the transition probability from an initial state with $\vec{P}_a$ and $\vec{P}_b$ to a final state with momenta $\vec{P}_1 \ldots \vec{P}_n$ is obtained from a matrix element:

$$T = \langle \vec{P}_1, \vec{P}_n | H' | \vec{P}_a, \vec{P}_b \rangle \qquad (2.7)$$

The matrix element contains all possible information concerning the application of the perturbation H' to the system under consideration. This matrix element T will be discussed in detail in section II.3.b of this chapter.

The kinematic factor is a phase space density (phase space for short). To extract information about the matrix element or about the final state interactions of particles produced in the reaction, it is necessary to know the effects of phase space limitations.

The total phase space volume available to a reaction is determined by the kinematics of the reaction through the phase space requirements of momentum and energy conservation. Physically it represents the statistical

probability of an event yielding a state with the ith particle in the momentum range dP_i. If T is independent of the momentum variables, the phase space distribution alone will determine the distribution of events for that reaction.

The relationship of the dynamic factor and kinematic factor to the cross section can be seen from Fermi's golden rule number 2. The probability per unit time that the reaction a+b $\longrightarrow$ 1+2+3+...+n will take place can be expressed (FER50) as:

$$W = \frac{2\pi}{\hbar} |\langle \psi_f | H' | \psi_i \rangle|^2 F \qquad (2.8)$$

where ψ_i and ψ_f are the initial and final state wave functions respectively, and $\langle \psi_f | H' | \psi_i \rangle$ is the matrix element T for the transition from i to f caused by a perturbation H' of the Hamiltonian. The factor F is the phase space factor.

Equation (2.8) can be expressed in two different ways :

$$W = \frac{2\pi}{\hbar} |T'|^2 \rho(E) \qquad (2.9)$$

and $$W = \frac{2\pi}{\hbar} |T''|^2 R(E) \qquad (2.10)$$

The matrix element T' in equation (2.9) is not invariant under a Lorentz Transformation but T" in equation (2.10) is. Since W is the same for both equations, it follows that the phase space factor $\rho(E)$ is

non-invariant while R(E) is invariant under a Lorentz transformation. Throughout this thesis only the invariant phase space R(E) is used. In the following section the phase space factor is derived. The derivation of this factor follows that given in reference (NYB68).

II.2.b The Definition and General Formula for the Phase Space Density

For one particle, a definite state of motion, with specified position (x,y,z) and momentum (P_x, P_y, P_z) can be represented as a point in a six dimensional phase space. Conversely each point in phase space corresponds to a definite state of motion of the particle.

Classically there are no limits on the density of the representation points: a given value of x can be combined with any value of P_x. It is also possible in principle to measure x and P_x simultaneously with infinite accuracy and localize a point in phase space. Thus classically there is an infinite number of points available in phase space for a particle confined to a certain region in configuration space and with a certain energy. However quantum mechanics requires the representation points to be separated by finite distances. The uncertainty principle states that it is impossible to

measure position and momentum simultaneously with accuracy better than

$$\Delta x_i \, \Delta P_i = 2\pi\hbar$$

Therefore a state of motion can only be given with this indefiniteness and corresponds in phase space to a finite volume or elementary cell of size $(2\pi\hbar)$.

The number of final states N_1 available to one particle therefore is finite and equal to the total volume of the phase space divided by the size of the elementary cell:

$$N_1 = \frac{1}{(2\pi\hbar)^3}\int dx\,dy\,dz\,dP_x\,dP_y\,dP_z$$

$$= \frac{1}{(2\pi\hbar)^3}\int d^3x\,d^3P \qquad (2.11)$$

If the particle is confined to a volume V, then

$$N_1 = \frac{V}{(2\pi\hbar)^3}\int d^3P$$

with $$V = \int d^3x \qquad (2.12)$$

For a particle of mass M and with total energy less than or equal to E, N_1 will be the number of cells in a volume enclosed in momentum space by the sphere:

$$P_x^2 + P_y^2 + P_z^2 = E^2 - M^2 \qquad (2.13)$$

Given the total number of states, the density of states in phase space can be defined as the number of states per unit energy interval ;

$$\rho_1(E) = \frac{dN_1}{dE} \qquad (2.14)$$

The extension to a system of n particles each of which has energy ≤E can be made simply. The total number of states N_n will be the product of the number of final states for each particle, thus;

$$N_n = \left[\frac{1}{(2\pi\hbar)^3}\right]^n \int_{x_i} \int_{P_i} \prod_{i=1}^{n} d^3x_i d^3P_i \tag{2.15}$$

Since all particles are assumed to be confined to the same geometric volume V, then

$$N_n = \left[\frac{V}{(2\pi\hbar)^3}\right]^n \prod_{i=1}^{n} (2S_i+1) \int_{P_i} \prod_{i=1}^{n} d^3P_i \tag{2.16}$$

This formula gives the number of cells available to the final state of a system of n particles with particle i having spin S_i. The phase space density of states for n particles can be written as

$$\rho_n(E) = \frac{dN_n}{dE} = \frac{d}{dE}\left\{\left[\frac{V}{(2\pi\hbar)^3}\right]^n \prod_{i=1}^{n}(2S_i+1) \int \prod_{i=1}^{n} d^3P_i\right\} \tag{2.17}$$

The conservation of momentum and energy have to be considered. The conservation of momentum is given by

$$\sum_{i=1}^{n} \vec{P}_i - \vec{P} = 0 \tag{2.18}$$

and the conservation of energy by

$$\sum_{i=1}^{n} E_i - E = 0 \tag{2.19}$$

With the introduction of the δ-function, these requirements can be included in equation (2.17). The properties of these δ-functions are

$$\int d^3P_m \, \delta^3\left(\vec{P}_m - \left(\vec{P} - \sum_{i=1}^{n-1} \vec{P}_i\right)\right) = 1, \tag{2.20}$$

and for energy conservation:

$$\int \delta\left(\sum_{i=1}^{n} E_i - E\right) dE = 1 . \tag{2.21}$$

With the introduction of equations (2.20) and (2.21) into equation (2.16), the number of states, N_m, then becomes

$$N_m = \prod_{i=1}^{n} (2S_i + 1) \int dE \prod_{i=1}^{n} d^3P_i \, \delta^3\left(\sum_{i=1}^{n} \vec{P}_i - \vec{P}\right) \delta\left(\sum_{i=1}^{n} E_i - E\right)$$

and equation (2.17) becomes:

$$\rho_{n(E)} = \prod_{i=1}^{n} (2S_i + 1) \int \prod_{i=1}^{n} d^3P_i \, \delta^3\left(\sum_{i=1}^{n} \vec{P}_i - \vec{P}\right) \delta\left(\sum_{i=1}^{n} E_i - E\right) \tag{2.22}$$

This formula is the non-invariant phase space, and is symmetric in all the n particles. In addition, the requirements of energy and momentum conservation are explicitly given. However equation (2.22) is not invariant under Lorentz Transformations. The simplest way to make equation (2.22) invariant is to replace d^3P_i in equation (2.22) by $d^3P_i / 2E_i$ (NYB68). This gives the general phase space formula:

$$R_{n(E)} = \prod_{i=1}^{n} (2S_i + 1) \int \prod_{i=1}^{n} \frac{d^3P_i}{2E_i} \, \delta^3\left(\sum_{i=1}^{n} \vec{P}_i - \vec{P}\right) \delta\left(\sum_{i=1}^{n} E_i - E\right) \tag{2.23}$$

which is invariant under Lorentz Transformations. The factor $2E_i$ enters from a normalization of the wave function in field theory.

Equation (2.23) can be evaluated fairly easily for three body and four body final states. The three body phase space density can be written as:

$$R_3 = \prod_{i=1}^{n}(2S_i+1)\int \frac{d^3P_1}{2E_1}\frac{d^3P_2}{2E_2}\frac{d^3P_3}{2E_3}$$
$$\delta(E_1+E_2+E_3-E)\,\delta^3(\vec{P}-\vec{P}_1-\vec{P}-\vec{P}_3) \qquad (2.24)$$

and can be simplied to the form (NYB68):

$$R_3 \propto \int dT_1 dT_2$$

or $$dR_3 \propto dT_1 dT_2 \qquad (2.24b)$$

where T_i is the kinetic energy of the ith particle. Expression (2.24b) shows that the number of states of the three body final state is proportional to the area in a T_1 vs T_2 plot.

From equation (2.23) the four body phase space density becomes:

$$R_4 = \prod_{i=1}^{n}(2S_i+1)\int \frac{d^3P_1}{2E_1}\frac{d^3P_2}{2E_2}\frac{d^3P_3}{2E_3}\frac{d^3P_4}{2E_4}$$
$$\delta(E_1+E_2+E_3+E_4-E)\,\delta^3(\vec{P}-\vec{P}_1-\vec{P}_2-\vec{P}_3-\vec{P}_4) \qquad (2.25)$$

This can be simplied to the form

$$\frac{dR_4}{dT_1 dT_2} \propto \int \frac{P_3 E_3 dT_3}{E-E_1-E_2-E_3} \quad . \qquad (2.26)$$

II.3 The Distorted Wave Born Approximation (DWBA)

Although no analysis was done using DWBA in the present work, the DWBA approach and its prediction on the cross section will be discussed in this section.

II.3.a Introduction

Equation (2.8) gives Fermi's "Golden Rule no. 2":

$$W = \frac{2\pi}{\hbar} |\langle \psi_f | H' | \psi_i \rangle|^2 F \qquad (2.8)$$

where $\langle \psi_f | H' | \psi_i \rangle = T$ is the nuclear matrix element.

For reactions of the type A(a,b)B, F is given by (SCH68):

$$F = \frac{\mu_b L^3}{8\pi^2\hbar^3} k_b \, d\Omega_b \qquad (2.27)$$

where $d\Omega_b$ is the infinitesimal element of solid angle associated with the direction $\vec{k}_b$, L^3 is the initial volume, and μ_b is the reduced mass in the exit channel.

The quantity W obtained by substitution of equation (2.27) into equation (2.8) is the probability of scattering into solid angle $d\Omega_b$ per unit time when there is initially one system in the volume L^3. A single system in L^3 corresponds to an incident flux V_a/L^3 per unit area and time, where V_a is the initial relative speed of a and A. Since the differential scattering cross section $d\sigma$ is defined as the probability per unit incident flux, then

$$d\sigma = \frac{WL^3}{V_a} \qquad (2.28)$$

When equations (2.8) and (2.27) are substituted into (2.28) using $k_a = \frac{\mu_a v_a}{\hbar}$

the differential cross section is found to be

$$\frac{d\sigma}{d\Omega} = \frac{\mu_a \mu_b L^6}{4\pi^2 \hbar^4} \frac{k_b}{k_a} \sum_1 |T_{ba}|^2 \qquad (2.29)$$

where μ_a and μ_b are reduced masses in the entrance and exit channels. The sum is over the magnetic quantum numbers M_A, M_B, m_a, m_b. If spin and total angular momentum as well as antisymmetrization are taken into consideration, the differential cross section becomes ;

$$\frac{d\sigma}{d\Omega} = \frac{\mu_a \mu_b L^6}{4\pi^2 \hbar^4} \left(\frac{k_b}{k_a}\right)\left(\frac{N_b}{N_a}\right)(2J_A+1)^{-1}(2S_a+1) \sum_{\substack{M_A M_B \\ m_a m_b}} |T_{ab}|^2 \qquad (2.30)$$

where J_A is the total angular momentum of the target nucleus A, and S_a is the spin of the incident particle. The antisymmetrization factor (N_b/N_a) is inserted into equation (2.30) to account for the number of equivalent arrangements of nucleons in the entrance and exit channels. N_a, the total number of permutations in the entrance channel, is given by

$$N_a = \frac{(n_a + n_A)!}{n_a!\, n_A!} \qquad (2.31)$$

and is obtained by dividing the number of permutations of all kinds by the number internal to a and the number

internal to A. N_b is defined in a similar way.

II.3.b The Nuclear Matrix Element

The Hamiltonian for the system A(a,b)B is

$$H = H_a + H_A + T_{aA} + V_{aA}$$
$$= H_b + H_B + T_{bB} + V_{bB}$$

where T_{aA}, T_{bB} are the kinetic energy operators for the relative motion of the particles in the entrance and exit channels, H_i is the internal Hamiltonian for particle i and V_{ij} is the total interaction between particles i and j.

The transition matrix element in the DWBA can then be written as (JAC70):

$$T = \langle \chi_b^- \phi_b \Phi_B \mid V_{aA} - U_{aA} \mid \chi_a^+ \phi_a \Phi_A \rangle \qquad (2.32)$$

where U_{aA} is the optical potential for elastic scattering in the entrance channel, $\phi_a, \phi_b, \Phi_A, \Phi_B$, are the eigenstates of H_a, H_b etc; and the $\chi^{\pm}$ are the distorted wavefunctions of relative motion for particles a and b. Thus for the initial state

$$H_A \Phi_A = \varepsilon_A \Phi_A \ , \quad H_a \phi_a = \varepsilon_a \phi_a \qquad (2.33)$$

$$(T_{aA} + U_{aA}) \chi_a^+ = (E - \varepsilon_a - \varepsilon_A) \chi_a^+ \qquad (2.34)$$

where ε_i are the eigenvalues for H , and E is the total energy. The equations for the final state are similar to the above equations. If a cluster of x nucleons is picked up as in Fig.2.3, the total interaction V_{aA} can be written as the sum:

$$V_{aA} = V_{aB} + V_{ax} \tag{2.35}$$

where A = B+x

The matrix element can then be written as

$$T = \langle \chi_b^- \phi_b \Phi_B | V_{ax} + (V_{aB} - U_{aA}) | \chi_a^+ \phi_a \Phi_A \rangle \tag{2.36}$$

Usually it is assumed that the matrix element of $(V_{aB} - U_{aA})$ is zero (SAT64). This is based on the argument that the elastic effects of V_{aB} are largely contained in U_{aA} while the inelastic effects are small. This assumption is probably most valid for heavy nuclei.

The matrix element in equation (2.36) can be further evaluated by introducing coordinates explicitly. Since it is assumed that the only coordinate dependence of the potential V_{aA} is on the relative coordinates, it is useful to use only relative coordinates in evaluating T. Using α and β to denote the entrance and exit channels respectively, one can define the relative coordinates r_α and r_β to be

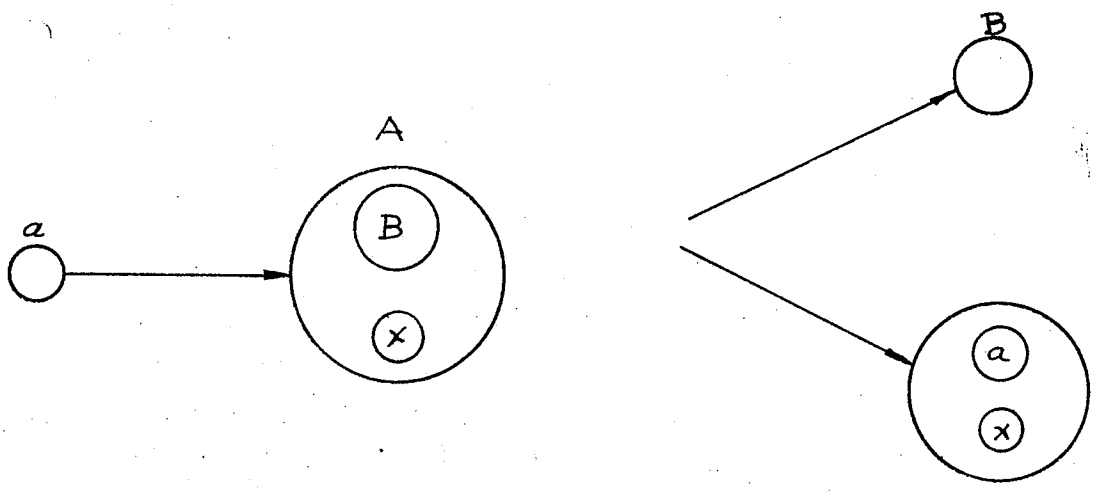

Fig.2.3

A cluster of x nucleons is picked up by the incident particle a in a pickup reaction.

$$\vec{r}_\alpha = \vec{r}_a - \vec{r}_A \tag{2.37}$$

$$\vec{r}_\beta = \vec{r}_b - \vec{r}_B \tag{2.38}$$

The distorted wave amplitude becomes (AUS64)

$$T_{\alpha\beta} = \mathcal{J} \int d^3r_\alpha \int d^3r_\beta \, \chi^{-*}_\beta(\vec{k}_\beta, \vec{r}_\beta) \langle B,b|V|A,a\rangle \chi^{+}_\alpha(\vec{k}_\alpha, \vec{r}_\alpha) \tag{2.39}$$

where $\langle B,b|V|A,a\rangle = \langle \Phi_B \phi_b | V_{aA} - U_{aA} | \Phi_A \phi_a \rangle$

In the expression for $T_{\alpha\beta}$, $\mathcal{J}$ is the Jacobian of the transformation from fixed coordinates to the relative coordinates r_α and r_β as shown in Fig.2.4. The bra-ket notation is used to signify intergration over all coordinates independent of r_α and r_β. The nuclear matrix element $T_{\alpha\beta}$ is a function of r_α and r_β, and plays the role of an effective and in general nonlocal interaction for the transition between the distorted waves χ^{+}_α and χ^{-}_β. It contains all the information on the nuclear structure, on angular momentum selection rules, and the type of reaction being considered.

The nuclear matrix element of equation (2.39) can be expanded into a series of multipoles each of which corresponds to the transfer to the target nucleus of a definite angular momentum j composed of an orbital part l and a spin part s. If the projectiles a and b have

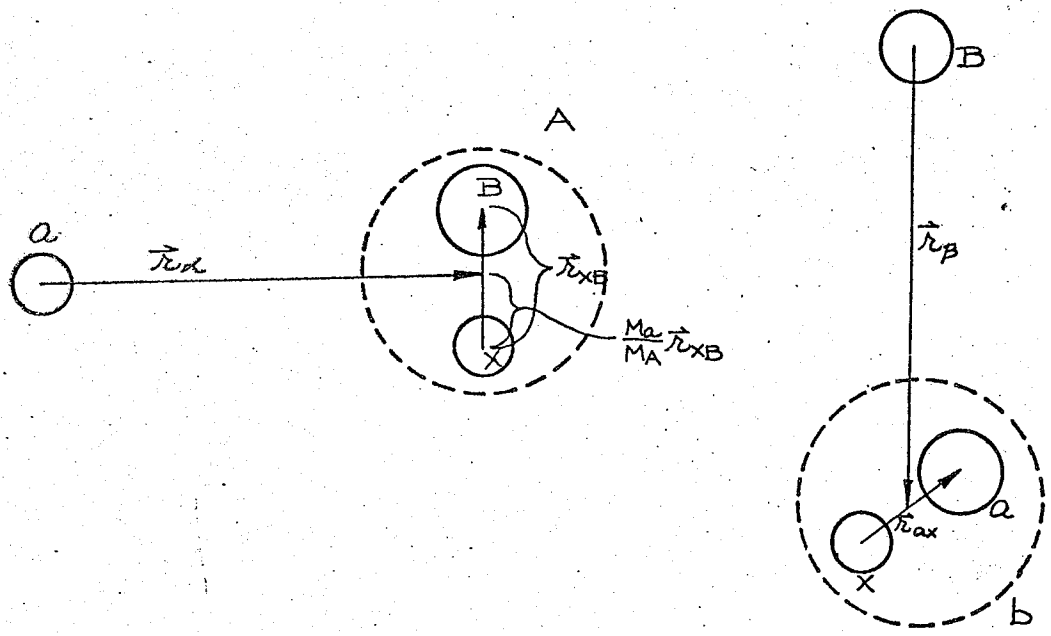

Fig.2.4

The relative coordinates of the particles participating in a pickup reaction. The entrance channel is denoted by α, while the exit channel is denoted by β.

definite spin S_a and S_b, and if the target and residual nuclear spins are J_A and J_B respectively, the transferred angular momentum can be defined to be:

$$\vec{J}=\vec{J}_B-\vec{J}_A\,,\quad \vec{s}=\vec{S}_a-\vec{S}_b\,,\quad \vec{l}=\vec{j}-\vec{s} \tag{2.40}$$

The multipole series may then be written with Clebsch-Gordan coefficients, corresponding to the vector coupling in (2.40), so that the matrix element becomes:

$$\begin{aligned}
&\mathcal{J}\,\langle J_B M_B, S_b m_b \mid V \mid J_A M_A, S_a m_a\rangle \\
&= \sum_{lsj} i^{-l}\, G_{lsj,m}(\vec{r}_\beta,\vec{r}_\alpha\,;\,bB,aA) \\
&\times(-1)^{S_b-m_b}\langle J_A j\,;M_A, M_B-M_A \mid J_B M_B\rangle \\
&\times\langle S_a S_b\,;m_a,-m_b\mid s, m_a-m_b\rangle \\
&\times\langle ls\,;m, m_a-m_b\mid j, M_B-M_A\rangle
\end{aligned} \tag{2.41}$$

where $m=M_B+m_b-M_A-m_a$, and $\mathcal{J}$ is the Jacobian of the transformation to the relative coordinates as in equation (2.39). The multipole operator, $G_{lsj,m}$, expresses definite angular momentum l transfer. Each of these multipoles can be expanded into a sum of multipoles in charge space, that also express definite isospin transfer. Each G then becomes a sum of terms:

$$\langle T_A t\ M_{T_A}\ m_t \mid T_B M_{T_B}\rangle\langle t_b t\ m_{t_b}\ m_t \mid t_a m_{t_a}\rangle$$

corresponding to the transfer of the isospin t in analogy with equation (2.40). The multipole operator, $G_{lsj,m}$, may be explicitly displayed by the inverted form of the above expansion:

$$G_{\ell s j,m} = i^{\ell}\left(\frac{2\ell+1}{2J_B+1}\right)\sum_{\substack{M_A M_B \\ m_a m_b}} \ell \langle J_B M_B, S_b m_b | V | J_A M_A, S_a m_a \rangle$$
$$\times (-1)^{S_b m_b} \langle J_A j; M_A, M_B - M_A | J_B M_B \rangle$$
$$\times \langle S_a S_b ; m_a - m_b | S, m_a - m_b \rangle$$
$$\times \langle \ell s ; m, m_a - m_b | j, M_B - M_A \rangle \qquad (2.42)$$

The factor i^{ℓ} is to ensure convenient time-reversal properties. By its construction $G_{\ell s j,m}$ is seen to transform under rotation of the coordinate system like the spherical harmonic Y_{ℓ}^{m}.

It is often helpful to write $G_{\ell s j,m}$ as a product of two factors,

$$G_{\ell s j,m}(\vec{r}_\beta, \vec{r}_\alpha) = A_{\ell s j}\, f_{\ell s j,m}(\vec{r}_\beta, \vec{r}_\alpha) \qquad (2.43)$$

$A_{\ell s j}$ is the spectroscopic coefficient which includes such quantities as fractional parentage coefficients for the initial or the final nuclear states and the interaction strength, while $f_{\ell s j,m}$ is the form factor. The form factor by definition is a function expressing the structure of the nucleus. The form factor is determined on the basis of a given model and adjusted to give the best measure of agreement with the experimental data. The form factor $f_{\ell s j,m}$ is proportional to the magnitude of the interaction V_{aA} and to the internal wavefunction of the transferred nucleon. The physical meaning of $f_{\ell s j,m}$ will become apparent in the following section.

With the introduction of equations(2.41) and (2.43) into equation (2.39) the distorted wave amplitude reduces to a sum over multipole contributions:

$$T_{\beta\alpha} = \sum_{lsj} (2l+1)^{\frac{1}{2}} A_{lsj} (-1)^{S_b - m_b} \langle J_A j; M_A, M_B - M_A | J_B M_B \rangle$$
$$\times \langle l s, m, m_a - m_b | j, m - m_b + m_a \rangle$$
$$\times \langle S_a S_b ; m_a, -m_b | s, m_a - m_b \rangle \beta_{sj}^{lm} \qquad (2.44)$$

where the reduced amplitude β_{sj}^{lm} is defined as

$$(2l+1)^{\frac{1}{2}} i^l \beta_{sj}^{lm} = \int d^3R_\alpha \int d^3R_\beta \chi_\beta^{-*}(\vec{k}_\beta, \vec{R}_\beta) f_{lsj,m}(\vec{R}_\beta, \vec{R}_\alpha)$$
$$\chi_\alpha^{+}(\vec{k}_\alpha, \vec{R}_\alpha) \qquad (2.45)$$

II.3.c The Zero-Range Approximation

Equation (2.45) presents calculational difficulties for reactions involving any sort of rearrangement. The presence of different variables in the two channels prevents easy reduction of the integral, and therefore equation (2.45) is difficult to evaluate. In most current distorted wave calculations the above difficulty is removed by the assumption that the form factor is of very small range, either because it is proportional to an interaction that has a small range, or either because the internal wavefunctions of one or more of the projectiles have small ranges. This zero-range assumption has the physical meaning that the light particle in channel β is emitted at the same point that the light particle in

channel α is absorbed. For the reaction involving transfer of particle x with:

$$B-A = x = a-b$$

the zero-range assumption thus implies

$$\vec{r}_a = \vec{r}_b = \vec{r}_x$$

and $$\vec{R}_\beta = \vec{R}_b - \vec{R}_B$$

$$= \vec{R}_a - \frac{M_A \vec{R}_A + M_x \vec{R}_a}{M_A + M_x}$$

$$= \frac{M_A}{M_B} \vec{r}_\alpha$$

where $M_B = M_A + M_x$ and is the mass of particle B.

The form factor then can be written as

$$f^{ZERO}_{lsj,m}(\vec{r}_\alpha) = \delta(\vec{r}_\beta - \frac{M_A}{M_B}\vec{r}_\alpha) \int f_{lsj,m}(\vec{r}_\beta + \frac{M_A}{M_B}\vec{r}_\alpha, \vec{r}_\alpha)\, d^3r_\beta$$

$$= F_{lsj}(\vec{r}_\alpha)\, Y^{m*}_l(\hat{r}_\alpha)\, \delta(\vec{r}_\beta - \frac{M_A}{M_B}\vec{r}_\alpha) \qquad (2.45b)$$

where $\hat{r}_\alpha = \vec{r}_\alpha / |r_\alpha|$ is the unit vector and therefore indicates the scattering angle. As a result, equation (2.45) reduces to the zero-range expression:

$$(2l+1)^{1/2} i^l \beta^{lm}_{sj} \approx \int d^3r\, \chi^{-*}_\beta(\vec{k}_\beta, \frac{M_A}{M_B}\vec{r})\, F_{lsj}(\vec{r})\, Y^{m*}_l(\hat{r})\, \chi^{+}_\alpha(\vec{k}_\alpha, \vec{r}) \qquad (2.46)$$

where $\vec{r} = \vec{r}_\alpha$, which is considerably easier to evaluate.

Many computer codes have been constructed to evaluate equation (2.46) numerically. The distorted waves in equation (2.46) are usually in the form of partial wave expansions:

$$\chi_\beta^+ = \frac{4\pi}{k_\beta r_\beta} \sum_{\ell m} i^\ell e^{i\sigma_\ell} f_{\beta\ell}(\vec{k}_\beta, \vec{r}_\beta) Y_\ell^m(\hat{r}_\beta) Y_\ell^{m*}(\theta,\phi) \qquad (2.47)$$

and

$$\chi_\beta^{-*}(\vec{k}_\beta, \vec{r}'_\beta) = \frac{4\pi}{k_\beta r_\beta} \sum_{\ell m} i^{-\ell} e^{-i\sigma_\ell} f_{\beta\ell}(\vec{k}_\beta, \vec{r}'_\beta) Y_\ell^m(\hat{k}_\beta) Y_\ell^m(\hat{r}'_\beta) \qquad (2.48)$$

The angles θ, ϕ indicate the direction of $\vec{k}_\beta$ with respect to the coordinate axes. The radial functions $f_{\beta\ell}$ are required to vanish at $\vec{r}_\beta = 0$ in order that χ_β^+ be regular. The unit vectors $\hat{k}_\beta$ and $\hat{r}'_\beta$ are defined as $\vec{k}_\beta / |k_\beta|$ and $\vec{r}'_\beta / |r'_\beta|$.

The angular integrations of equation (2.46) are done analytically, yielding

$$\beta_{sj}^{\ell m} = \sum_{L_\alpha L_\beta M_\alpha M_\beta} i^{L_\alpha - L_\beta - \ell} e^{i\sigma_{\alpha L_\alpha} + i\sigma_{\beta L_\beta}} \left[\frac{4\pi(2L_\beta+1)}{(2L_\alpha+1)}\right]^{1/2} I_{L_\beta L_\alpha}^{\ell s j} \langle L_\beta \ell; 00 | L_\alpha 0\rangle \langle L_\beta \ell; M_\beta m | L_\alpha M_\alpha\rangle Y_{L_\beta}^{M_\beta}(\hat{k}_\beta) Y_{L_\alpha}^{M_\alpha *}(\hat{k}_\alpha) \qquad (2.49)$$

where

$$I_{L_\beta L_\alpha}^{\ell s j} = \frac{M_B}{M_A} \frac{4\pi}{k_\alpha k_\beta} \int_0^\infty F_{\ell s j}(r) f_{\beta L_\beta}(\vec{k}_\beta, \frac{M_A}{M_B} r) f_{\alpha L_\alpha}(\vec{k}_\alpha, \vec{r}_\alpha) dr \qquad (2.50)$$

The radial integrals $I_{L_\beta L_\alpha}^{\ell s j}$ are obtained by numerical integration of equation (2.50) using radial wavefunctions $f_{\beta L_\beta}$ and $f_{\alpha L_\alpha}$ that have been computed by numerical integration of the optical model radial Schrödinger equations in channels α and β.

One quantity that affects the magnitude of the radial integral in equation (2.50) is the change of linear

momentum, $k_\beta \rightarrow k_\alpha$. The zero-range form factor $F_{lsj}(\vec{r})$ is derived from the overlap of bound state wavefunctions. Because these tend to have small momenta, the form factor tends to be a slowly-varying function of r. Therefore the values of the radial integral(2.50) are dominated by the radial distorted waves $f_{\beta L_\beta}$ and $f_{\alpha L_\alpha}$. This overlap is reduced if the momenta k_α and k_β are very different, for then the distorted waves oscillate at very different rates and the overlap averages to a small value. To yield large cross section, a reaction must provide good momentum matching, with $k_\alpha \approx k_\beta$.

Angular momentum matching also plays a role in the radial integrals. The wavefunction of each partial wave tends to have its largest maximum near the classical turning point. Therefore best overlap in equation(2.50) is obtained if the first maxima of the two radial waves coincide. This occurs if

$$\frac{L_\alpha}{k_\alpha} \approx \frac{L_\beta}{k_\beta}$$

If conditions of the reaction yield $k_\alpha \approx k_\beta$ then $L_\alpha \approx L_\beta$ is favored; therefore small values of angular momentum transfer are favored.

The DWBA formalism can also be applied to multinucleon transfer reactions, and the cross section can then be calculated as before using

$$\frac{d\sigma}{d\Omega} = \frac{\mu_\alpha \mu_\beta L^6}{(2\pi\hbar^2)^2}\left(\frac{k_\beta}{k_\alpha}\right)\left(\frac{N_\beta}{N_\alpha}\right)(2J_A+1)^{-1}(2S_a+1)^{-1}\sum_{\substack{M_A M_B \\ m_a m_b}}|T_{\alpha\beta}|^2 \qquad (2.30)$$

Because the spin projections are displayed explicitly in equation(2.44) the sums in equation(2.30) can easily be performed with the result that

$$\frac{d\sigma}{d\Omega} = \frac{\mu_\alpha \mu_\beta L^6}{(2\pi\hbar^2)^2}\left(\frac{k_\beta}{k_\alpha}\right)\left(\frac{N_\beta}{N_\alpha}\right)\frac{(2J_B+1)}{(2J_A+1)(2S_a+1)}\sum_{\ell s_j}\left\{|A_{\ell s j}|^2\sum_m|\beta_{s_j}^{\ell m}|^2\right\}$$

(2.30b)

With the zero-range approximation for the reduced amplitude, $\beta_{s_j}^{\ell m}$ is given by equation(2.49).

Thus with suitable wave functions and interaction potentials the theoretical values of the cross sections can be obtained for different nuclear models, and these cross sections then can be compared with those obtained from experiments.

II.3.d The Application of the DWBA to the (p,^{5}Li) System

Although no DWBA analysis has been attempted in the present work, the application of the DWBA to the ^{12}C(p, ^{5}Li)^{8}Be reaction is briefly considered here. In the calculation of the zero-range approximation it was shown that in order to have large cross sections, the reaction must provide good momentum matching such that $k_\alpha \approx k_\beta$. Although the zero-range approximation is not valid for the (p,^{5}Li) reactions the conclusions regarding momentum

Fig.2.5

The energy levels of ^{5}Li. Energy values are plotted vertically in MeV, based on the ground state as zero. Values of total angular momentum J, parity, and isobaric spin T which appear to be reasonably well established are indicated on the levels.

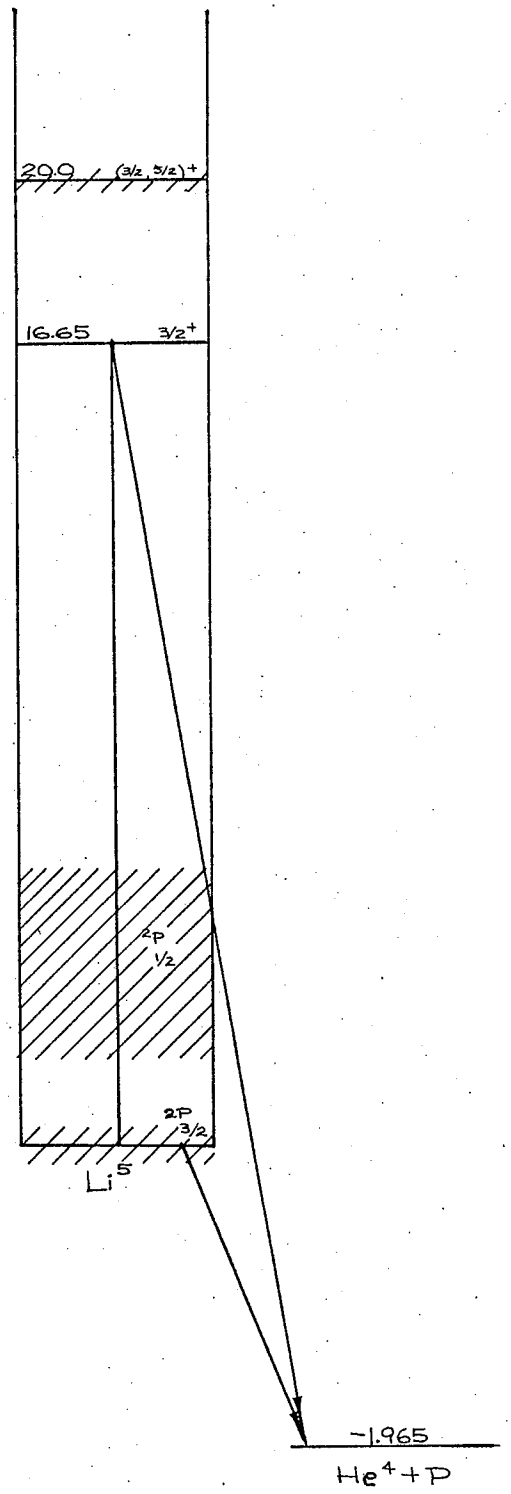
20.9
(3/2, 3/2)+
16.65
3/2+
2P 1/2
2P 3/2
Li5
-1.965
He4+P

and angular momentum mismatch are still largely valid. In the present work, with incident proton energy of 38.23 MeV and an outgoing ^{5}Li energy of 22.6 MeV (at $\theta_{^5Li}=39^o$), the ratio of the linear momenta of the proton and ^{5}Li is about 2. The ratio of the momenta is thus not ideal.

It is also known that small values of angular momentum transfer favor large cross sections. The ground state of ^{5}Li has $J^\pi=3/2^-$, while the ground state of ^{8}Be has zero spin. Since the proton has spin s=1/2, the angular momentum transfer l is restricted to

$$J+s>l>|J-s|$$

This gives l=1 or 2 while parity restrictions eliminate l=1.

The P-state wave function of ^{5}Li in its ground state prevents the application of zero-range DWBA. This is due to the fact that a P-state gives zero amplitude at short range while the zero range approximation places all the interaction strength at zero range. This suggests that the analysis of (p,^{5}Li) has to done by using the finite-range approximation. In the following paragraphs the finite-range approximation will be obtained.

The exact numerical procedure for the finite-range integration of equation (2.45) is done by performing as many integrations as possible before the distorted waves are brought into the calculation. Because the distorted waves in equations (2.47) and (2.48) are to be handled in

spherical harmonic expansion, it is obvious that the angular integrations in equation (2.45) can all be made to precede the integration over the radial wavefunctions of the distorted waves. The calculation thus has two stages. (1) All integrals that involve internal variables of the form factor or that involve angles of r_α and r_β are performed. (2) The double radial integral with respect to r_α, r_β is performed.

The first stage of the calculation is carried through by expanding the form factor in a double series of spherical harmonics. Because $f_{\ell s j,m}$ transforms under rotations like Y_ℓ^m, this series takes the form

$$f_{\ell s j,m} = \sum_{L_\alpha L_\beta M} F^{\ell s j}_{L_\beta L_\alpha}(\vec{r}_\beta,\vec{r}_\alpha)\, Y^{M*}_{L_\beta}(\hat{r}_\beta)\, Y^{(m-M)*}_{L_\alpha}(\hat{r}_\alpha)\, \langle L_\beta L_\alpha; M, m-M \mid \ell m\rangle$$

Equation (2.45) thus becomes

$$\beta^{\ell m}_{sj} = \frac{(4\pi)^{3/2}}{k_\alpha k_\beta} \sum_{L_\alpha L_\beta} i^{L_\alpha + L_\beta - 1}\, e^{i\sigma_{L_\alpha} + i\sigma_{L_\beta}}\, I^{\ell s j}_{L_\beta L_\alpha} \langle L_\beta \ell; m, -m \mid L_\alpha 0\rangle\, Y^{-m}_{L_\beta}(\Theta, 0)$$

where the z-axis is taken along $\vec{k}_\alpha$, the y-axis is along $\vec{k}_\alpha \times \vec{k}_\beta$ and Θ is the angle between $\vec{k}_\alpha$ and $\vec{k}_\beta$. The radial integrals $I^{\ell s j}_{L_\beta L_\alpha}$ are

$$I^{\ell s j}_{L_\beta L_\alpha} = \int_0^\infty r_\alpha^2 dr_\alpha \int_0^\infty r_\beta^2 dr_\beta\, f_{\beta L_\beta}(k_\beta, r_\beta)\, F^{\ell s j}_{L_\beta L_\alpha}(\vec{r}_\beta,\vec{r}_\alpha)\, f_{\alpha L_\alpha}(\vec{k}_\alpha,\vec{r}_\alpha)$$

where $F^{\ell s j}_{L_\beta L_\alpha}$ is the coefficent as defined in equation (2.45b). The second stage involves the calculation of the double integral $I^{\ell s j}_{L_\beta L_\alpha}$. This is done by numerical methods.

The overall calculation of the finite-range DWBA thus requires the numerical evaluation of one set of

single integrals and of one set of double integrals. The distorted wavefunctions only enter in the double integral.

III. Design Principles for Experimental Apparatus

III.1 The design of the Apparatus

The design of the experimental set up is based on the assumption that the $^{12}C(p,^{5}Li)^{8}Be$ has initially only two bodies in the final state. The incident proton is assumed to approach the ^{12}C nucleus and to capture an alpha particle to form a ^{5}Li nucleus. However because of its short lifetime the ^{5}Li quickly breaks up into a proton and an alpha particle. Relative to the ^{5}Li direction, the maximum angle of the alpha particle is around 8.5° while that of the proton is around 31° for the present experimental conditions. These angles are obtained from a kinematic calculation which will be discussed later in this section. For a given ^{5}Li direction, the associated alpha particle will fall into a cone with opening angle of roughly 17° (Fig.3.1a). The intensity of the alpha particle distribution is expected to be peaked near the edge of this cone assuming that the ^{5}Li breaks up isotropically in its centre of mass.

The experimental set up, which will be discussed in detail in the next chapter, closely followed this reaction model. A proton detector was placed in the same horizontal plane as the target while the alpha particle detector was placed at an angle θ directly above (Fig.3.1b). Since the alpha particles from the ^{5}Li breakup were

Fig.3.1a

The directions of ^{5}Li, proton, and alpha particle. With a given ^{5}Li direction both the proton and the alpha particle from the breakup of ^{5}Li go out in a cone of 62° and 17° respectively for incident proton energy of 38 MeV.

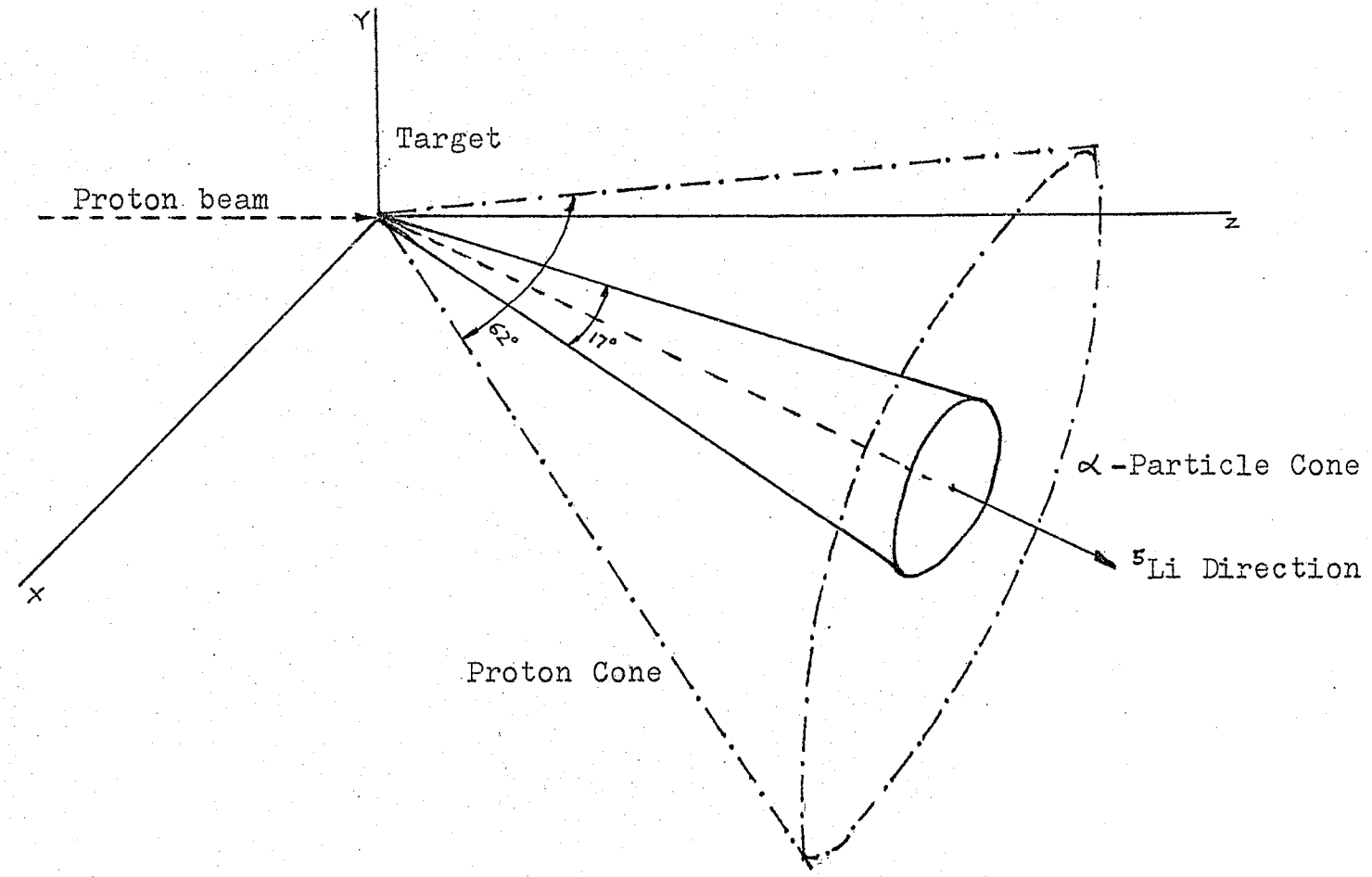
Y
Target
Proton beam
Z
X
62°
17°
α-Particle Cone
5Li Direction
Proton Cone

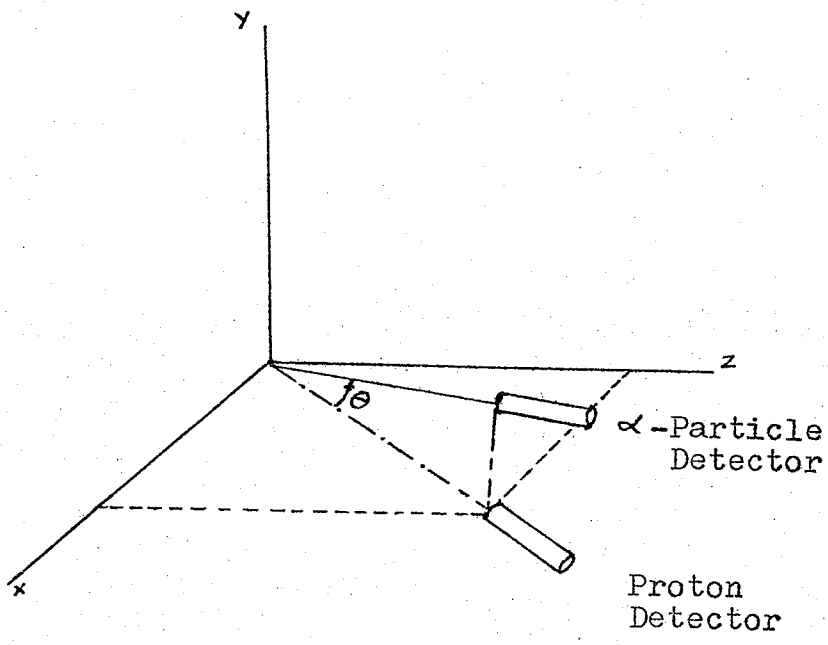

Fig.3.1b

The alpha particle detector is placed at an angle θ directly above the proton detector.

produced in a 17° cone, the alpha particle detector intercepted only a portion of the alpha particles. Moreover, the alpha particles were not uniformly distributed within this cone. A Monte Carlo program was written to simulate the kinematics of the reaction and the ^{5}Li breakup and to estimate the local densities of the correlated alpha particle and proton in their allowed cones. From these results the efficiency of the detection system could be calculated. The Monte Carlo technique is outlined in the Appendix. In the remainder of this section, the approach to writing the program and the results obtained are discussed.

The Monte Carlo program was written to simulate the kinematics of the experiment. In the two body reaction $^{12}C(p,^{5}Li)^{8}Be$ the energy of the outgoing ^{5}Li can be determined from two body kinematics. In the case of an incident proton energy of 38.23MeV and with the proton detector at 30°, the ^{5}Li has an energy of 22.6MeV in the laboratory frame to within the uncertainty due to the spread in the ^{5}Li mass. The ^{8}Be, which also has a short lifetime, goes out in the opposite direction at about 105° with energy of 6.3 MeV in the laboratory frame, and it breaks up into two alpha particles in 10^{-16} second. In order to simplify the Monte Carlo calculation, the following assumptions were made:

(1) The incident proton beam was monoenergetic and

parallel.

(2) The beam spot was assumed to be a single point located at the centre of the target.

(3) The target was very thin so that the energy loss of the alpha particles or of the protons passing through the target was negligible.

(4) The $^{12}C(p,^{5}Li)^{8}Be$ reaction in the $p+^{12}C$ centre of mass frame was assumed to be isotropic.

(5) The breakup of the ^{5}Li was assumed to be isotropic in its centre of mass frame.

Throughout the program the random number generator subroutine RANDU, which is a standard IBM subroutine, was used to generate random numbers. Fig.(3.2) shows the configuration and coordinates used in this program. In this figure the Z-axis is the beam direction. The $p+^{12}C$ frame (Fig.3.2a) is defined as the centre of mass frame for the $p+^{12}C$ system. The ^{5}Li rest frame (Fig.3.2b) is defined as the frame in which ^{5}Li is at rest. The following symbols are used for the coordinates of the ^{5}Li, alpha particle, and proton:

For the ^{5}Li:

$\psi_{^{5}Li}$ is the polar angle of ^{5}Li in the laboratory frame.

$\psi'_{^{5}Li}$ is the corresponding polar angle of ^{5}Li in the $p+^{12}C$ centre of mass frame (C.M. for short)

$\phi_{^{5}Li}$ is the azimuthal angle of ^{5}Li in the laboratory

Fig.3.2a

The coordinate system used in the Monte Carlo calculation. This frame is referred to as the $p+^{12}C$ frame in the text.

Fig.3.2b

The breakup coordinates of ^{5}Li. This is referred to as the ^{5}Li rest frame in the text.

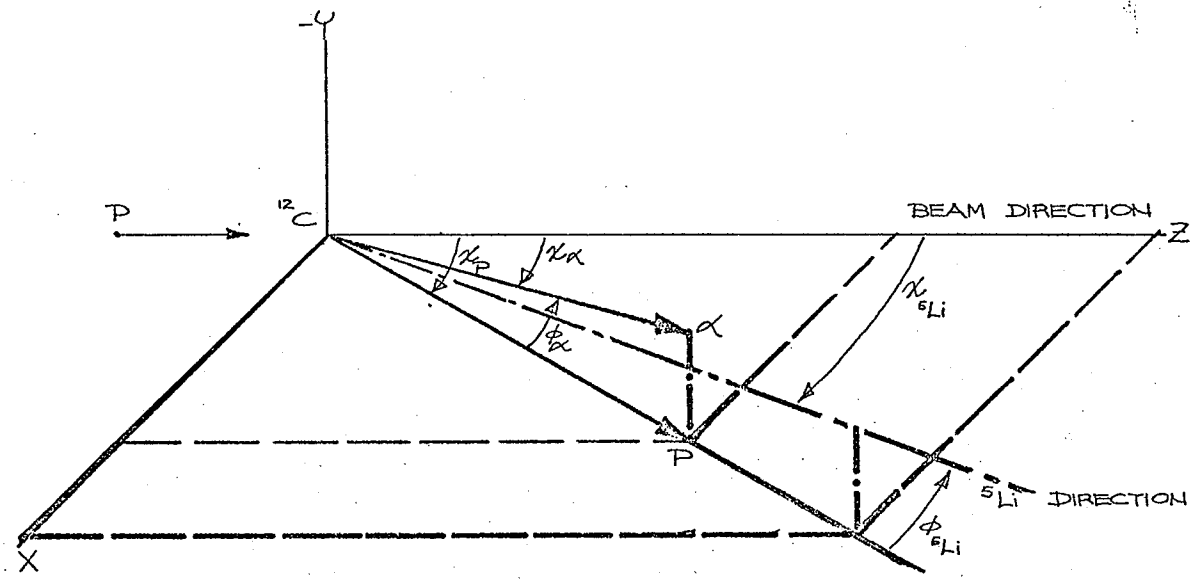
-Y
P
^{12}C
BEAM DIRECTION
Z
χ_p
χ_α
$\chi_{^6Li}$
ϕ_α
α
P
^5Li DIRECTION
$\phi_{^6Li}$
X

-3.2a-

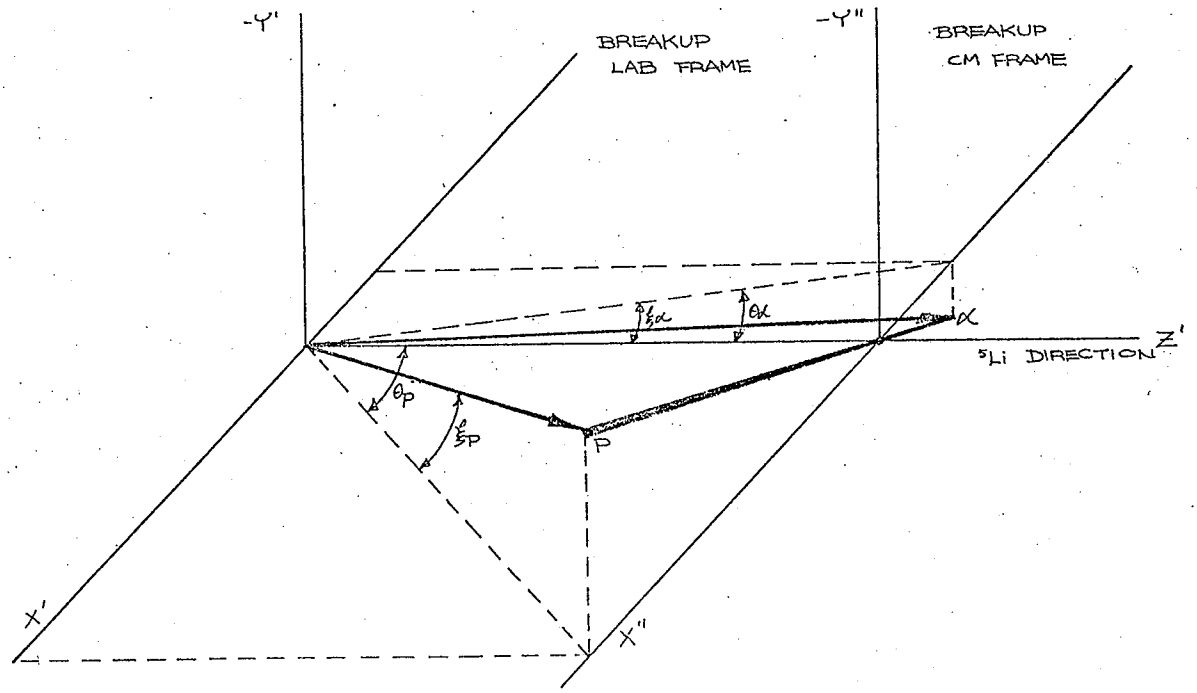
-Y'
BREAKUP
LAB FRAME
-Y''
BREAKUP
CM FRAME
ξ_α
θ_α
α
^5Li DIRECTION
Z'
θ_p
ξ_p
P
X'
X''

-3.2b-

frame. (lab. for short)

For the proton

ψ_p is the laboratory polar angle of proton.

ϕ_p is the laboratory azimuthal angle of proton.

θ_p is the laboratory polar angle of the proton in the ^{5}Li rest frame.

θ_p' is the C.M. polar angle of proton in the ^{5}Li rest frame.

ξ_p is the laboratory azimuthal angle of the proton in the ^{5}Li rest frame.

The corresponding angles of the alpha particle are expressed by replacing p with an α in the proton coordinates, i.e. ψ_α, ϕ_α, θ_α, θ_α', and ξ_α.

As the incident proton strikes the ^{12}C nucleus at rest in the laboratory frame, ^{5}Li is formed. For simplicity of calaulation the shape of the mass distribution was assumed to be a gaussian:

$$F(\Delta M_{5_{Li}}) = F_o\, e^{-(\Delta M_{5_{Li}}/\Delta E)^2} \qquad (3.1)$$

Here F_o normalizes F so that $Fd(\Delta M) = 1$, and the value of ΔE is about 1.5 MeV (LAU66). The Monte Carlo program chose ^{5}Li masses in accordance with this distribution and used them in calculating the kinematics for each event of the simulated reaction.

According to two body relativistic kinematics

(DED62), if all the masses and the centre of mass angle are known for particle i, then the corresponding laboratory angle θ_i and the energy E_i can be obtained by using the following relations

$$\theta_i = \tan^{-1}\left(\frac{\sin\theta_i'}{\gamma(\cos\theta_i') + \beta/\beta'}\right) \qquad (3.2)$$

$$E_i = \gamma(E_i' + \beta P_i' \cos\theta_i') \qquad (3.3)$$

where θ_i' is the C.M. polar angle of the particle i,

$$\gamma = (1-\beta^2)^{-1/2} \qquad (3.4)$$

and E_i' and P_i' are the C.M. energy and momentum respectively.

According to assumptions (4) and (5) the reaction proceeds isotropically in its C.M. frame, and the break up of ^{5}Li is also isotropic in the ^{5}Li C.M. frame. The Monte Carlo technique was thus used to generate ψ'_{ξ_i} and θ_p' according to the equation:

$$\cos\theta' = (1.0-R_1)\cdot\cos\theta_1' + R_1\cdot\cos\theta_2' \qquad (3.5)$$

Here R_1 is a random number distributed uniformly on the interval 0 to 1, θ_2' and θ_1' are the upper and lower limits of $\psi'_{^5Li}$ or θ_p' as the case may be. The azimuthal angles $\phi_{^5Li}$ and ξ_p were obtained by using the following equation:

$$\phi = R_2(\phi_2 - \phi_1) + \phi_1 \qquad (3.6)$$

where R_2 is a second random number and ϕ_1, ϕ_2 are the limits on ϕ. The above equation is a straight line

indicating an equal probability of finding ϕ in any interval $d\phi$.

Thus with the two body kinematic equations mentioned before, the energy and directions of the ^{5}Li, and the proton could be obtained. The energy and direction of the alpha particle were determined using conservation of energy and momentum. However the directions of the proton and alpha particle obtained above are relative to the direction of ^{5}Li as shown in Fig.3.2b, and have to be transformed to the p+^{12}C laboratory frame. This is done using Euler's transformation, and the following set of equations is obtained (DAN72):

For the proton

$$\sin\psi_p \sin\phi_p = \cos\psi_{5_{Li}} \sin\phi_{5_{Li}} \sin\theta_p \cos\xi_p + \cos\phi_{5_{Li}} \sin\theta_p \sin\xi_p + \sin\psi_{5_{Li}} \sin\phi_{5_{Li}} \cos\theta_p \quad (3.7)$$

$$\sin\psi_p \cos\phi_p = \cos\psi_{5_{Li}} \cos\phi_{5_{Li}} \sin\theta_p \cos\xi_p - \sin\phi_{5_{Li}} \sin\theta_p \sin\xi_p + \sin\psi_{5_{Li}} \cos\phi_{5_{Li}} \cos\theta_p \quad (3.8)$$

$$\cos\psi_p = \cos\psi_{5_{Li}} \cos\theta_p - \sin\psi_{5_{Li}} \sin\theta_p \cos\xi_p \quad (3.9)$$

For the alpha particle the subscript p is replaced by α.

With the angles obtained from the above equations, the directions of both the proton and the alpha particle can be transformed to Cartesian Coordinates with the centres of the detectors as the origins. It is useful to make

this transformation because it is simplier in Cartesian Coordinates to compare the location of particle i with the boundaries of the collimators. If particle i falls within the boundary of the collimator, it will be accepted as a good event otherwise it will be rejected. The origin of the new coordinate system may be expressed in terms of the p+^{12}C centre of mass frame using

$$X_i' = r_i \sin\theta_i \cos\phi_i \qquad (3.10)$$

$$Y_i = r_i \sin\theta_i \sin\phi_i \qquad (3.11)$$

$$Z_i = r_i \cos\theta_i \qquad (3.12)$$

where i stands for either p or α and r_i is the distance from the target to the particle i detector. The final transformations to coordinates centred on the detectors are performed by rotating about the y-axis then along the x'-axis as shown in Fig.3.3. The angles of rotations are the angles of the detectors in the p+^{12}C centre of mass frame. With the transformation matrices A and B given in Fig.3.3, the Cartesian Coordinates of the proton or alpha particle in the detector plane can be obtained

Fig.3.3

The matrices A and B for transforming the coordinates of the proton and the alpha particle in the $p + {}^{12}C$ frame to the planes of the detectors.

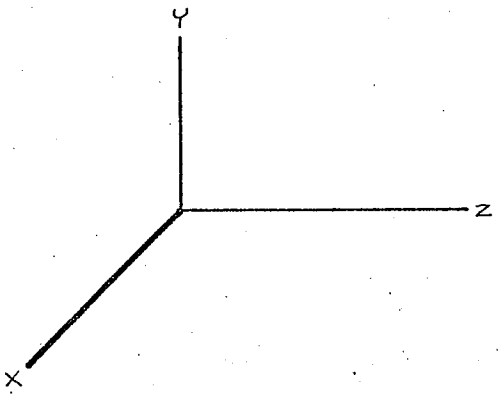

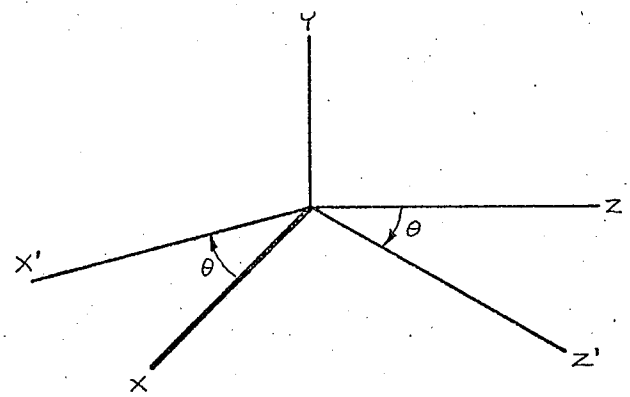

$$A = \begin{pmatrix} \cos\theta & 0 & -\sin\theta \\ 0 & 1 & 0 \\ \sin\theta & 0 & \cos\theta \end{pmatrix}$$

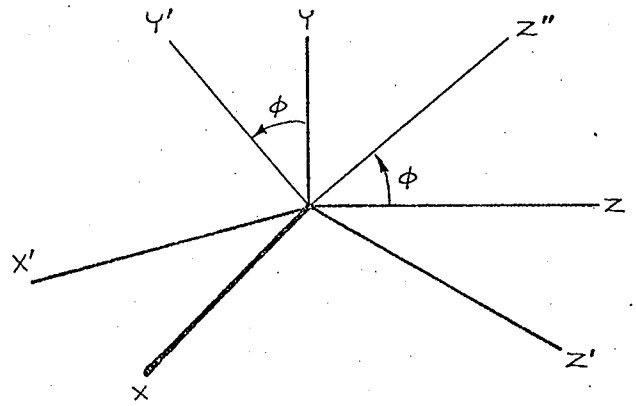

$$B = \begin{pmatrix} 1 & 0 & 0 \\ 0 & -\sin\phi & \cos\phi \\ 0 & \cos\phi & \sin\phi \end{pmatrix}$$

$$\begin{pmatrix} x_i' \\ y_i' \\ z_i' \end{pmatrix} = \begin{pmatrix} 1 & 0 & 0 \\ 0 & -\sin\phi_{Di} & \cos\phi_{Di} \\ 0 & \cos\phi_{Di} & \sin\phi_{Di} \end{pmatrix} \begin{pmatrix} \cos\theta_{Di} & 0 & -\sin\theta_{Di} \\ 0 & 1 & 0 \\ \sin\theta_{Di} & 0 & \cos\theta_{Di} \end{pmatrix} \begin{pmatrix} x_i \\ y_i \\ z_i \end{pmatrix} \quad (3.13)$$

where θ_{Di} and ϕ_{Di} are the polar and azimuthal angles of the ith-particle detector.

Usually 2.5×10^5 events were generated by the program at the target. All these events are assumed to be $^{12}C(p,{}^5Li)^8Be$ events. The first Monte Carlo step established the ^5Li ground state mass. The angle of the ^5Li in the overall centre of mass frame was also obtained using a Monte Carlo technique. This C.M. angle was restricted to a certain range so as to improve the program efficiency. The limits on this angle were determined by starting with a wide angular range and then narrowing the range as far as possible without losing events of the desired type.

With the centre of mass angle of ^5Li generated, the kinematic calculation for $^{12}C(p,{}^5Li)^8Be$ then followed. This calculation gave the laboratory angles and energy of ^5Li in the $p+^{12}C$ frame. The alpha particle and proton angles in the ^5Li rest frame were then generated. Since the breakup Q-value of the ^5Li is 1.96 MeV plus or minus a correction depending on the choosen ^5Li mass, the centre of mass momenta and energies of the proton and the

alpha particle could be calculated. The values of the laboratory momenta and energies in the ^{5}Li rest frame were then obtained. The last step in the program involved the transformation of coordinates as has been discussed. At this stage the azimuthal angle of the ^{5}Li in the p+^{12}C laboratory frame and that of the proton or the alpha particle in the ^{5}Li rest frame were generated. Only the events falling inside the boundaries were accepted. On the basis of the number of events "detected" by the Monte Carlo model, the efficiency ε_p of the detector system was calculated. Since the efficiency defined here is determined by dividing the number of "detected" events by the number generated, the units of ε_p are steradians. See Table3.1.

The shape of the collimator on the proton detector was optimized by running the Monte Carlo program with only the alpha particle detector collimated while observing the distribution of protons on the proton detector plane. The most favorable shape for this collimator was found to be that discussed in section III.2.d. The size of the proton collimator was determined from the light collection efficiency of the plastic scintillator as discussed in the following section and involved maximizing the solid angle while minimizing peak shape distortion. In determining the detector positions the maximum breakup angle of the proton and alpha particle was

Table 3.1

The result obtained from the Monte Carlo calculation for the reaction $^{12}C(p,{}^{5}Li)^{8}Be$ with ^{5}Li breakup into a proton and an alpha particle. The value of $T_{^5Li}+Q$ is obtained from kinematic calculations. This calculation is for incident proton energy of 38.23 MeV.

θ_p	Mean $\theta_{^5Li}$	ε_p (in sr)	$T_\alpha+T_p$ (in MeV)	$T_{^5Li}+Q$ (in MeV)
30°	39°	1.18×10^{-5}	24.7±.2	24.65
40°	46°	1.16×10^{-5}	23.6±.2	23.68
50°	54°	1.14×10^{-5}	22.3±.2	22.41

calculated using the kinematic calculation. This angle was about 40°. However if the size of the collimators and the distances from the detectors to the target were taken into consideration, the optimum angle between the centre lines of the two detectors was approximately 34°.

The output of the program contained the printout of the direction of the ^{5}Li, the energies of the ^{5}Li, proton, alpha particle as well as the sum of the proton and alpha particle energies for each accepted event. The positions where the alpha particle and the proton struck the detectors, were also printed out to ensure that events accepted were indeed within the collimator boundaries. It also contained the distributions of the polar angle, the azimuthal angle, the energy of the ^{5}Li in the p+^{12}C laboratory frame, and the distribution of the breakup angles of the proton and alpha particle as well as the sum of their breakup angles in the ^{5}Li rest frame. The distribution of the detected events on the detector surface was also included.

Figure 3.4 and Table 3.1 summarize the results from this program. Figure 3.4a shows the mean ^{5}Li angle to be ψ_{Li} = 39°, 46°, 54° when the proton detector is located at θ_p = 30°, 40°, 50° respectively. Figure 3.4b shows the distribution of the sum of the kinetic energies of the proton and the alpha particle. The distributions of the breakup angles of the proton and the alpha particle as

well as the sum of their angles are plotted in Figure 3.4c. All the events in these distributions were accepted events within the detector collimators. In these figures it is shown that the range of the sum of the breakup angles is 27°-43° in the ^{5}Li rest frame for all three proton detector angles. The distributions of the alpha particle breakup angles also show a relatively high density around the maximum alpha particle breakup angle as expected.

Table 3.1 shows the values of the ^{5}Li outgoing angle in the p+^{12}C centre of mass frame, the efficiency of the detection system, and the sum of the proton and alpha particle energies. The values of $T_{^{5}Li}$ +Q calculated from two body kinematics at the mean ^{5}Li angle are also shown for comparison.

Fig.3.4a

The distributions of ^{5}Li outgoing angles corresponding to mean proton detector angles of 30°, 40°, and 50°. From these graphs it is seen that the respective ^{5}Li outgoing angles are approximately 39°, 46°, and 54°.

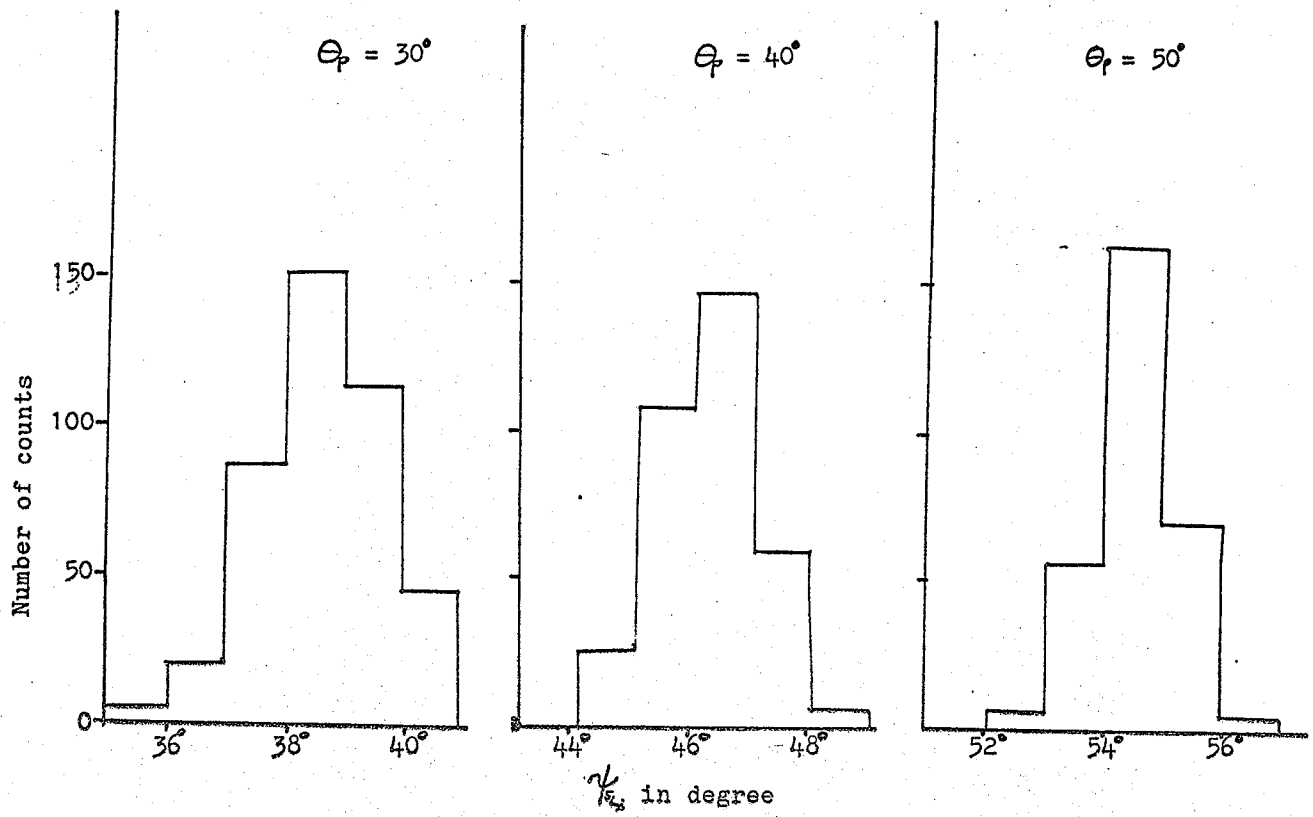
θ_p = 30°
θ_p = 40°
θ_p = 50°
Number of counts
150
100
50
0
36°
38°
40°
44°
46°
48°
52°
54°
56°
ψ_s in degree

Fig.3.4b

The distributions of $T_\alpha + T_p$ obtained from the Monte Carlo calculations.

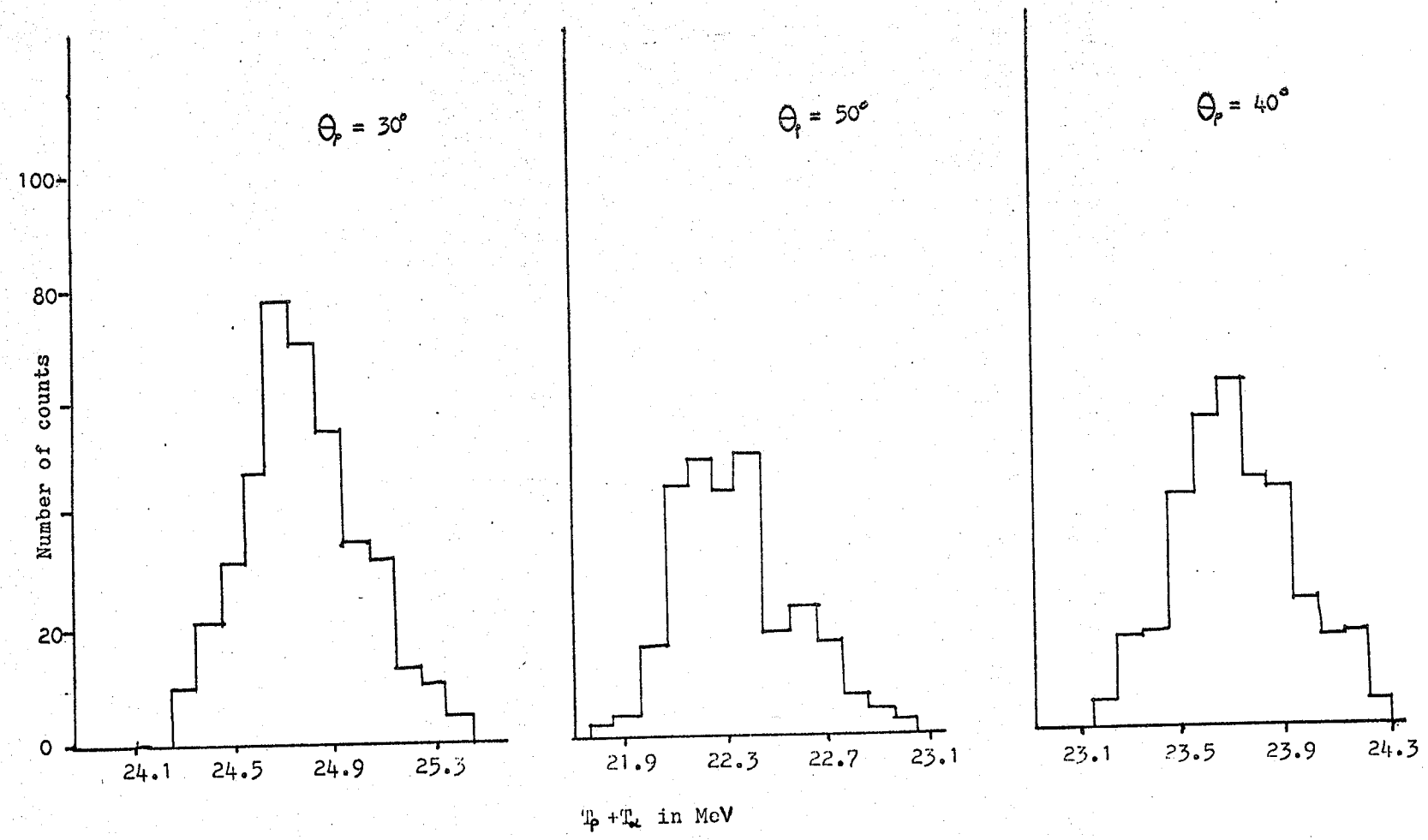
θ_p = 30°
θ_p = 50°
θ_p = 40°
Number of counts
100
80
20
0
24.1
24.5
24.9
25.3
21.9
22.3
22.7
23.1
23.1
23.5
23.9
24.3
$T_p + T_\alpha$ in MeV

Fig.3.4c

The distribution of the separation angles of proton and alpha particle for events detectable by the present experimental arrangement.

Fig.3.4d

The distribution of alpha particle breakup angle in the ^{5}Li rest frame.

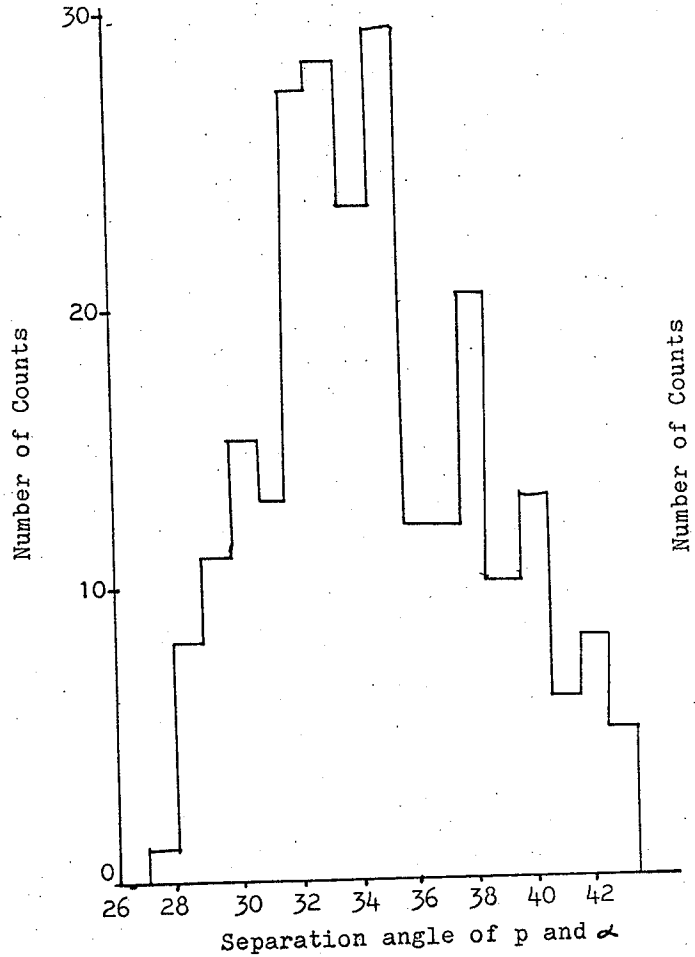

Fig.3.4c

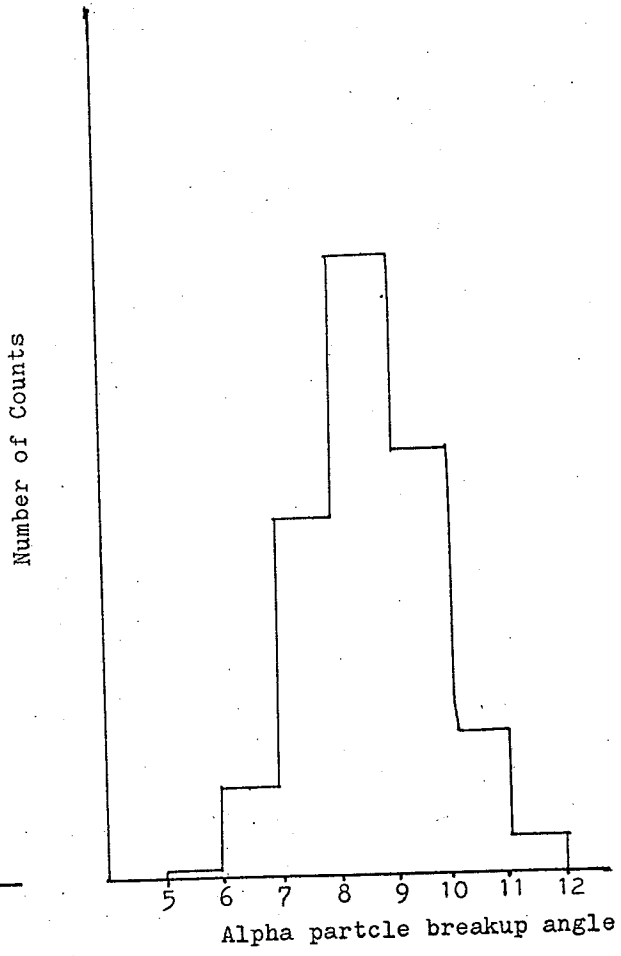

Fig.3.4d

III.2 The Design of the Scintillation Counter

III.2.a Introduction

The ideal apparatus for this experiment would have an alpha particle detector on the scattering plane with one proton scintillation counter placed above the plane and one below it (Fig.3.5a). This arrangement maximizes the proton solid angle while it minimizes the kinematic shift due to accepting protons and alpha particles coming from ^{5}Li nuclei emitted into a wide range of angles. However, due to limitations imposed by the height of the scattering chamber, an arrangement such as described above is not feasible. Unfortunately it is not possible to allow the protons to enter the scintillator off axis as in Fig.3.5b. A study of light collection efficiency in a cylindrical scintillator shows that this arrangement results in very asymmetric peak shapes and poor resolution. An arrangement with the proton detector on the plane and the alpha particle detector above it as shown in Fig.3.5c is a possible alternative.

This section will discuss the properties of plastic scintillators, the light collection process and also the distortion effect of off axis proton detection.

Fig.3.5a

An ideal case where two plastic scintillation counters are used as proton detectors. One of the counters is placed above the scattering plane and the other below it. Both counters are tilted and their central axes make angles of 34° with the scattering plane. An alpha detector is placed on the median plane.

Fig.3.5b

Proton detectors are placed parallel to the incident beam such that resultant particles from proton bombardment of ^{12}C enter the proton detectors off the central axis of the proton detectors.

Fig.3.5c

A possible alternative arrangement of the detectors in which the proton detector is placed on the median plane while the alpha particle is tilted and its axis makes an angle of 34° with the median plane.

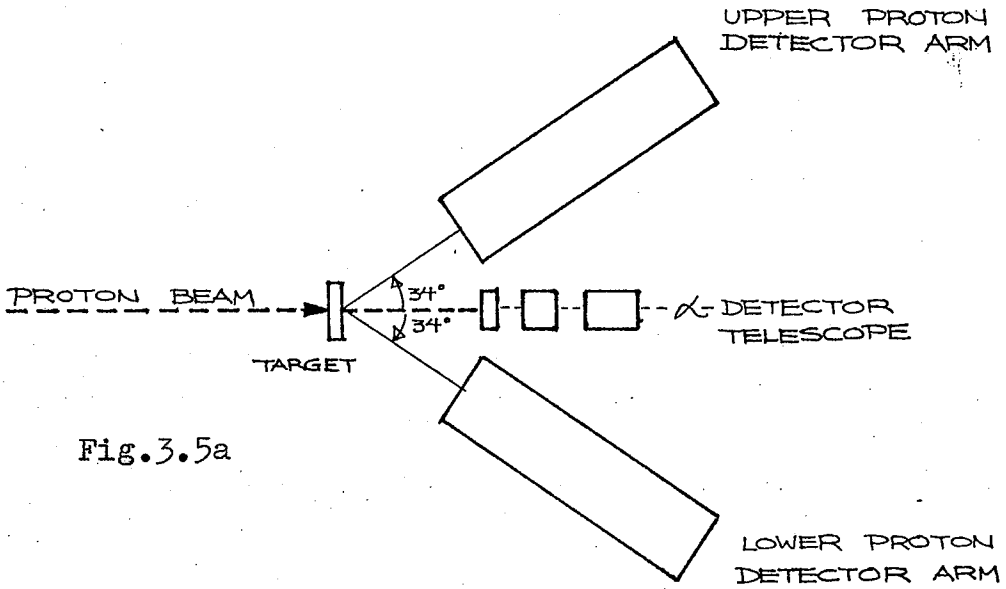

Fig.3.5a

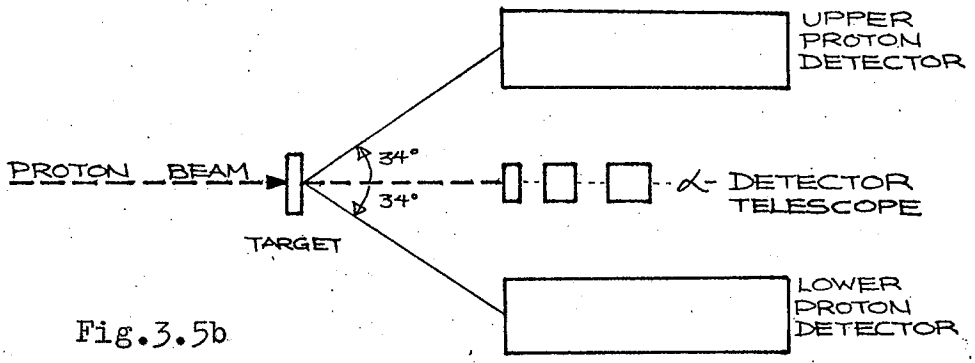

Fig.3.5b

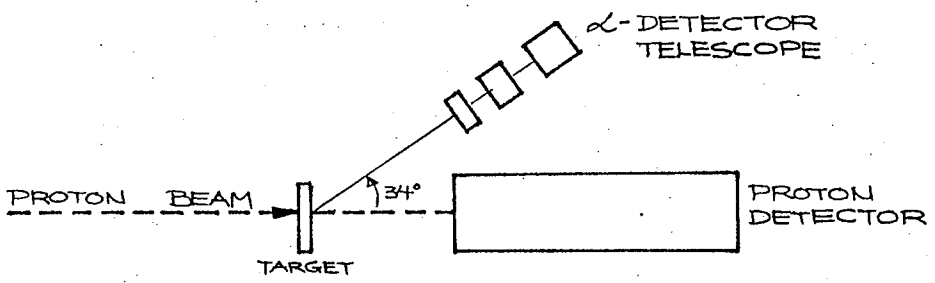

Fig.3.5c

III.2.b The Characteristics and Properties of Plastic Scintillators

It is well known that plastic scintillators have a non-linear response for low energy protons. The light output for a given energy loss is less when the density of ionization is high. Wright (WRI53) obtained the following relation:

$$\frac{dL}{dx} \propto \log\left(1 + a\frac{dE}{dx}\right) \qquad (3.15)$$

Here a is a constant and is equal to 25±2mg-MeV/cm² for protons, and dL/dx is the light output in the segment dx of the range.

Various authors (SHU49,POT60,KEI70,ANK63) have considered the theory and experimental results regarding light collection efficiencies for various sizes and shapes of scintillation counters. In these studies it has been shown that the efficiency of the light collection depends strongly on the position within the scintillator at which light is produced. For instance, light produced near the walls of a cylindrical scintillator is more effectively transported to the photocathode than light produced near the axis (AVE63). The light collection efficiency of plastic scintillators will be farther discussed in Section III.2.c.

Another characteristic of scintillators closely

related to light collection efficiency is the attenuation factor (KUI66). This attenuation of light intensity is caused by absorption of photons within the scintillator. The intensity of light depends on the path length according to the expression:

$$I = I_0 \exp(-\alpha x) \qquad (3.16)$$

where x is the path the photon has traversed, and α is the attenuation coefficient. The value of α changes as the path length increases. For NE102A scintillators (such as used in this experiment) with length in excess of 1 cm, α is approximately equal to 0.04 cm^{-1} while for short scintillators it is closer to 0.08 cm^{-1}.

III.2.c The Light Collection Efficiency of a Plastic Scintillator

When a scintillating plastic and a photomultiplier are used to detect charged particles, there may be large variations in the magnitude of the output pulse from particle to particle, and in some special cases the resulting peak shape may be severely distorted. The main features of the peak shapes produced by protons are determined by two factors:

(1) the statistical fluctuations in the number of electrons emitted from the photocathode, due primarily to the

finite number of photons produced in the scintillator.

(2) the variations in light transmission from the scintillator to the cathode, arising from different reflection and absorption losses along the various paths that the photon may follow within the scintillator.

The first of these two factors is assumed to have a Gaussian form and will not be discussed further. The second factor which deals with light collection efficiency as a function of position in the scintillator volume is discussed in more detail.

In the calculation of light collection efficiency, a scintillator is described as a volume radiator which is characterized by the energy E_o in the form of light arising in the scintillation process, a coefficient of absorption α, and an index of refraction n. The ratio, E/E_o, of the energy E arriving at the cathode to E_o, is called the light collection coefficient ε.

In the following treatment of the light collection efficiency, the following approximations and assumptions are used:

(1) The scintillator material is homogenous, isotropic, and free of flaws and sources of internal scattering. Any nuclear interactions in the scintillator are neglected(BAK69).

(2) The scintillator surfaces are well polished and reflections are specular.

(3) At every point within the scintillator the fluorescent light is produced isotropically.

(4) The ratio of the smallest dimension of the body to the longest wavelength involved is very large, allowing geometric optics to be used.

(5) The photocathode response is assumed uniform.

In this thesis the shape of the scintillator is restricted to a right circular cylinder, and the material considered is NE102A plastic scintillator. Fig.3.6 shows the scintillator-photomultiplier system and the geometry of a ray inside a cylinder.

The calculation of the light collection efficiency, ε, involves two main factors, the reflection and the absorption of light inside the scintillator. The average efficiency is:

$$\varepsilon = \frac{1}{N} \sum_{i=1}^{N} R_i \exp(-\alpha x_i) \qquad (3.17)$$

where N is the number of photons produced by the scintillation process, and i refers to a single photon. R_i is the reflection probability for the i-th photon, and x_i is the path length traversed by the i-th photon.

The dependence of on (ρ, z) (Fig.3.7) was first investigated by L.N. Averina (AVE63). In that work the values for the light collection efficiency were calculated for unpacked, polished, cylindrical scintillators,

Fig.3.6a

Sketch of the scintillator-photomultiplier system.

Fig.3.6b

Geometry of a ray inside a cylinder.

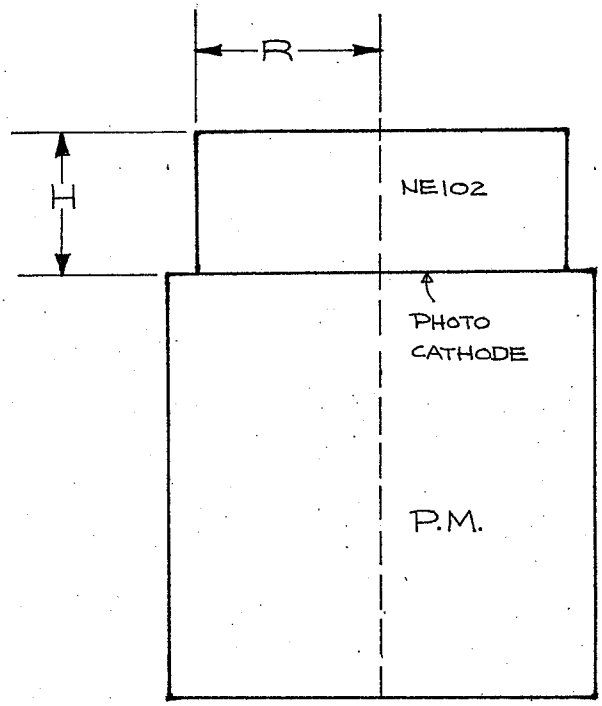

Fig.3.6a

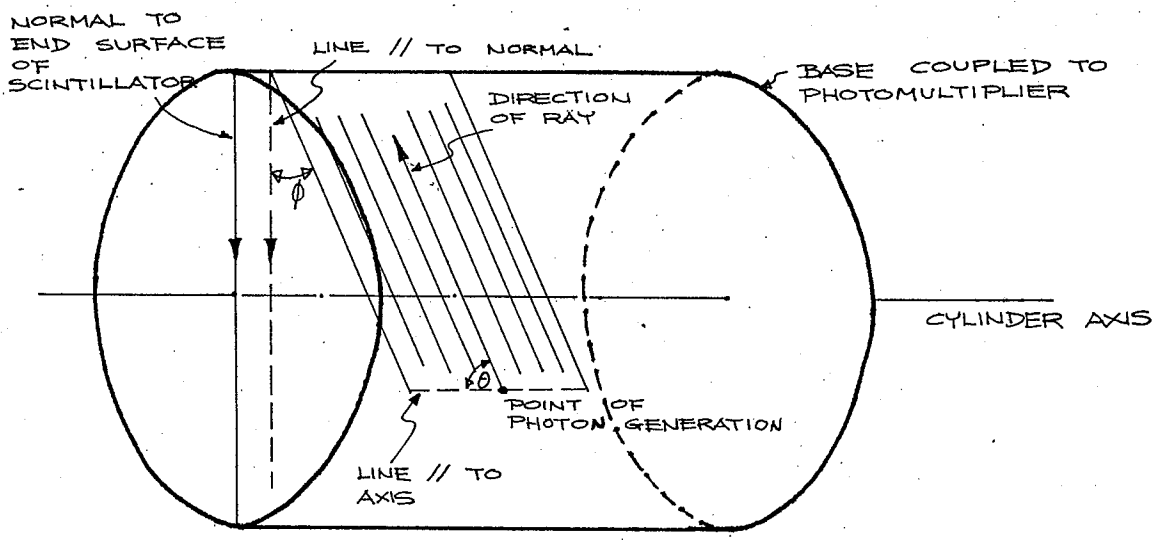

Fig.3.6b

Fig.3.7

The coordinates used in the calculation of the light collection efficiency. Cylindrical coordinates are used. ρ is measured from the central axis of the cylinder and z is measured from the end far from the photocathode.

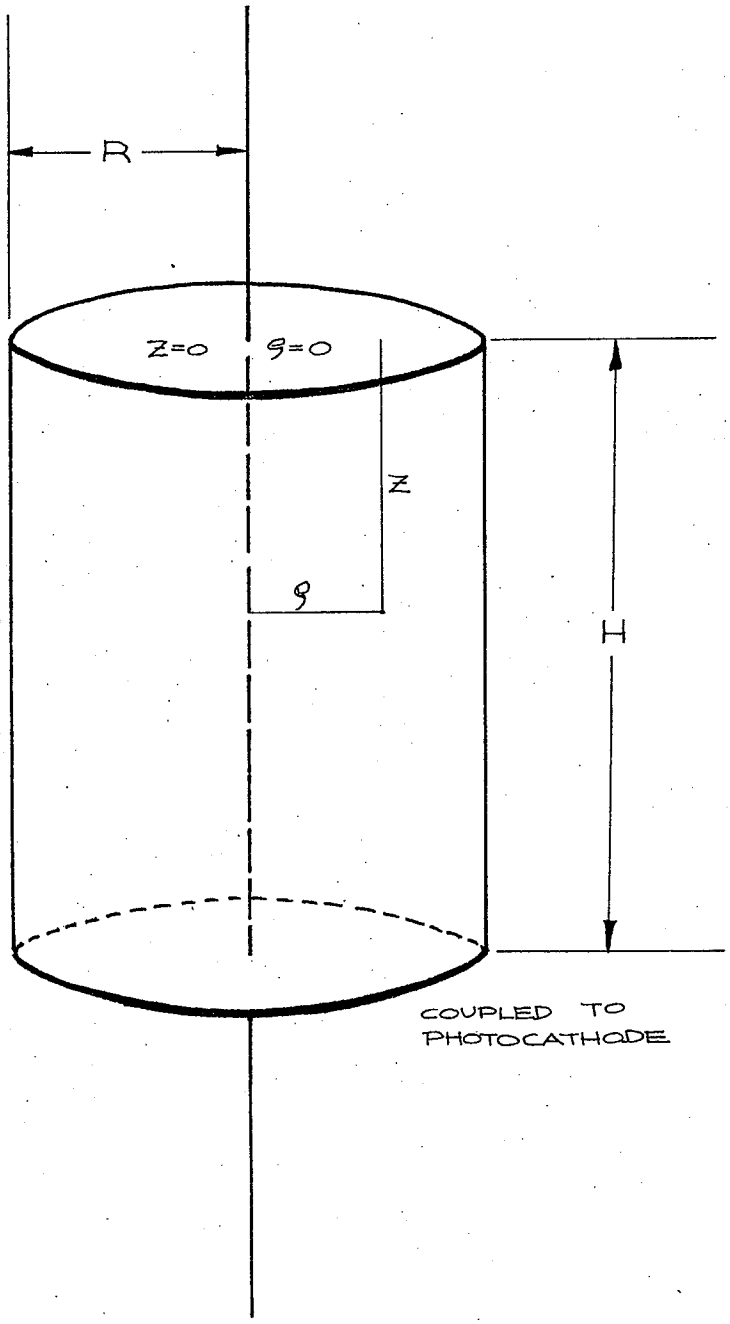
R
Z=0
ρ=0
z
ρ
H
COUPLED TO
PHOTOCATHODE

and ccmpared with experimental data. Unfortunately the paper did not give sufficient numerical or graphical data or calculate peak shape. In the present work therefore the light collection efficiency of NE102A plastic scintillators was also briefly investigated firstly by a Monte Carlo simultation and then by comparison with some data of interest to the present experiment. Plastic scintillators in the form of right circular cylinders, with radii of 1.0 cm and lengths of 1.0, 2.0, and 4.0 cm were considered. The necessary data such as the index of refraction and attenuation coefficient were obtained from the data sheets published by Nuclear Enterprises.

Details of the dependence of ε on ρ and z are summarized in Fig.3.8 which shows the calculated light collection efficiency as a function of the radius (ρ) from the central axis of the cylinder and the distance (z) measured parallel to the cylinder axis from the end farthest from the photocathode. A strong increase in collection efficiency near the walls of the cylinder and near the photocathode is apparent. The increase near the walls is due primarily to the increased portion of the light that is totally reflected at the walls. It is also apparent that the response becomes more nearly independent of ρ close to the photocathode where the walls play a reduced role. These features are qualitatively similar with those of Averina (AVE63).

Fig.3.8

Light collection efficiency as a function of radius (ρ) and distance (z) from the end farthest from the photocathode for scintillators of length 1.0, 2.0, 4.0 cm. In each case the scintillator radius is 1.0 cm. All values of z are in centimetres.

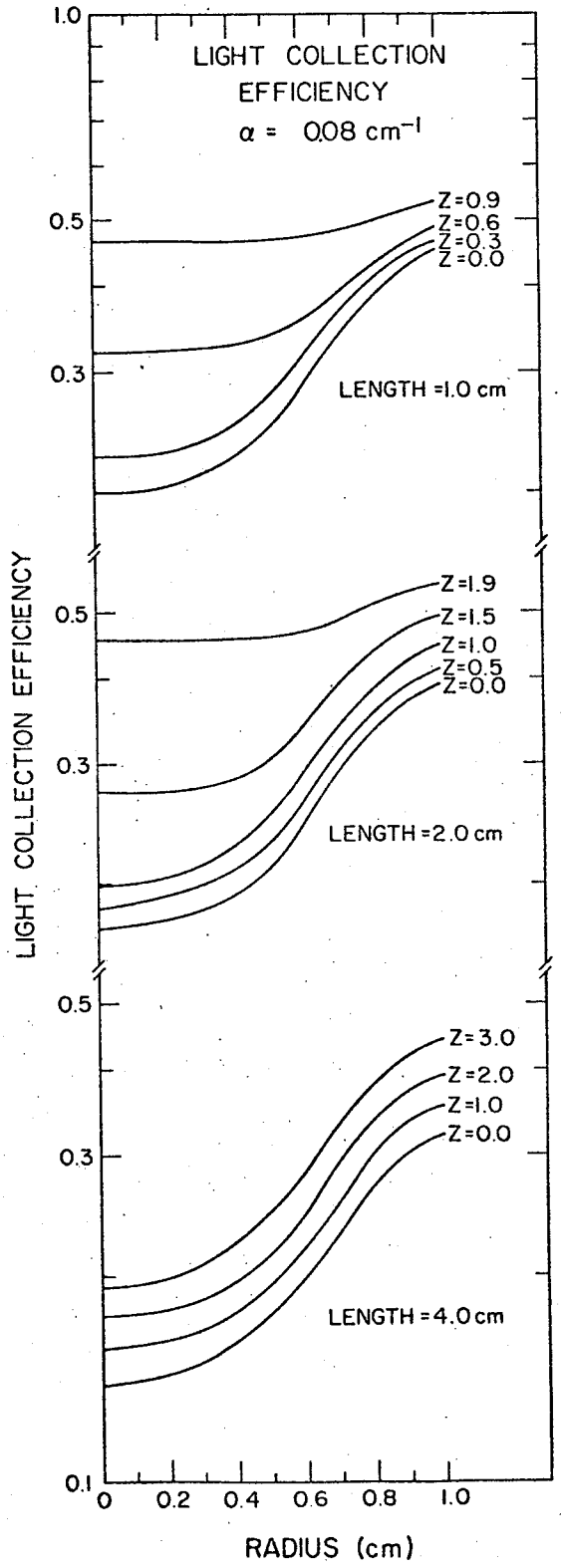
LIGHT COLLECTION
EFFICIENCY
α = 0.08 cm⁻¹
Z=0.9
Z=0.6
Z=0.3
Z=0.0
LENGTH =1.0 cm
Z=1.9
Z=1.5
Z=1.0
Z=0.5
Z=0.0
LENGTH =2.0 cm
Z=3.0
Z=2.0
Z=1.0
Z=0.0
LENGTH =4.0 cm
LIGHT COLLECTION EFFICIENCY
1.0
0.5
0.3
0.1
0
0.2
0.4
0.6
0.8
1.0
RADIUS (cm)

III.2.d The Effects of Collimators and off-axis Detection on the Peak Shape

In the last section it was shown that ε depends strongly on the coordinates (ρ, z). It follows that the collimators play an important role in determining the peak shape. In this section such an effect is first studied for protons incident parallel to the scintillator axis, and then for protons entering at an angle to the cylinder axis.

Various collimators may be described by giving the width $W(\rho)$ shown in Fig.3.9 as a function of ρ. The number dN of protons entering the scintillator between radii ρ and $+d\rho$ is then given by

$$dN = W(\rho)\, d\rho \times F_0 \qquad (3.18)$$

where F_0 is the incident flux.

According to equation (3.15) in section III.2.b, the light output is described by:

$$\frac{dL}{dx} \propto \log\left(1 + a\frac{dE}{dx}\right) \qquad (3.15)$$

where x is measured in units of mass per unit area as compared to ρ and z which are measured in centimetres. The total light collected at the photocathode from a proton entering vertically at radius ρ is

Fig.3.9

The collimator with width $W(\rho)$ which can be described as a function of the coordinate ρ. In general $W(\rho)$ may have different values on the top and the bottom of the collimator.

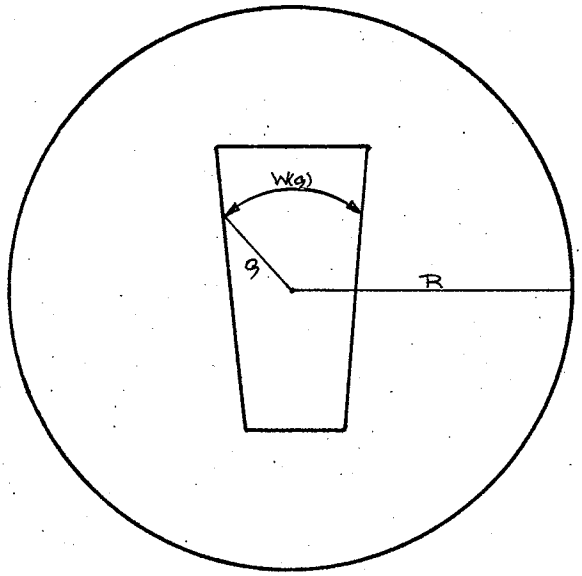
W(g)
g
R

$$I \propto \int_0^R \frac{dL}{dx}\,\varepsilon(\rho,z)\,dz \qquad (3.19)$$

where R is the proton range in the scintillator.

The pulse height distribution is then given by

$$\begin{aligned}\frac{dN}{dI} &\propto \frac{W(\rho)}{dI}\,d\rho \\ &= W(\rho)\,\frac{d\rho}{dI} \\ &\propto W(\rho)\left[\frac{d}{d\rho}\int_0^R \frac{dL}{dx}\,\varepsilon(\rho,z)\,dz\right]^{-1}\end{aligned} \qquad (3.20)$$

Calculations were carried out for circular collimators and for slit collimators of widths 1.0mm, 2.0mm, and 4.0mm. All slit collimators were taken to have round ends (i.e. ρ = constant). Thus a slit collimator 4.0mm wide and 4.0mm long is identical to a circular collimator of diameter 4.0mm.

Fig.3.10 shows simulated peak shapes calculated using the Monte Carlo program without any broadening due to the statistical nature of light detection or electronics. The peaks obtained for the four collimators are normalized at the maximum pulse height to emphasize differences in peak shape. The arrows labelled 4 to 16 indicate the portion of each curve that is used in obtaining the peak shape for collimators of various sizes.

There are several features of special interest. Firstly a circular collimator 4mm in diameter placed on the scintillator axis will produce a pulse height distribution with an intrinsic width of approximately 2%. Slit

Fig.3.10a

Simulated peak shapes obtained from a Monte Carlo calculation of light collection efficiency assuming various collimators placed in front of the scintillator and symmetrically with respect to the scintillator axis. The scintillator was taken to be 1.0 cm long by 1.0 cm in radius. The incident protons are vertically incident and have initial energies of 20 MeV. The arrows indicate the high energy limits for the collimators of various size. No peak broadening due to electronics or the statistical nature of light production is included.

Fig.3.10b

Same as for Fig.3.10a but the scintillator is 4.0 cm long.

Fig.3.10c

Same as for Fig.3.10a but the scintillator is 4.0 cm long and the incident proton energy is 50 MeV.

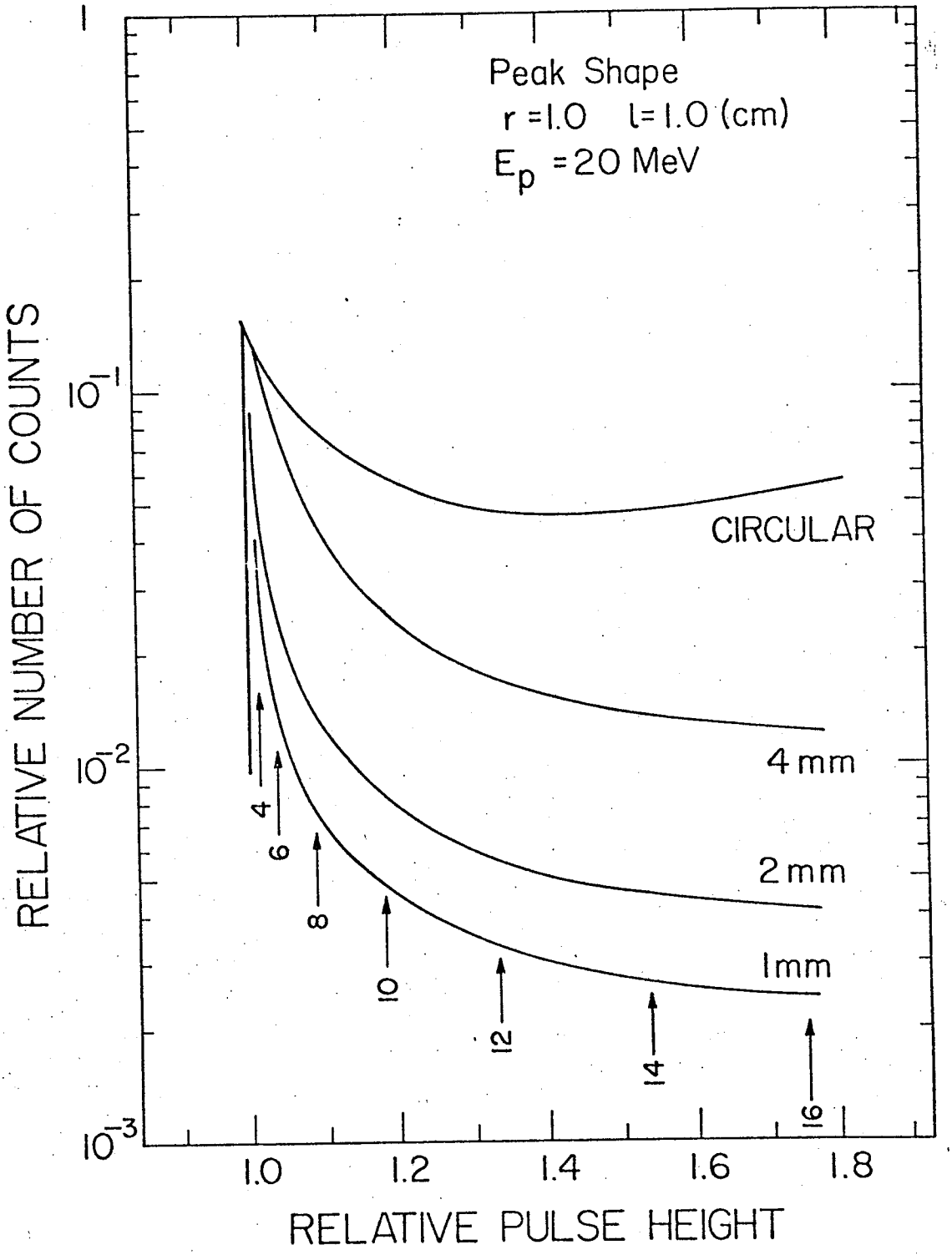
Peak Shape
r =1.0 l=1.0 (cm)
Ep =20 MeV
CIRCULAR
4 mm
2 mm
1mm
4
6
8
10
12
14
16
RELATIVE NUMBER OF COUNTS
RELATIVE PULSE HEIGHT
1
10⁻¹
10⁻²
10⁻³
1.0
1.2
1.4
1.6
1.8

Fig.3.10a

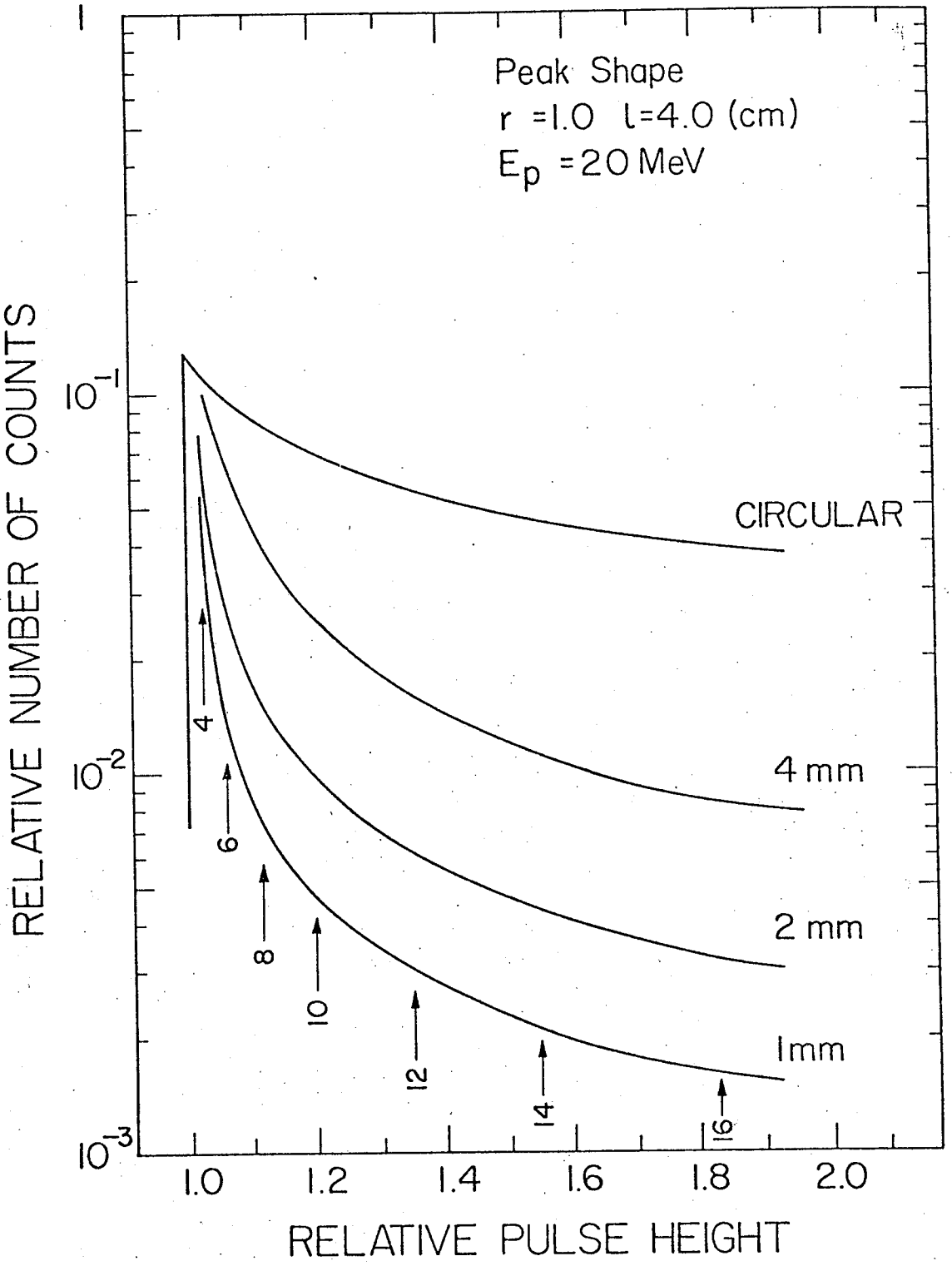
Peak Shape
r =1.0 l=4.0 (cm)
Ep =20 MeV
CIRCULAR
4 mm
2 mm
1mm
4
6
8
10
12
14
16
RELATIVE NUMBER OF COUNTS
RELATIVE PULSE HEIGHT
1
10-1
10-2
10-3
1.0
1.2
1.4
1.6
1.8
2.0

Fig.3.10b

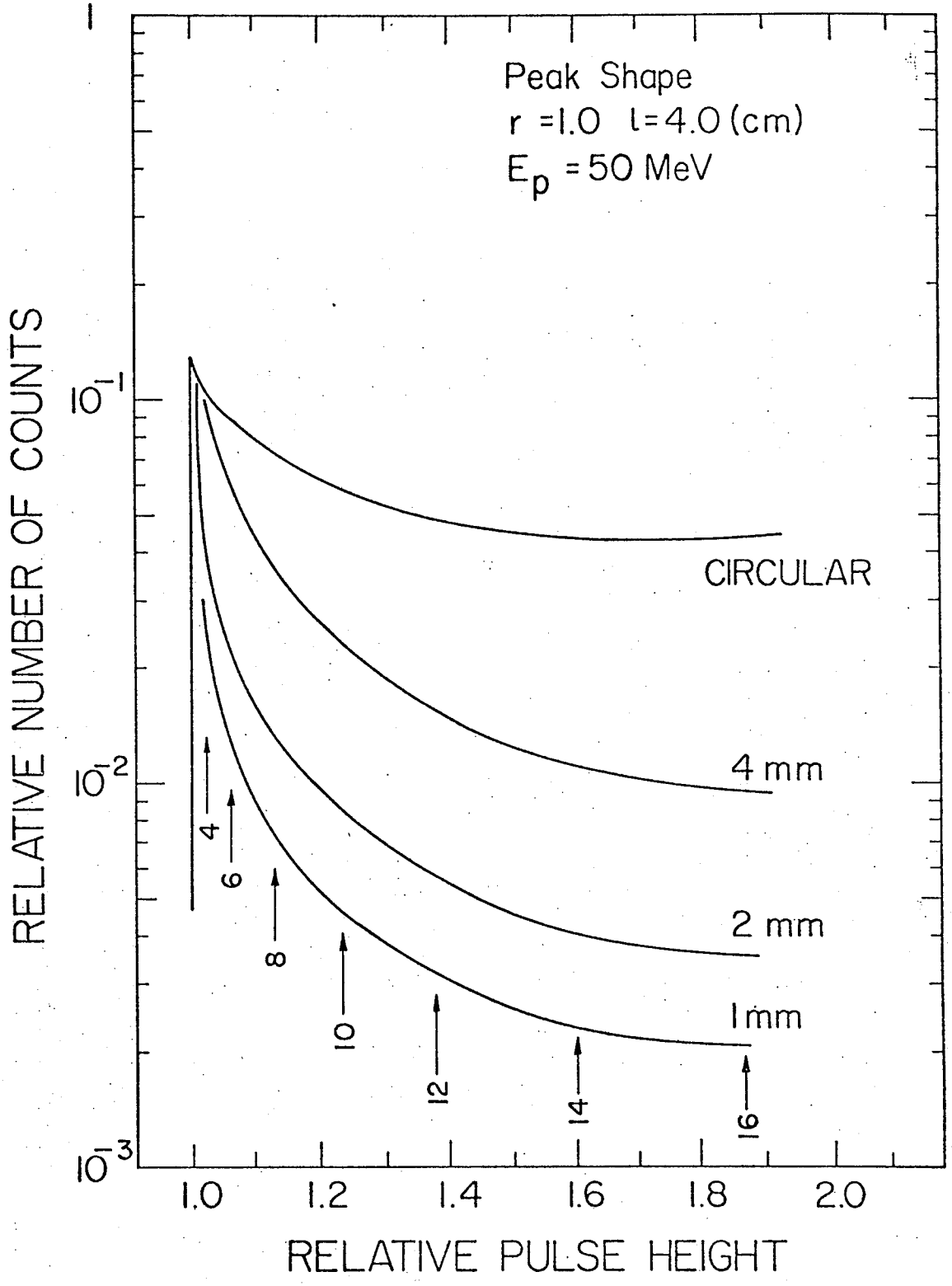
Peak Shape
r =1.0 l=4.0 (cm)
E_p = 50 MeV
CIRCULAR
4 mm
2 mm
1 mm
4
6
8
10
12
14
16
RELATIVE NUMBER OF COUNTS
RELATIVE PULSE HEIGHT
1
10^{-1}
10^{-2}
10^{-3}
1.0
1.2
1.4
1.6
1.8
2.0

Fig.3.10c

collimators will be slightly narrower. The same collimator placed off-axis will give poorer resolution. Even an 1 mm collimator centred at 0.7cm from the axis of the scintillator will have an intrinsic resolution of approximately 8%. Finally it is clear that system using large collimators, that allow protons to enter near the scintillator walls as well as near the centre, may have seriously impaired resolution.

When protons enter the scintillator at an angle to the scintillator axis as shown in Fig3.11, equation (3.20) must be modified. In the case of collimators, whose width is much less than their length, the necessary modification reduces to

$$\rho = y\sin\theta \pm \rho_0 \qquad (3.21)$$

where y is the distance covered by the proton inside the scintillator, θ is the incident angle, and ρ_0 is the value of where a given proton enters the scintillator. The sign of ρ_0 depends on which side of the cylinder axis (either group A or group C in Fig.3.11) the proton enters. Finally

$$z = y\cos\theta \qquad (3.22)$$

Obviously in evaluating equation (3.20), dz will be replaced by dy.

Fig.3.12 shows the result for 20 MeV protons incident at θ=30° on a scintillator 1.0cm long. Slit

Fig.3.11

Geometry of a collimator-scintillator system for measurements with protons incident at an angle θ from the vertical.

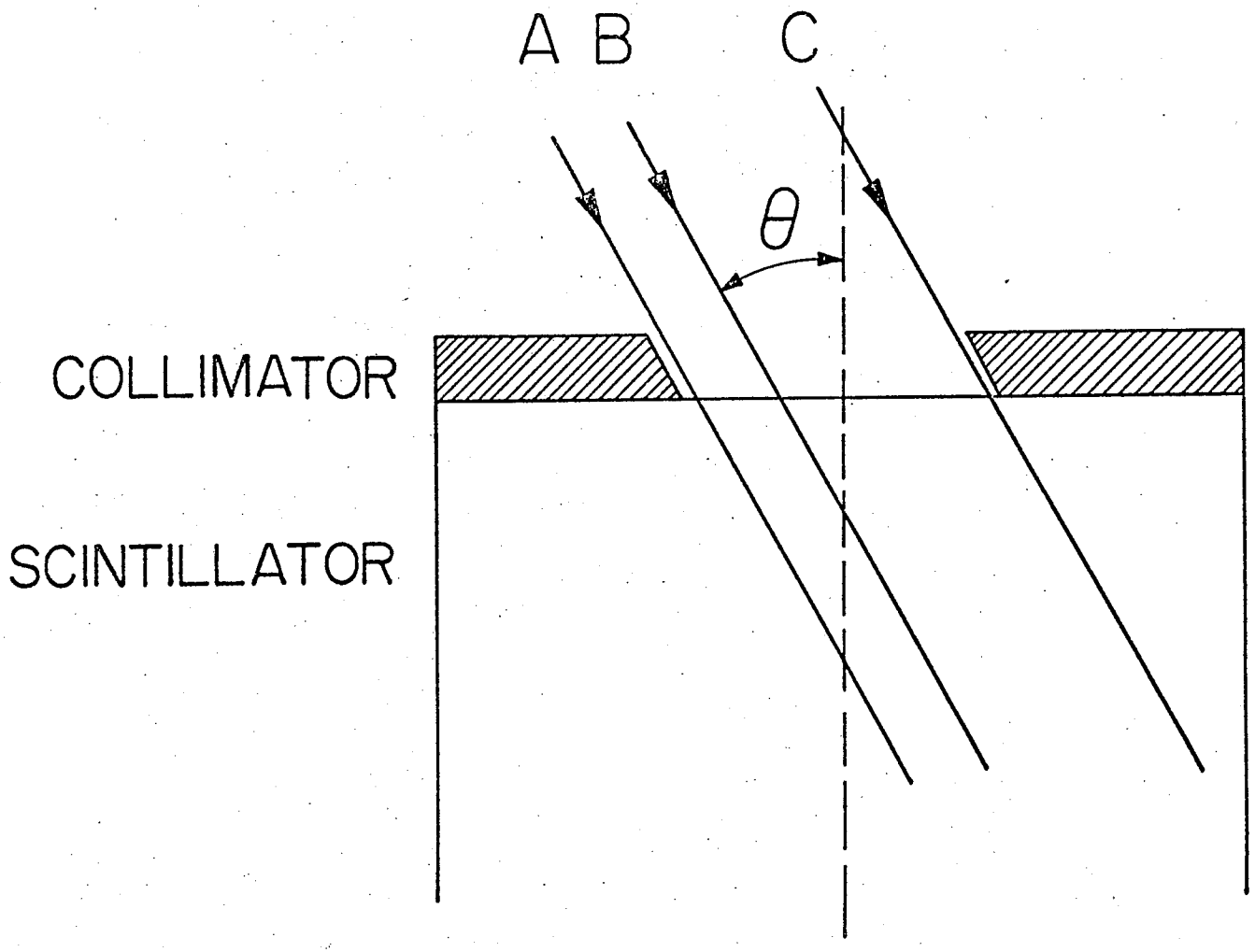
A B
C
θ
COLLIMATOR
SCINTILLATOR

Fig.3.12

Peak shapes for 20 MeV protons incident at 30° to the vertical on a scintillator 1.0 cm long of radius 1.0 cm. In each case the collimator is symmetrically placed with respect to the scintillator axis and is 2.0 mm wide. Calculated results are shown for collimators slits of lengths 4.0mm, 6.0mm, and 8.0mm.

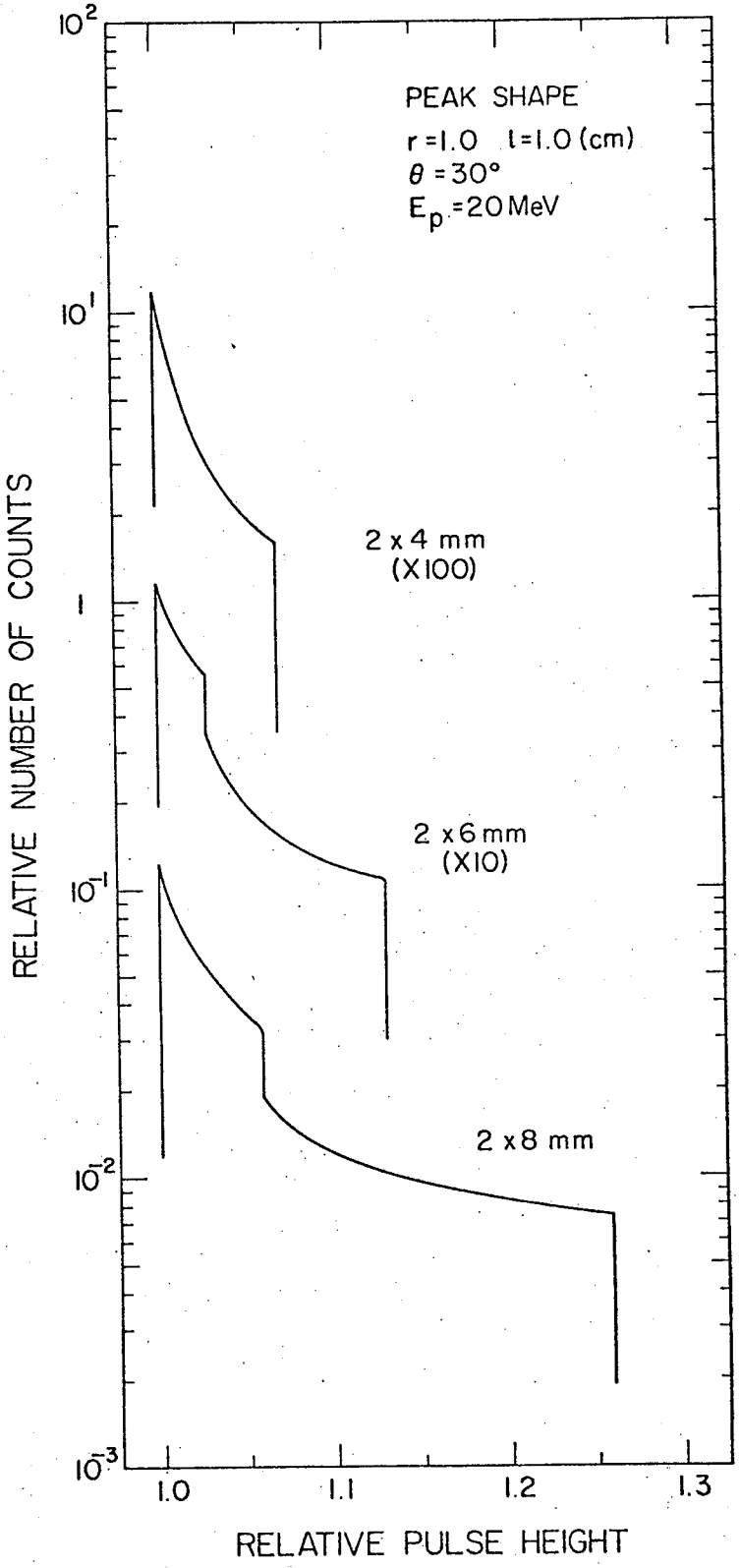
PEAK SHAPE
r=1.0 l=1.0 (cm)
θ=30°
E_p=20 MeV
2 x 4 mm
(X100)
2 x 6 mm
(X10)
2 x 8 mm
RELATIVE NUMBER OF COUNTS
RELATIVE PULSE HEIGHT
10^2
10^1
1
10^-1
10^-2
10^-3
1.0
1.1
1.2
1.3

collimators of sizes 2.0mm wide and 4.0,6.0 and 8.0 mm long are assumed. In these peak shapes a double pedestal on the high energy side is observed. However this phenomenon can be understood qualitatively from the previous discussions. The protons from group C (in Fig.3.11) traverse regions of the scintillator with higher light collection efficiency than those from either of groups B and A. On the other hand, for longer collimators, protons in group A pass through volumes of the scintillator in which light collection efficiency is also rising steeply with δ. As a result these protons generate a second pedestal that overlies that coming from group C.

The discussion in this section is next applied to calculate the peak shape obtained using a large wedge-shape collimator employed at an early stage of the present work. The scintillator was a cylinder of NE102A 4.0 cm in diameter and 2.5 cm long, polished on all surfaces and optically coupled to an EMI 9815B photomultiplier. The scintillator was placed in a brass casing and the end opposite to the photomultiplier was in contact with a Havar foil.

The collimator was a wedge 24.7mm long varying in width from 3.7mm to 6.0mm as shown in Fig.3.13. The ends of the wedge were cut at a 34° angle so that protons with a 34° angle of incidence and moving in a plane containing

Fig.3.13

The collimator used in obtaining the experimental data for both the light collection efficiency experiment and the $^{12}C(p,^{5}Li)^{8}Be$ experiment.

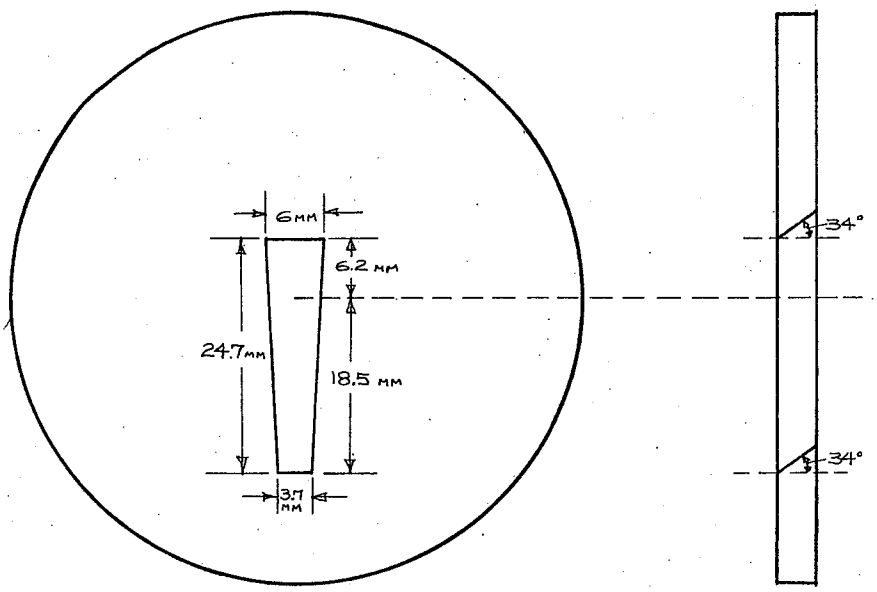

FRONT VIEW

SIDE VIEW

the long axis of the wedge, travelled essentially parallel to the walls of the collimator. The wedge was offset from the axis of the scintillator parallel to the long axis of the collimator so that next to the scintillator, the narrow end of the collimator was 18.5mm from the cylinder axis while the wider end was 6.2mm away as shown in Fig.3.13. Protons with energies of approximately 35 MeV were scattered into the above system and the peak shape shown in Fig.3.14 was recorded. The broadening due to electronics was deduced from the spectrum obtained by using a 3mm diameter circular collimator centred on the scintillator axis and with protons incident parallel to the axis. The full width half maximum of this latter peak is 3.3±0.1%. Unfolding the width due to the finite size of the collimator left a 2.6±0.2% F.W.H.M. broading (very nearly Gaussian) due to electronics and statistics. The Gaussian shape is shown in the insert in Fig.3.14 to the same horizontal scale as the experimental peak.

The curve labelled " perfect resolution" shows the intrinsic peak shape calculated as described previously. The peak shape obtained by folding the "perfect resolution" curve with the 2.6% F.W.H.M. gaussian curve reproduces the experimental data quite well. The effect of the overlying pedestal is clearly visible in the experimental spectrum. A small change of slope near a relative pulse height of 1.10 due to the underlying

Fig.3.14

Comparision of calculated and experimental peak shapes. Experimental data are shown by dots. The curve labelled "Resolution 2.6% (F.W.H.M)" is calculated from the unbroadened peak shape labelled "perfect resolution" by folding a Gaussian shape with resolution of 2.6% (F.W.H.M.) shown in the insert.

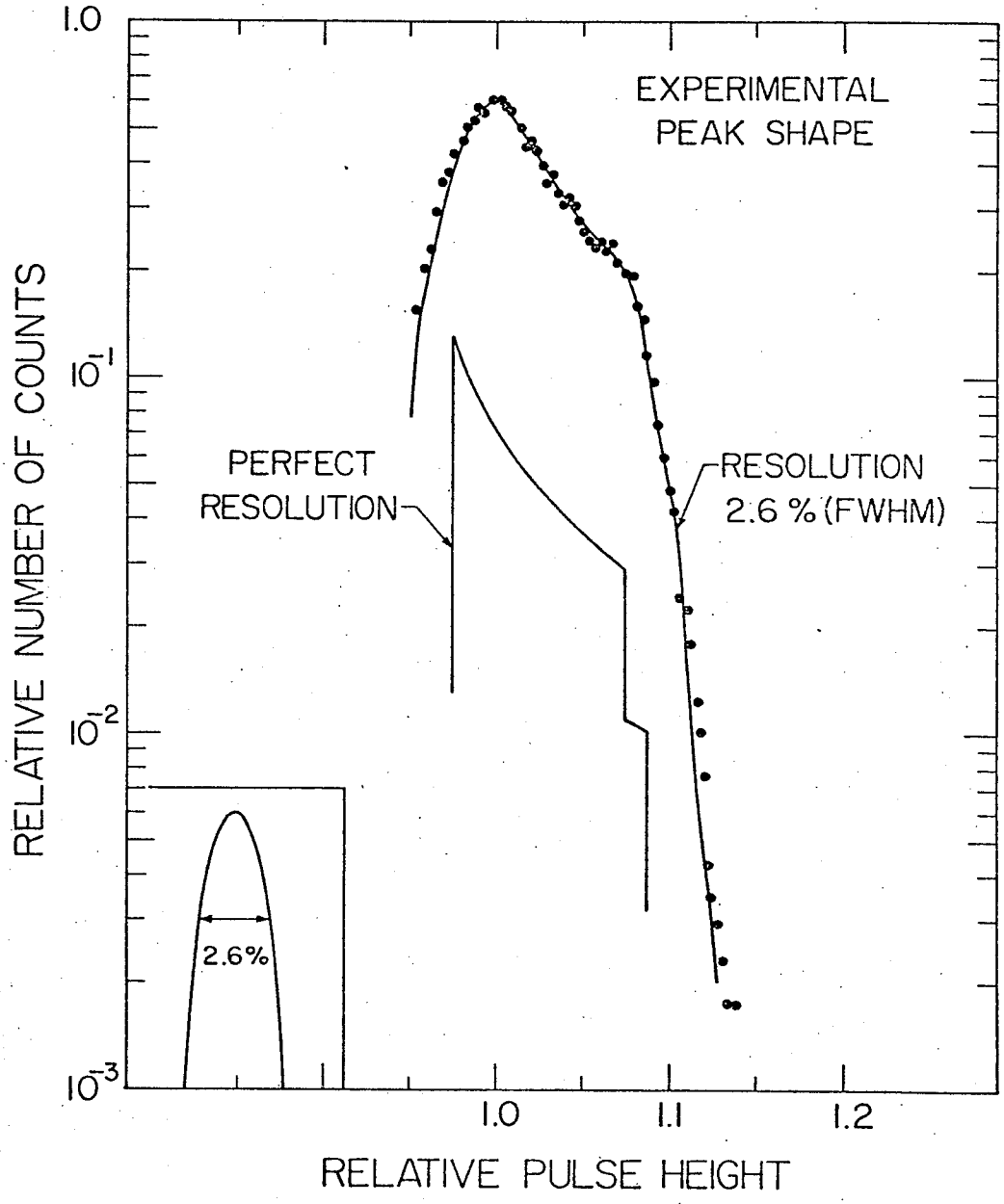
1.0
10^{-1}
10^{-2}
10^{-3}
RELATIVE NUMBER OF COUNTS
EXPERIMENTAL
PEAK SHAPE
PERFECT
RESOLUTION
RESOLUTION
2.6 % (FWHM)
2.6%
1.0
1.1
1.2
RELATIVE PULSE HEIGHT

pedestal is also visible in both the experimental and calculated peak shapes. The discussion in this section then clearly suggests that the idea of using a proton detector with protons incident off axis is not desirable because of the asymmetric peak shape obtained both theoretically and experimentally.

IV. The Experiment

IV.1 The Cyclotron and the Scattering Chamber

The proton beam used in this experiment was produced in the sector-focused cyclotron of the University of Manitoba (BUR66). This cyclotron accelerates negative hydrogen ions resulting in external proton beams variable in energy from 20 to 49 MeV. Fig.4.1 shows the layout of the cyclotron, experimental area, and the scattering chamber. Figs.4.2 and 4.3 show a sketch of the 36" scattering chamber used in this experiment including the detector and the target positions. A target ladder capable of holding up to 6 targets was mounted on top of the chamber. Detectors were mounted on a rotating platform fitted with a Decitrak angular readout. The beam current, which was measured and integrated by a current integrator, was typically around 6 nanoampres on the target throughout this experiment. The reasons for using such low currents were firstly to lower the background and secondly to lower the counting rate to the rate that the photomultiplier could handle. A counting rate reduction was necessary because of the fact that in this experiment fast timing, which required high voltage, was used. Consequently overheating the photomultiplier might result at high count rates. The maximum counting rate that the photomultiplier could handle was calculated

Fig.4.1

cylotron beam line layout.

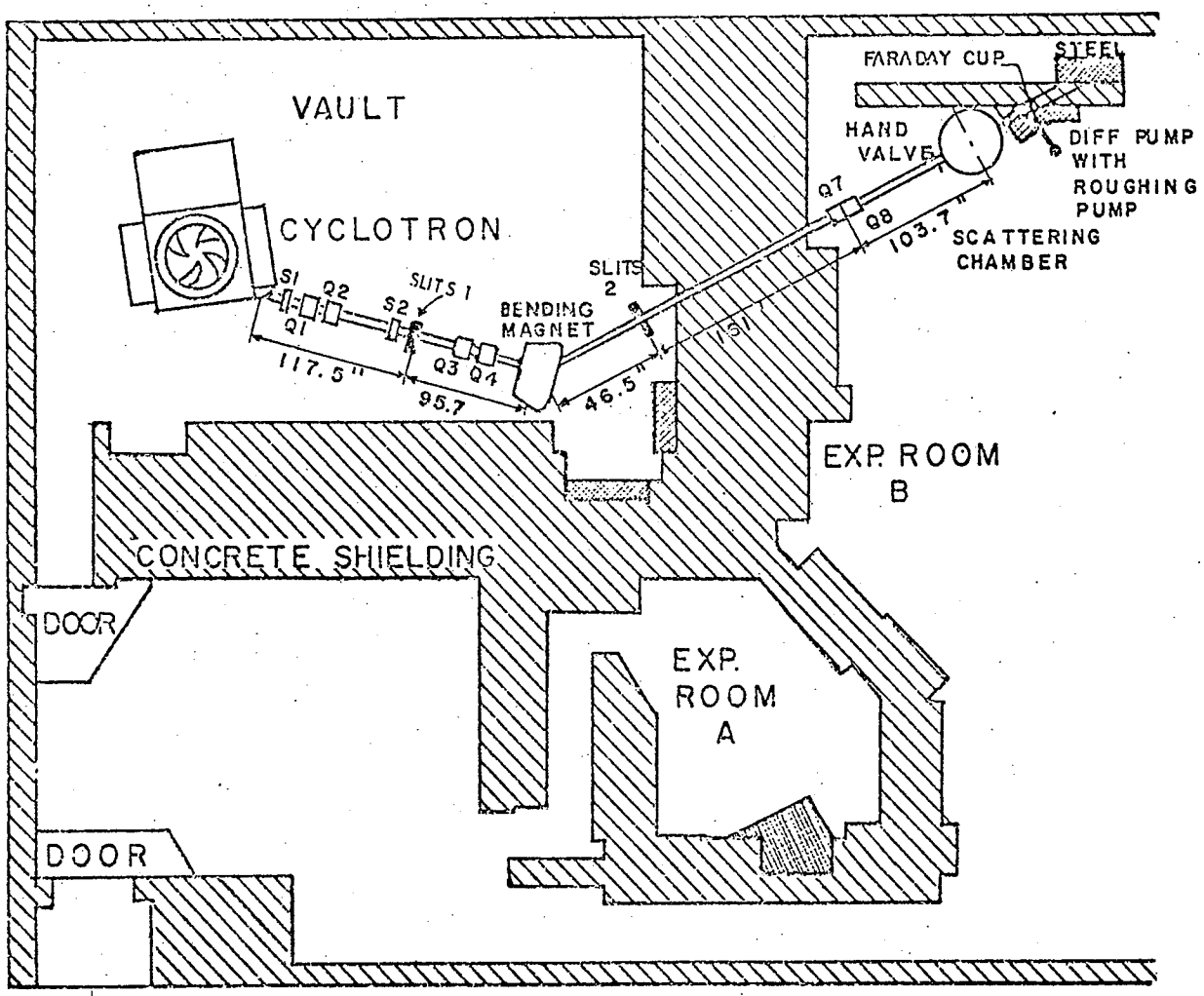
VAULT
CYCLOTRON
S1
Q2
SLITS 1
S2
Q1
BENDING MAGNET
SLITS 2
Q3 Q4
117.5"
95.7
46.5"
151
FARADAY CUP
STEEL
HAND VALVE
DIFF PUMP WITH ROUGHING PUMP
Q7
Q8
103.7"
SCATTERING CHAMBER
EXP. ROOM B
CONCRETE SHIELDING
DOOR
EXP. ROOM A
DOOR

Fig.4.2

The scattering chamber with the proton and the alpha particle detectors, the alpha particle detector is directly above the proton detector. The distances from the target to alpha particle detector and the proton detector are 11.8 cm and 8.7 cm respectively.

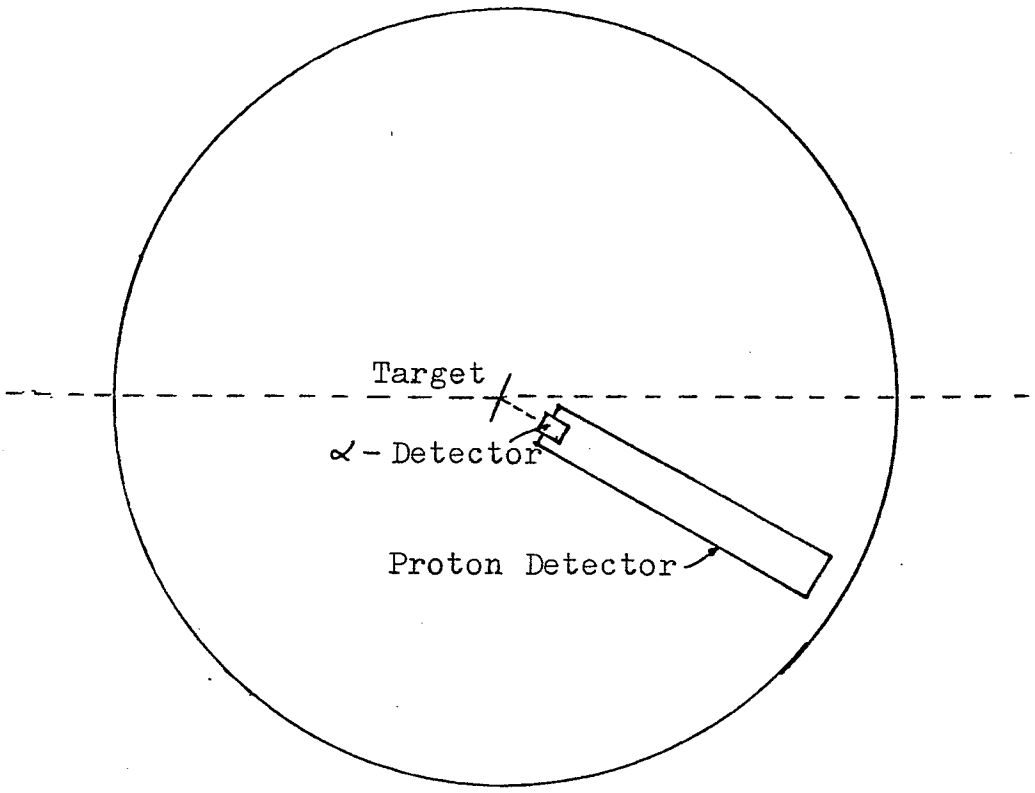
Target
∝ - Detector
Proton Detector

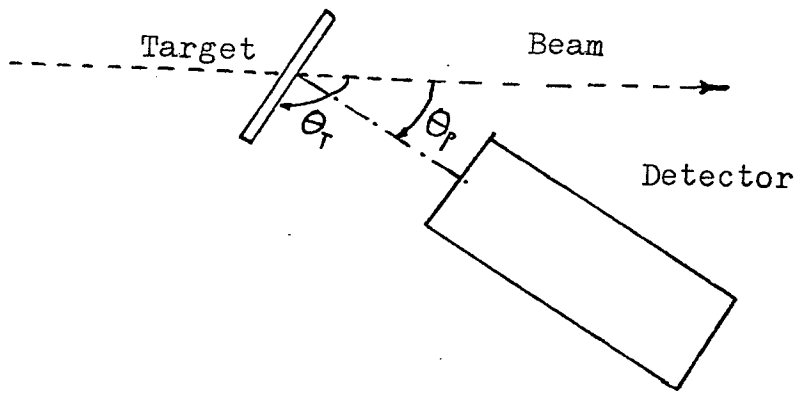

Fig.4.3 Target angles with respect to beam direction

to be 1.35×10^4 protons/sec.

IV.2 The Detection System

IV.2.a The Layout of the Detection System

A general description of the apparatus is given in this subsection; individual parts will be discussed in the following subsections. Fig4.4 shows a layout of the apparatus.

The design of the apparatus was based on the results described in the last chapter. The mean ^{6}Li outgoing angles and particle energies expected at various positions of the proton and alpha particle detectors, were known from the Monte Carlo calculations. It was found empirically and subsequently verified by calculation that placing the proton detector out of the scattering plane was not desirable. The following arrangement of the apparatus was judged the most satisfactory.

The plastic scintillation counter for protons was placed in the horizontal plane and was enclosed in a sealed brass cyclinder. Air was circulated through this cylinder casing by means of poly-flo tubing to act as a cooling agent for the photomultiplier and the base circuit. The high voltage cable for the photomultiplier was fed through the poly-flo tubing removing the need for high voltage vacuum feedthroughs. The proton counter

Fig.4.4

Layout of the appartus.

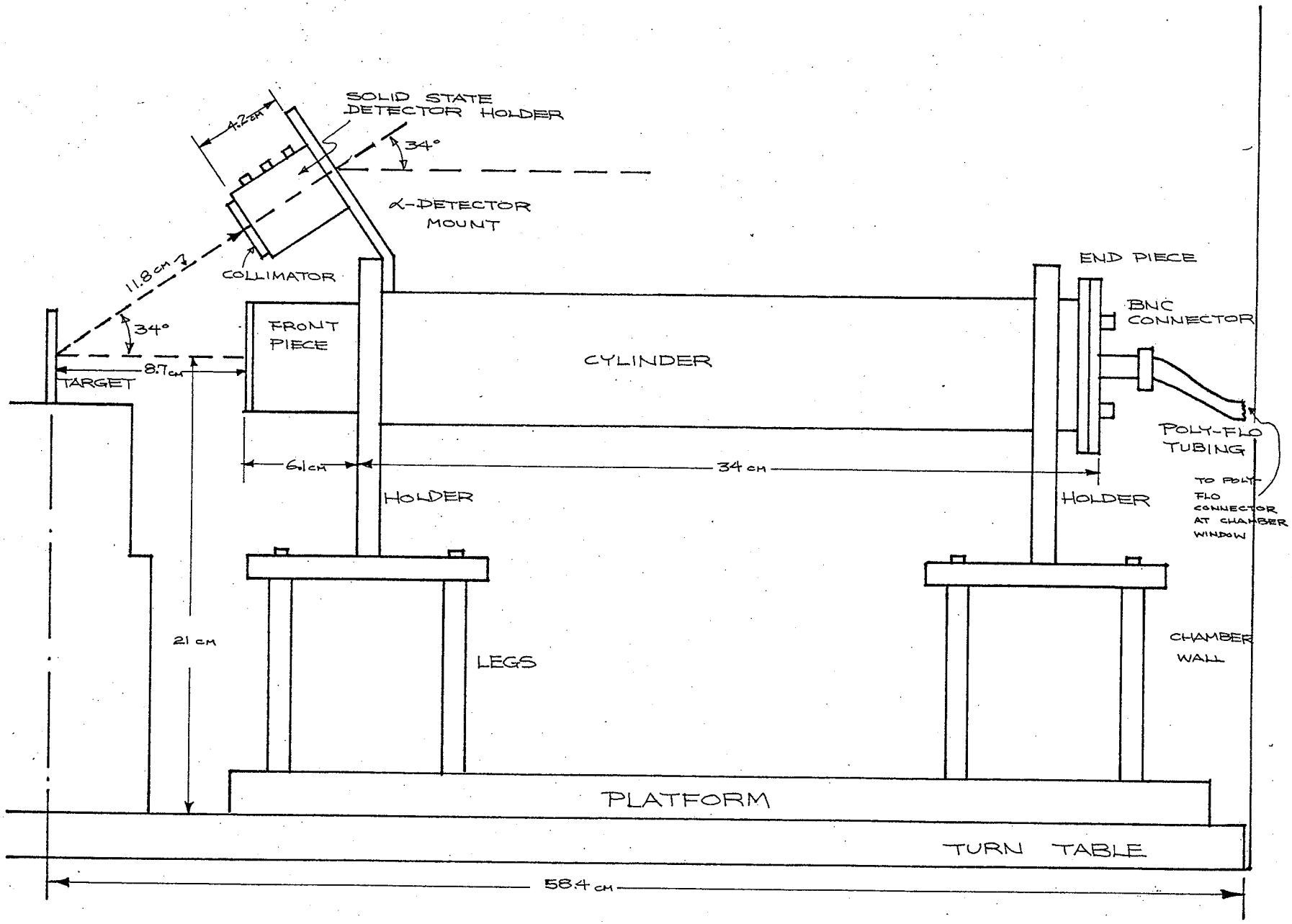
SOLID STATE
DETECTOR HOLDER
4.2 cm
34°
α-DETECTOR
MOUNT
11.8 cm
COLLIMATOR
34°
FRONT
PIECE
8.7 cm
TARGET
END PIECE
BNC
CONNECTOR
CYLINDER
POLY-FLO
TUBING
TO POLY
FLO
CONNECTOR
AT CHAMBER
WINDOW
6.1 cm
34 cm
HOLDER
HOLDER
21 cm
LEGS
CHAMBER
WALL
PLATFORM
TURN TABLE
58.4 cm

within the casing was then mounted on the platform of the turn table in the scattering chamber.

Above the proton counter an alpha particle telescope was mounted as shown in Fig.4.4. The telescope contained three solid state detectors, a 200μm ΔE detector, a 500μm E detector, and a 500μm veto detector. Using the ΔE and the E pulses, alpha particles could be distinguished from other particle types. The particle identification was performed on-line using computer software discussed in the following chapter. The purpose of the veto detector was to remove high energy particles, primarily protons, which could penetrate both the ΔE and E detectors.

The target used in this experiment was a CH_2 foil of thickness 2.96 mg/cm^2. A helium gas target was also used for setting up the timing and calibration.

IV.2.b The Proton Scintillation Counter

The layout of the proton counter is shown in Fig.4.5. This counter contained a cylindrical 4.0 cm diameter by 1.0 cm long NE102A scintillator, an EMI 9815B photomultiplier, a resistor chain, and a preamplifier. The system was totally enclosed in an air tight brass cylinder which was placed inside the scattering chamber. The collimator placed in front of the counter is shown in Fig.3.13. The size of this collimator was carefully considered as a compromise between a large solid angle

Fig.4.5

Section of the proton detector

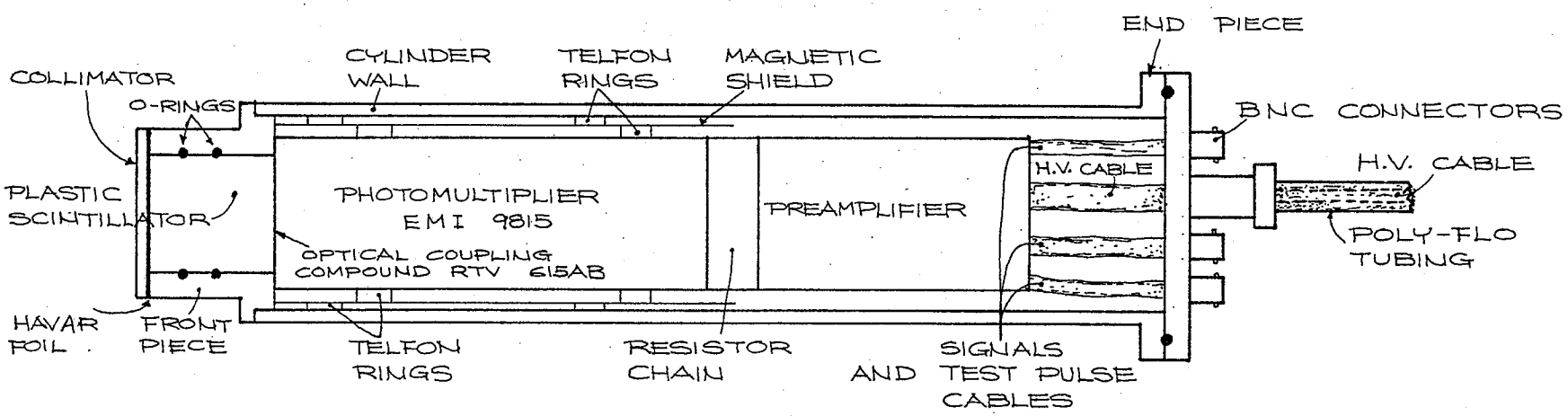
END PIECE
CYLINDER WALL
TELFON RINGS
MAGNETIC SHIELD
COLLIMATOR
O-RINGS
BNC CONNECTORS
H.V. CABLE
PLASTIC SCINTILLATOR
PHOTOMULTIPLIER EMI 9815
PREAMPLIFIER
H.V. CABLE
POLY-FLO TUBING
OPTICAL COUPLING COMPOUND RTV 615AB
HAVAR FOIL
FRONT PIECE
TELFON RINGS
RESISTOR CHAIN
SIGNALS AND TEST PULSE CABLES

and uniformity of scintillation response.

A havar foil of thickness .0038 cm was placed behind the collimator to act as a light seal, and to act as an absorber for the plastic scintillator. According to Gooding and Pugh (G0060) a thin absorber in front of a plastic scintillator can improve the linearity of response as a function of proton energy. This is because of the fact that the energy lost in the absorber by low energy particles is greater than that lost by high energy ones. This has the effect of straightening out the response curve but gives it a non-zero intercept on the proton energy axis. The effect of such an absorber is shown in the proton calibration curve in Fig.4.6.

Immediately behind the havar foil was the plastic scintillator. The scintillator compressed two O-rings as shown in Fig. 4.4. These O-rings acted as vacuum seals for the front end of the cylinder. The plastic scintillator was potted to the photomultiplier using General Electric RTV-615AB Optical coupling compound. The photomultiplier was held inside a magnetic shield by two telfon rings, and the magnetic shield was in turn supported inside the brass cylinder by two larger telfon rings.

A resistance chain and preamplifier were designed for use with the system. Both the resistance chain and preamplifier circuitry are shown in Figs. 4.7 and 4.8.

Fig.4.6

The calibration curves for both the proton (4.6a) and the alpha particle detector(4.6b). It is observed from the proton curve that if an absorber such as havar foil is placed in front of the plastic scintillator, the calibration curve is linear down to at least 10 MeV, but that a non-zero intercept on the energy axis is obtained.

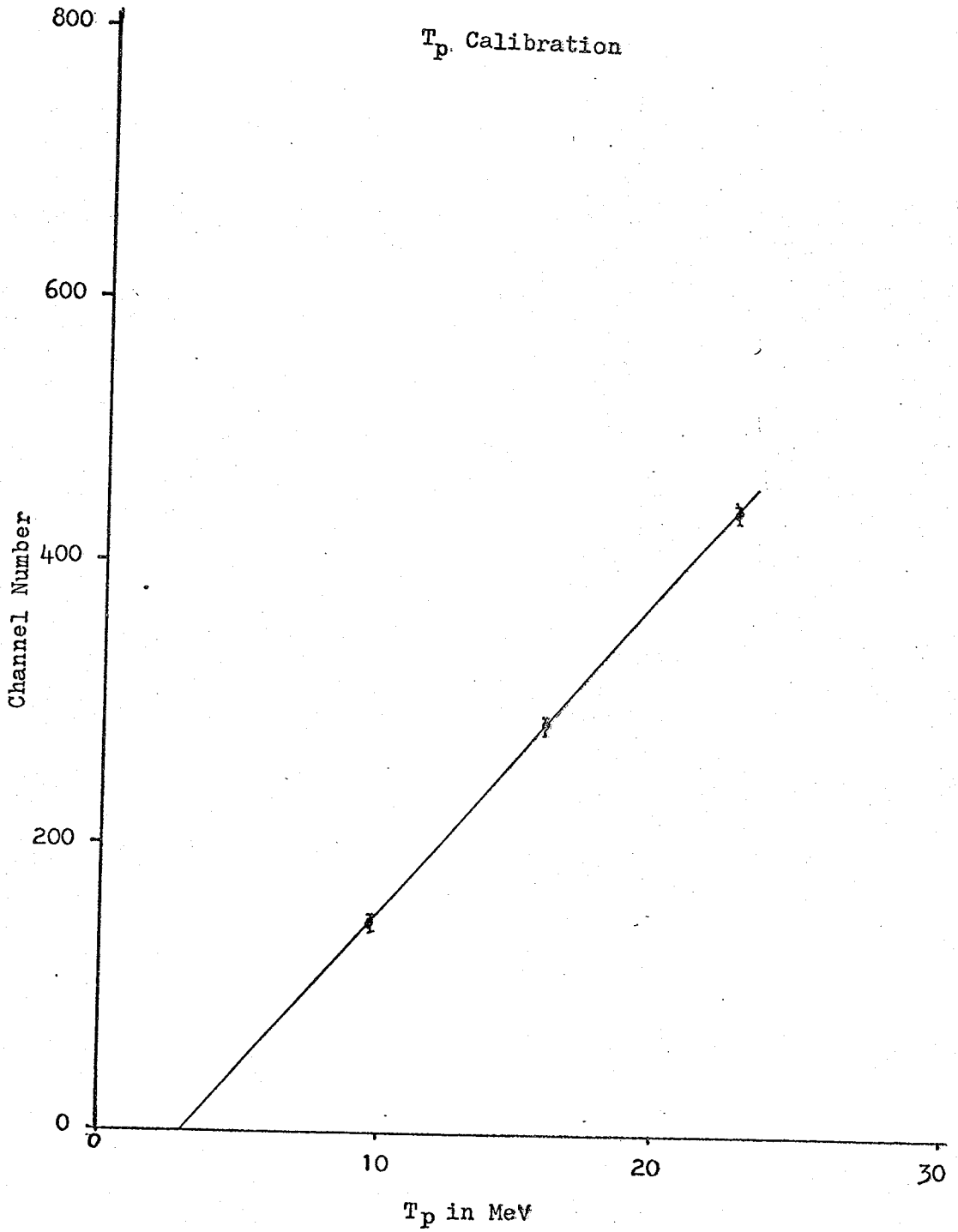
T_p Calibration
800
600
400
200
0
Channel Number
0
10
20
30
T_p in MeV

Fig.4.6a

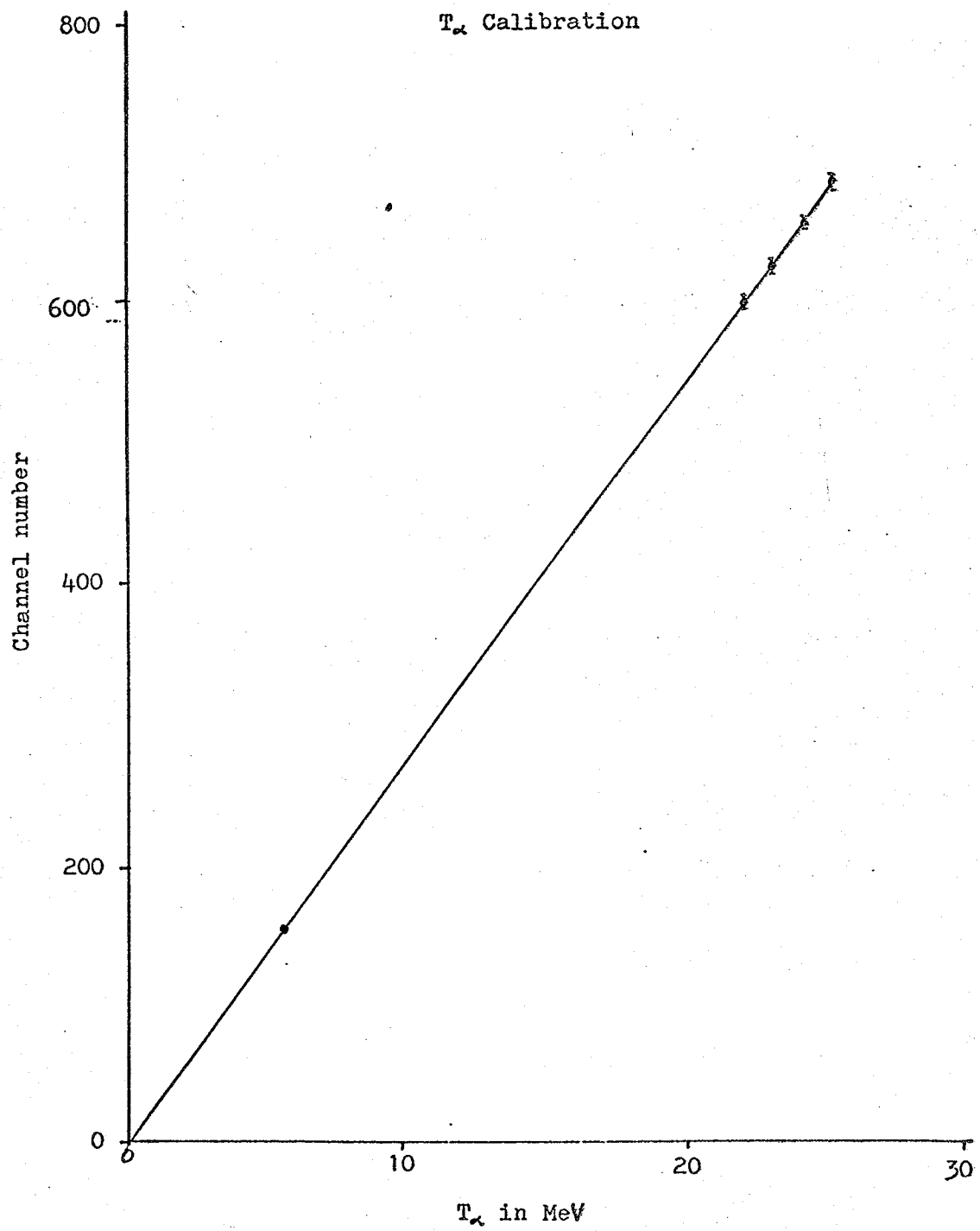
T_α Calibration
800
600
400
200
0
Channel number
0
10
20
30
T_α in MeV

Fig.4.6b

Fig.4.7

Preamplifier circuit for the photomultiplier.

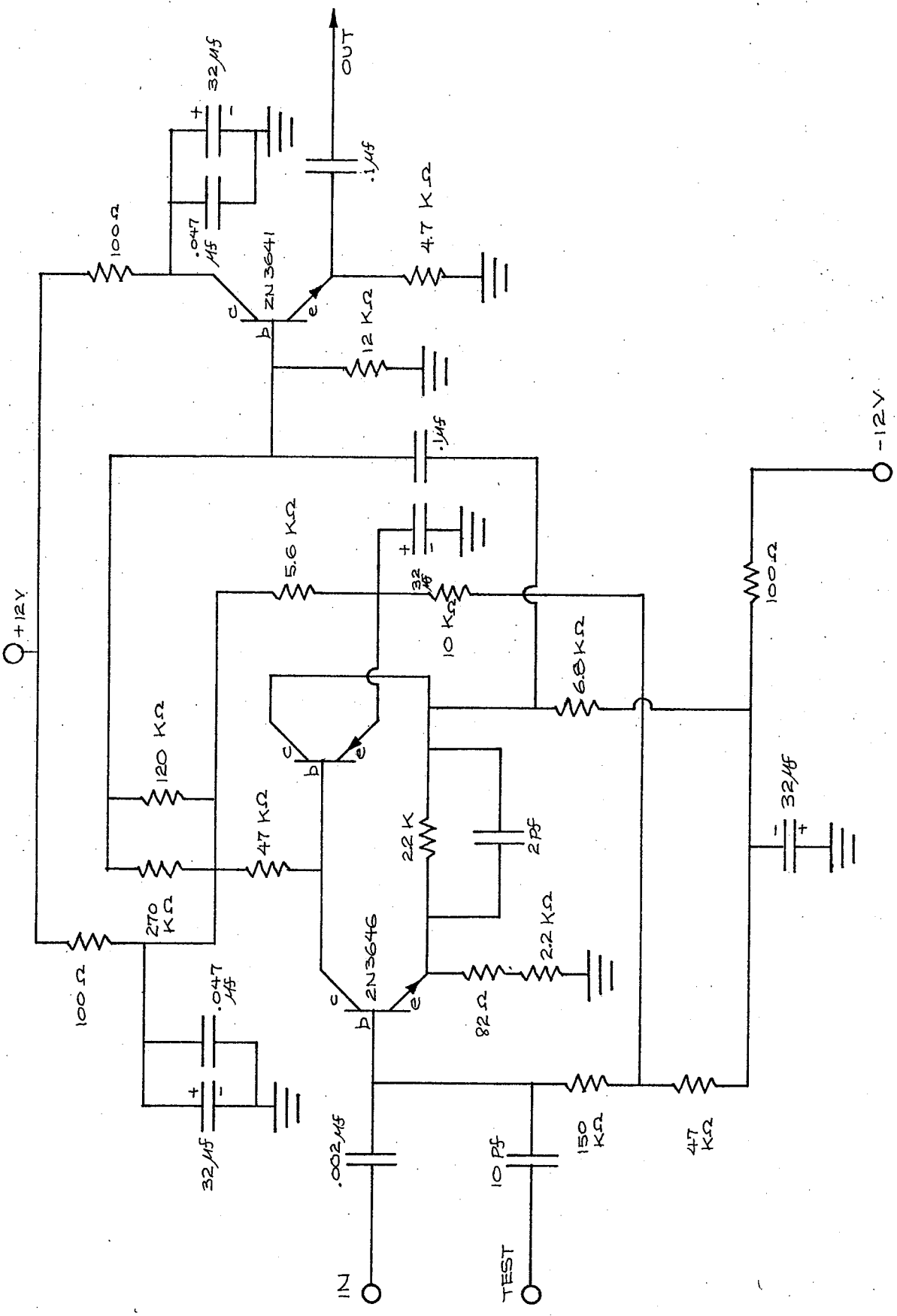
OUT
32 μf
.047 μf
.1 μf
100 Ω
4.7 KΩ
2N3641
12 KΩ
.1 μf
-12 V
+12 V
5.6 KΩ
32 μf
10 KΩ
100 Ω
6.8 KΩ
120 KΩ
32 μf
47 KΩ
22 K
2 pf
270 KΩ
2.2 KΩ
2N3646
82 Ω
100 Ω
.047 μf
32 μf
.002 μf
10 pf
150 KΩ
47 KΩ
IN
TEST

Fig.4.8

The resistance chain for the photomultiplier.

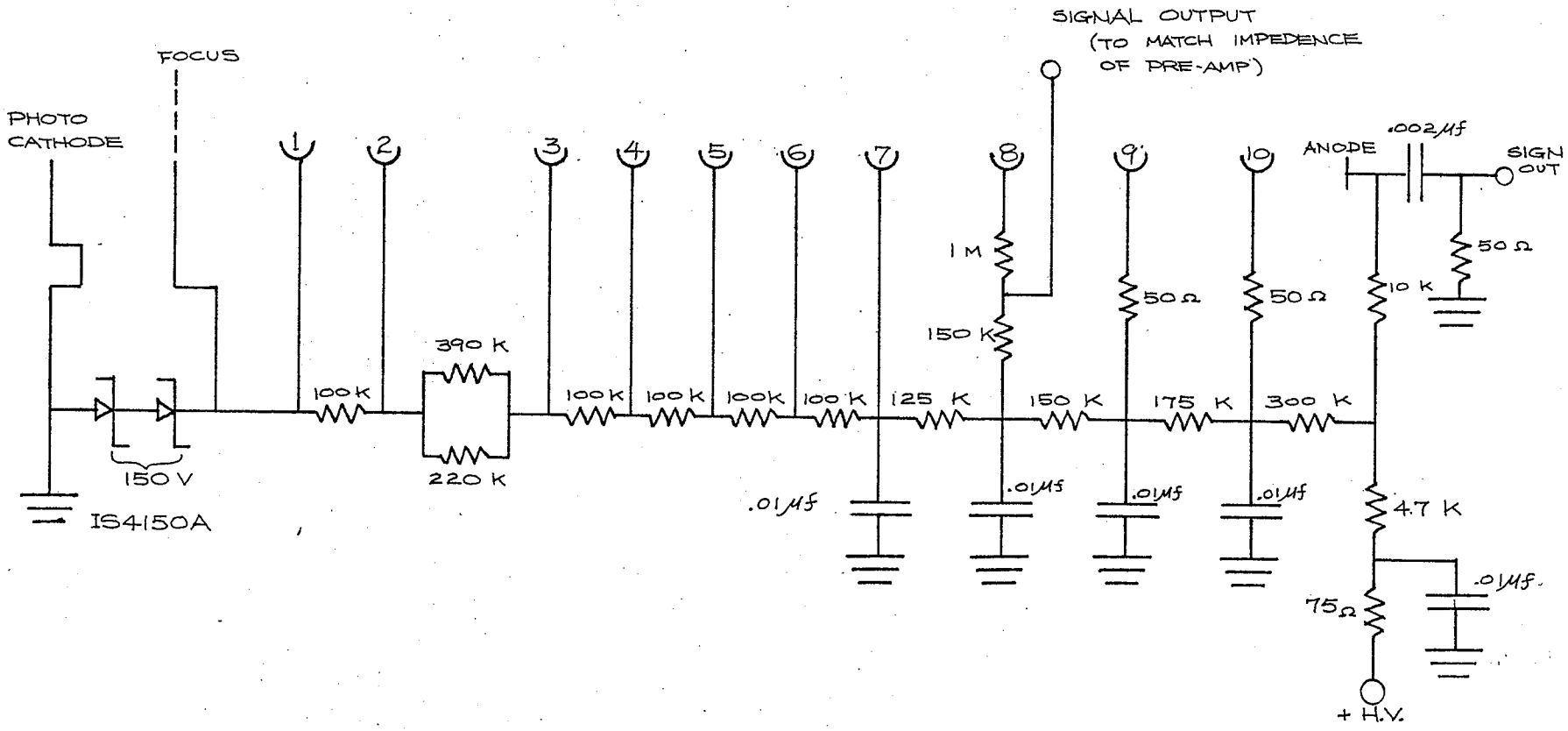
SIGNAL OUTPUT
(TO MATCH IMPEDENCE
OF PRE-AMP)
FOCUS
PHOTO
CATHODE
1
2
3
4
5
6
7
8
9
10
ANODE
.002μf
SIGN
OUT
1M
150 K
50 Ω
50 Ω
50 Ω
10 K
100 K
390 K
100 K
100 K
100 K
100 K
125 K
150 K
175 K
300 K
150 V
220 K
IS4150A
.01μf
.01μf
.01μf
.01μf
.01μf
4.7 K
75Ω
+ H.V.

The preamplifier featured two signal outputs. The output from the anode was for timimg purposes, while the other output from the eighth dynode was used for pulse height measurement. Such features were required because of the high counting rate of the protons elastically scattered from the carbon target. A test pulse input was also included in the preamplifier.

IV.3 The Electronics

A block diagram of the electronics used in this experiment is shown in Fig. 4.9. The electronic circuitry contained three sections: the proton arm, the alpha arm, and the timing portion.

The alpha arm contained 3 detectors: the ΔE, the E, and the VETO detectors. The signals from these three detectors were first amplified by ORTEC 109A preamplifiers placed next to the scattering chamber. Outputs from these preamplifiers were then sent by cable to the control room where the major electronics racks and PDP15/40 computer were located. These signals were amplified by CANBERRA 1416 amplifiers. The ΔE signal was increased by a factor of 4 over that of the E detector in order to make full use of the dynamic range (300 millivolts to 10 volts) of most of the electronic modules. This signal was then decreased by the same factor of 4 before it was added to the E signal. The

Fig.4.9

Schematic block diagram of the electronic circuitry used for data collection.

AMP: Amplifier

COINC: Coincidence unit

DA: Delay amplifier

CFD: constant fraction discrimator

DSI: Dual sum inverter

5FLOG: 5 fold logic

GDG: Gate and delay generator

D: Delay

QUAD DISC: Quad discrimator

PUG: Pile up gate

PRE AMP: Preamplifier

TAC: Time to amplitude converter

TFA: Timeing filter amplifier

SCA: Single channel analyzer

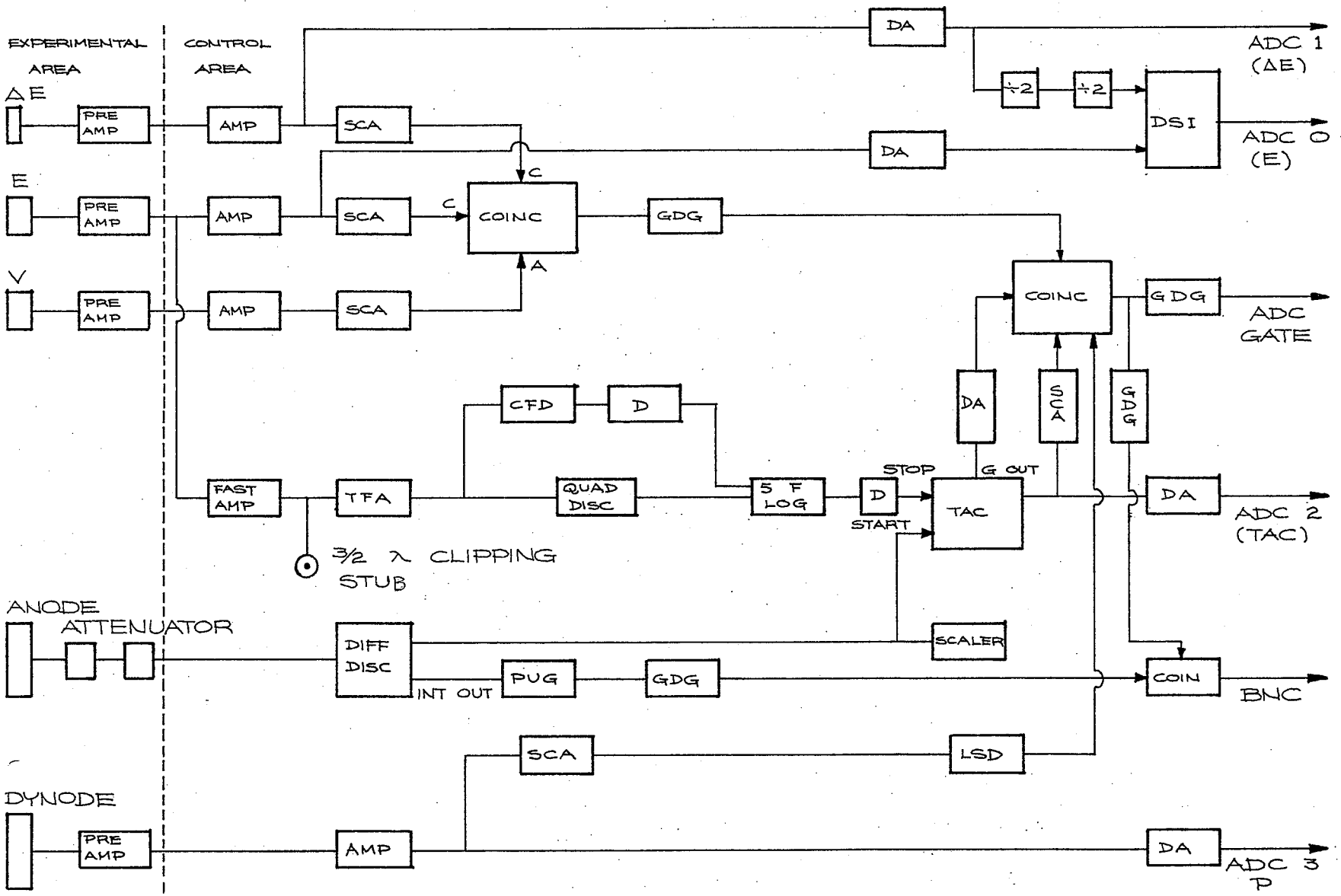
EXPERIMENTAL AREA
CONTROL AREA
ΔE
E
V
PRE AMP
AMP
SCA
DA
÷2
÷2
DSI
ADC 1 (ΔE)
ADC 0 (E)
C
A
COINC
GDG
ADC GATE
CFD
D
FAST AMP
TFA
QUAD DISC
5 F LOG
STOP
START
G OUT
TAC
ADC 2 (TAC)
3/2 λ CLIPPING STUB
ANODE
ATTENUATOR
DIFF DISC
INT OUT
PUG
SCALER
COIN
BNC
DYNODE
LSD
ADC 3 P

signals from the three detectors were all connected to a coincidence module where the ΔE and E signals were set in coincidence mode while that from the veto detector was set in anti-coincidence mode. The output was used later in the main coincidence module which controlled the gate on the ADC.

The proton arm contained two inputs. The pulse height signal from the photomultiplier dynode was first amplified by the preamplifier discussed in the previous section. This signal was then patched from the experimental area by a CI1416 amplifier. After this signal passed through an SCA it was connected to the main coincidence unit.

The timing signals were derived from the anode of the proton counter and the E detector of the alpha particle telescope. It is known that cyclotron radio frequency (RF) picked up by the fast signal cables is an important noise source. In order to eliminate this RF noise, the timing signal from the E detector was fed into a fast amplifier (Le Croy 133) whose output was connected to a timing filter amplifier (TFA ORTEC 463). At this connection a T connector allowed a clipping stub to be connected as shown in Fig. 4.9. The clipping stub was a 50Ω RG-8 cable shorted at one end. Its length was 3/2 wavelengths of the signal from the cyclotron oscillator. Reflected signals from this clipping stub would therefore

cancel the incoming RF noise at the T connector. The improved timing signal was then amplified by the timing filter amplifier before entering the constant fraction discriminator (CFD ORTEC 463). During the experiment however a difficulty with "WALK" arose. It was therefore necessary to include a QUAD Discriminator (QUAD DISC. EG&G T140/N) and a 5 fold logic (LRS163)as shown in Fig. 4.9. The output of the 5 fold logic was then used as the STOP pulse for the Time to Amplitude Converter (TAC). The START pulse came from the proton arm. The signal from the anode of the photomultiplier was first attenuated in the experimental area and then was sent to a differential discriminator (DIFF.DIS. EG&G TD101/N) in the control room. The INT. output from the DIFF.DIS. was used for measuring pile up events. The output from the DIFF.DIS. was used as a START pulse to trigger the TAC. A timing resolution less than the 35 nanosecond separation of the cyclotron beam bursts was obtained, thus allowing clear separation of the "REAL" and "RANDOM" coincidence peaks as shown in Fig. 4.10. The output of the TAC was then connected to the main coincidence circuit. The main coincidence opened the ADC gate to the computer if the signal from the alpha arm, the proton arm, and the TAC were in coincidence. A final adjustment was made to all the linear signals so that they arrived at the ADC's simultaneously.

Fig.4.10

The TAC spectrum. The centre peak is the "real+random" coincidence peak. The other 6 small peaks are the random peaks.

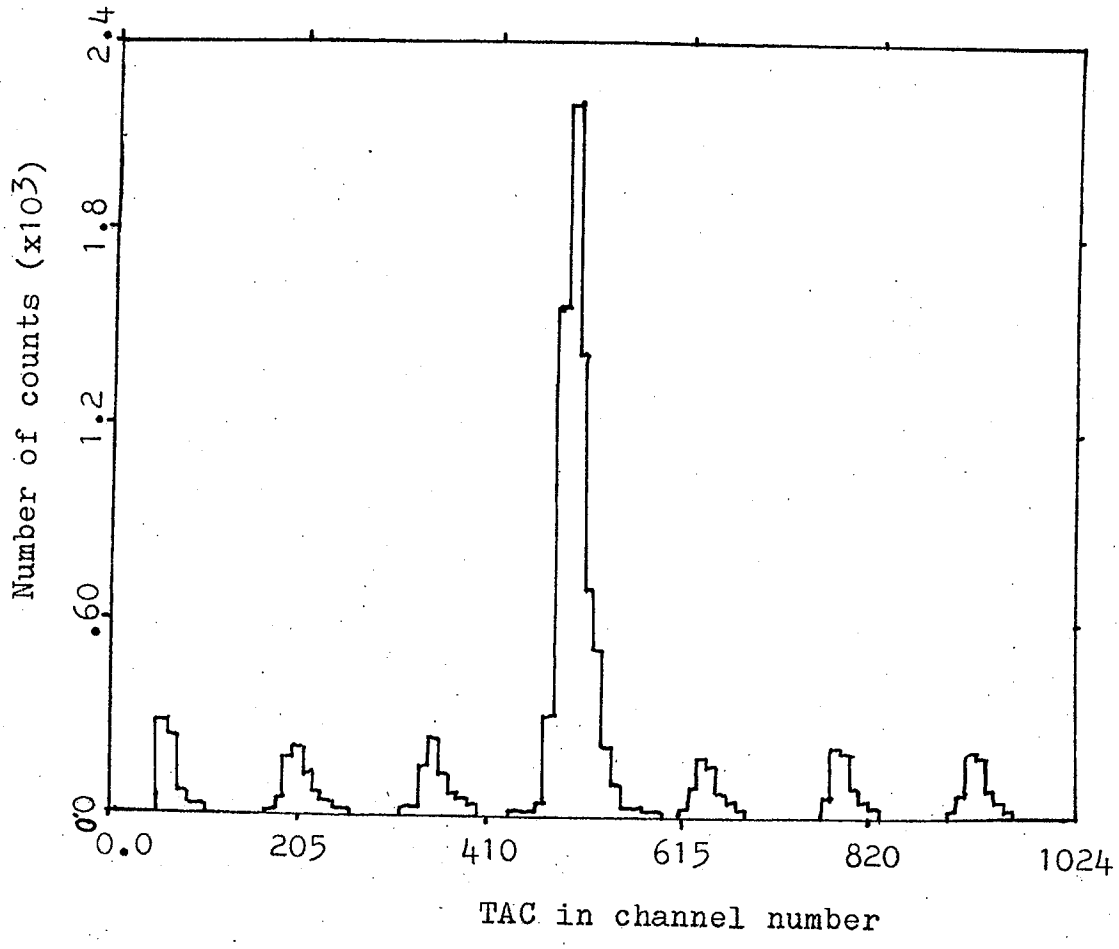
Number of counts (x10³)
2.4
1.8
1.2
.60
0.0
0.0
205
410
615
820
1024
TAC in channel number

IV.4 Experimental Procedures

The following procedures were carried out before and during data collections.

(1) Beam Optics Adjustments: The beam spot was adjusted until it was properly centred and had a size less than 3mm wide by 6mm high.

(2) Gain Matching for the ΔE and E detectors:

A crude matching of the gain of the ΔE and E amplifiers was first obtained using a pulser. A more accurate matching of the gains was obtained using an alpha particle source.

(3) Energy Calibrations for both the scintillation counter and solid state detectors:

The energy calibration of the alpha telescope was first obtained with a known source of alpha particles, then with the $^{12}C(p,\alpha)^{9}Be$ reaction. The proton energy calibration was obtained using $^{12}C(p,p)^{12}C$ and $H(p,p)H$ scatterings. Halfway through the experiment a second calibration was performed as a check for electronic drifts. The calibration curves are shown in Fig. 4.6.

(4) Timing adjustments:

The timing of the electronics was initially set up using a pulser, then refined using protons and alpha particles from $^{4}He(p,p)^{4}He$ scattering. A helium gas cell was used as the target. The proton counter was placed at 118° on one side of the chamber while the alpha particle teles-

cope was placed at 25° on the other side as shown in Fig.4.11. These positions correspond to 180° separation between proton and alpha particle directions in the centre of mass system resulting in a high rate of real coincidence. The coincident proton and alpha particle could then be used for timing purposes. The energy of alpha particles at 25° lab. is 20.3 MeV while that of protons is 17.8 MeV for an incident proton energy of 38.23 MeV. The alpha particle energy corresponded well to the energy range expected for alpha particles coming from ^{5}Li breakup following a $^{12}C(p,^{5}Li)^{8}Be$ reaction. However the elastically scattered protons have higher energies than that expected from the ^{5}Li breakup. The expected proton energy range in the latter case is from 5 MeV to 12 MeV.

During the experiment the TAC spectrum was collected and was checked from time to time to ensure that the windows set on the real and random peaks had not shifted significantly. Fig.4.10 shows a typical TAC spectrum. The TAC spectrum contained 6 random coincidence peaks and a large peak containing real plus random coincidences. From this spectrum the timing resolution of the TAC was found to be about 8 nanoseconds. The ratio of the number of real plus random events to the number of random events alone was about 4.5 to 1.

(5) Data collection:

Fig.4.11

Layout of the proton and alpha particle detectors for timing adjustment. The distances from the target to the alpha particle detector and the proton detector are 11.8 cm and 8.7 cm respectively. The proton collimator is shown in Fig.3.13, and the alpha particle detector has a slit collimator of size 10 mm by 4 mm.

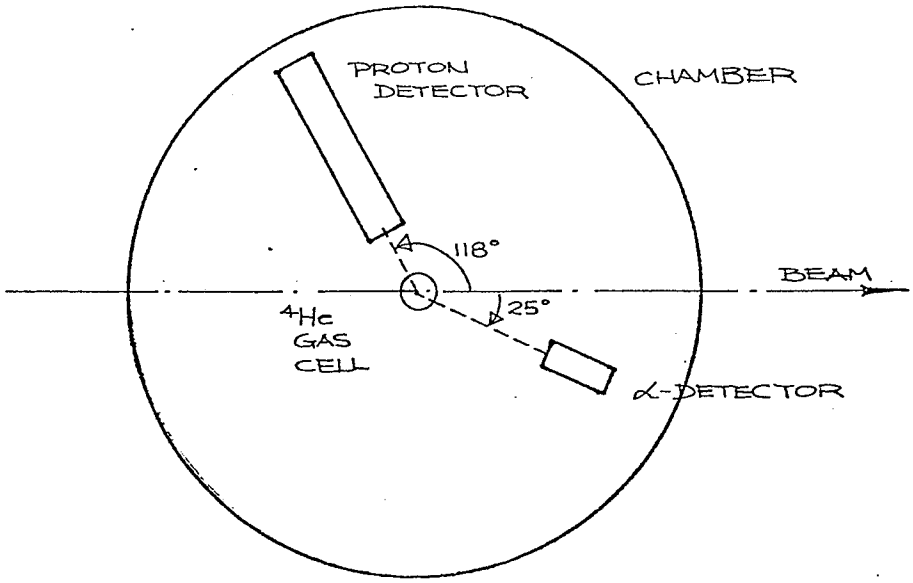
PROTON
DETECTOR
CHAMBER
118°
BEAM
25°
^{4}He
GAS
CELL
α-DETECTOR

Data acquisition was performed using the computer program MULPAR which will be discussed in detail in the next chapter. The data were stored event by event on magnetic tapes and the analysis was subsequently carried out off-line using a IBM370 computer and the program CORMAG which will be also discussed in detail in the following chapter.

V. Analysis and Results

V.1 Data Acquisition

Data acquisition was performed using the PDP computer program MULPAR (an acronym for multi-parameter) in conjunction with an external application-dependent processing routine GPYEE written for this experiment. This routine was capable of using particle identification loci to determine whether the particle was a proton or an alpha particle, and whether the energy was within a specified range. It was also capable of performing simple calculations on the parameters.

Those events that passed the operator-specified tests could be used in accumulating 2 dimensional spectra for display on the CRT screen either as a 64x64 differential contour display or as a 512x512 "twinkle" display. The variables on the axis might be chosen to be any of the ADC inputs or simple functions of the inputs generated by GPYEE. A Moseley plotter could also be used to produce on-line scatter plots of the currently displayed two dimensional spectrum. Fig.5.1 shows typical scatter plots of the two dimensional displays generated off-line during subsequent analysis. Each point plotted represents one recorded event. With suitable commands data could be recorded on a magnetic tape for subsequent off-line analysis.

Fig.5.1

The raw data scatter plots. (5.1a) shows the raw data without any constraints. It appears that there is a gap at around channel 256 of T_{α}. This gap cuts the data into two sections. Fig.5.1b shows the raw data when only the alpha particle and the real coincidences are accepted. From Fig.5.1b it is seen that the lower section in Fig.5.1a is mainly due to random and false coincidences.

Fig.5.1a

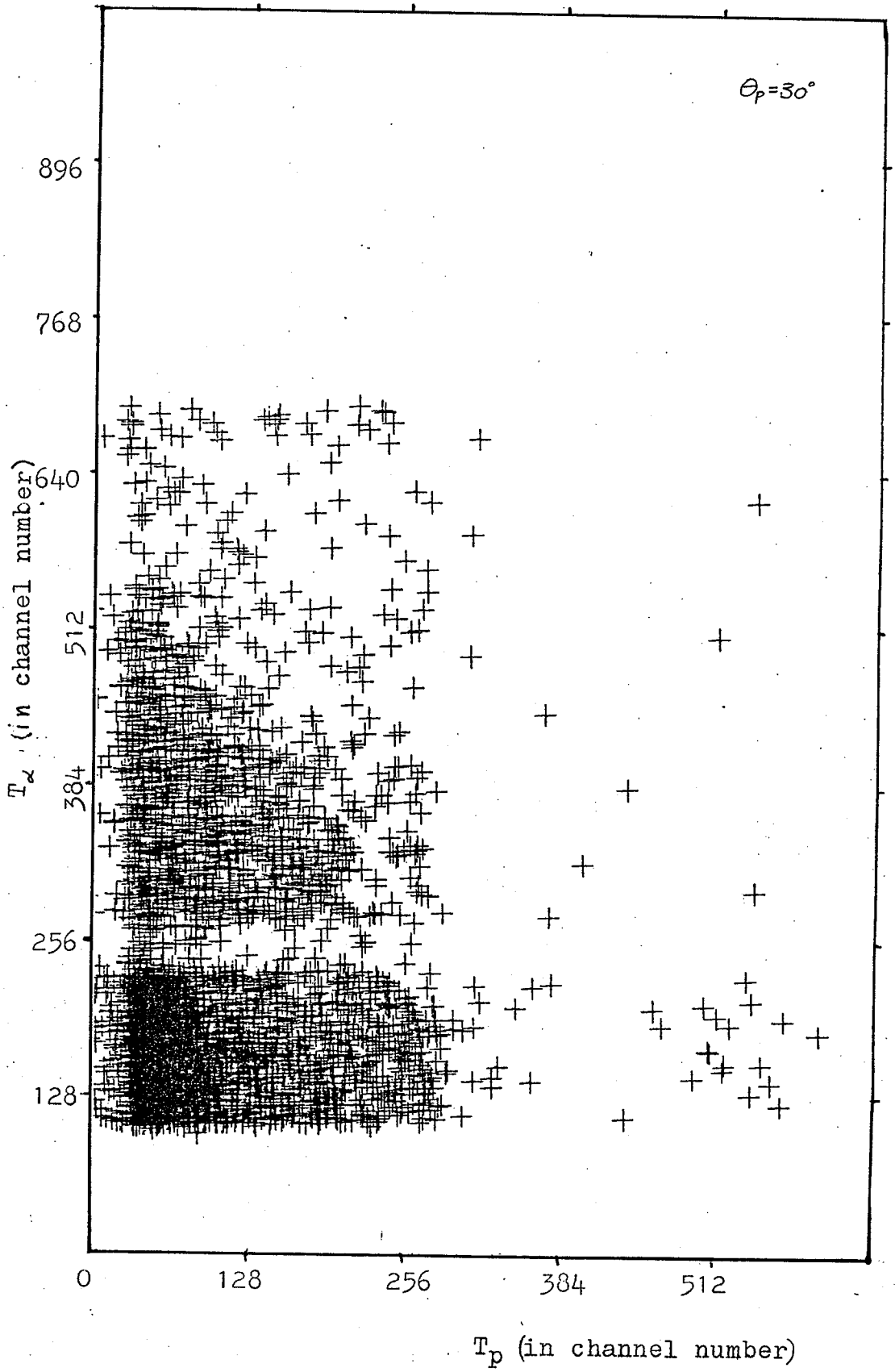
θ_p=30°
896
768
640
512
384
256
128
0
128
256
384
512
T_α (in channel number)
T_p (in channel number)

Fig.5.1b

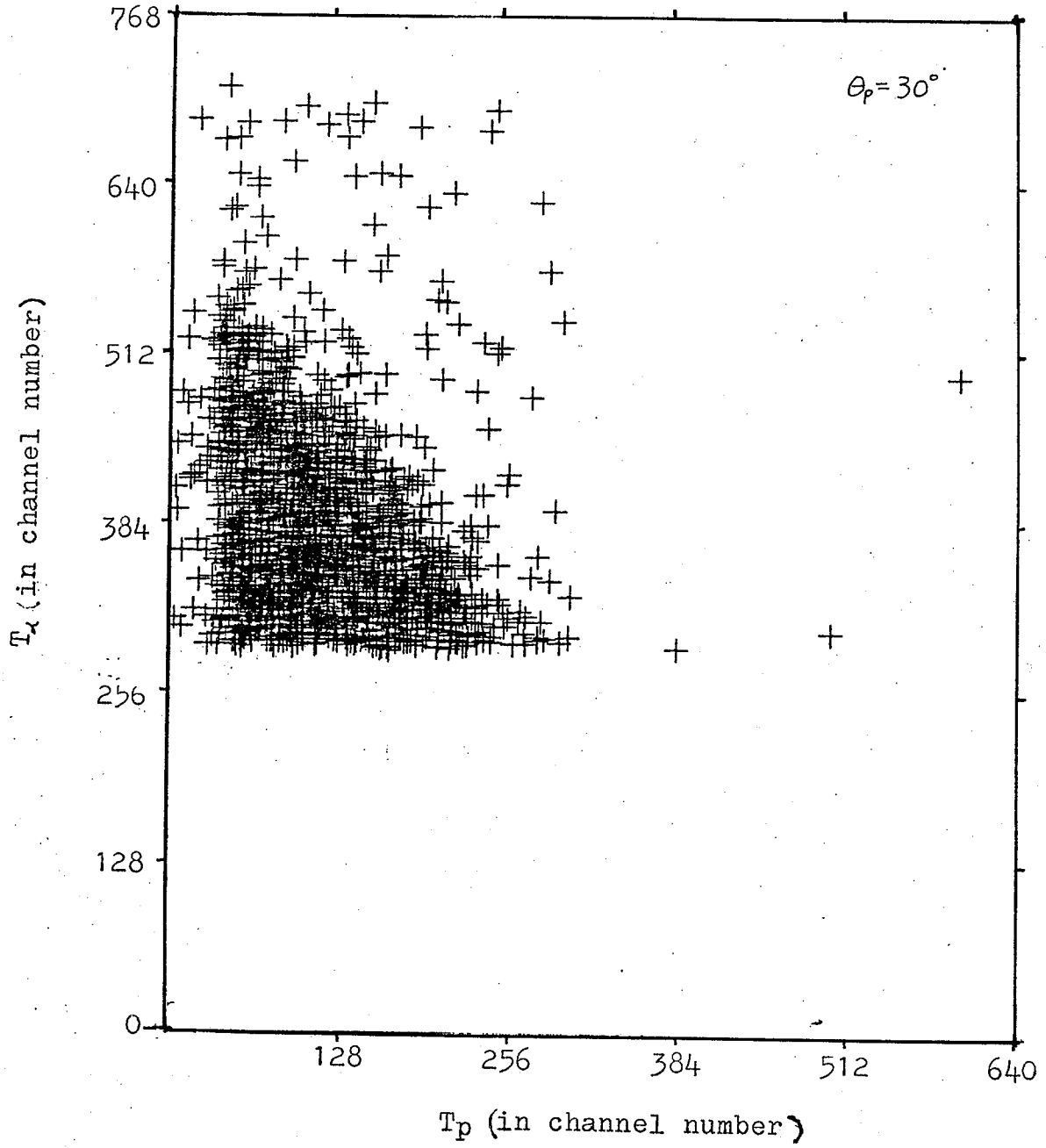
768
640
512
384
256
128
0
128
256
384
512
640
$\theta_p = 30°$
T_α (in channel number)
T_p (in channel number)

The program MULPAR was used mainly for a rough analysis and display during the experiment. A similar PDP program PETE with the same external subroutine GPYEE was used in preliminary analysis. However a more accurate analysis was done using the FORTRAN program CORMAG run on an IBM370 computer. An outline of these programs is discussed in the following section.

V.2 Data Reduction

Off-line data reduction was performed using the computer program CORMAG. This program could perform the same tasks as MULPAR, but could also make single histograms, double histograms (two dimensional histograms), and scatter plots of specified variables with a set of constraints (or tests) for each individual histogram or plot. There was also a facility in this program for subtracting randoms out of a scatter plot. CORMAG could keep track of up to 80 constraints for each individual histogram and up to 16 variables per event might be printed on the line printer for the first 100 events which passed the set of constraints specified. This feature provided means of testing the agreement between CORMAG and MULPAR and of testing the correctness of the processed variables.

Fig.5.2a shows a scatter plot of ΔE vs E such as was used for particle identification. There is a clear

134

Fig.5.2

Scatter plots of ΔE vs E. Fig.5.2a shows the plot without any particle identification constraint. Different types of particles are labelled in the plot. It can be seen that the particles are clearly separated. Fig.5.2b shows the plot with a particle identification constraint applied so that only alpha particles are accepted.

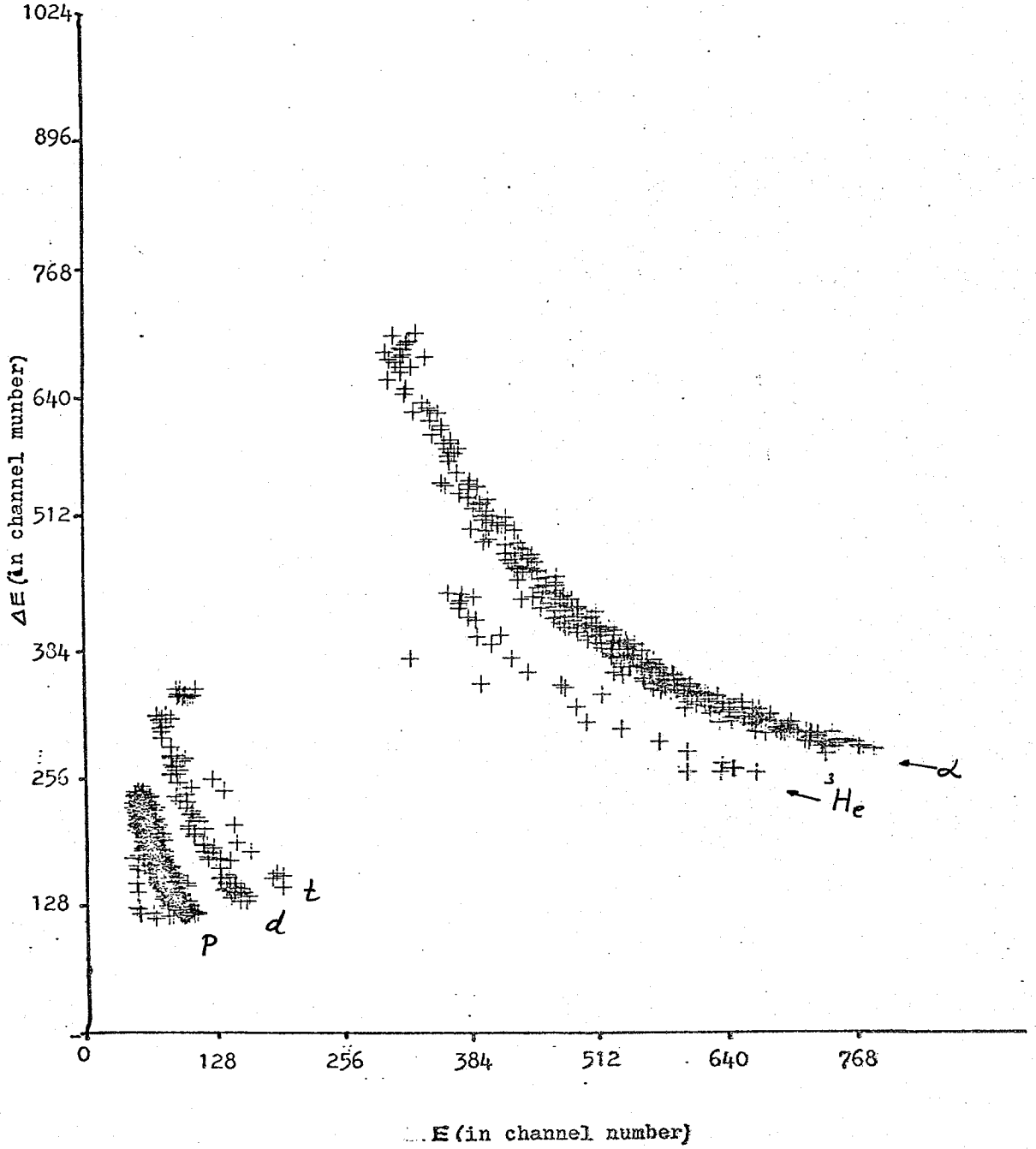
1024
896
768
640
512
384
256
128
0
128
256
384
512
640
768
ΔE (in channel number)
E (in channel number)
p
d
t
α
^3He

Fig.5.2a

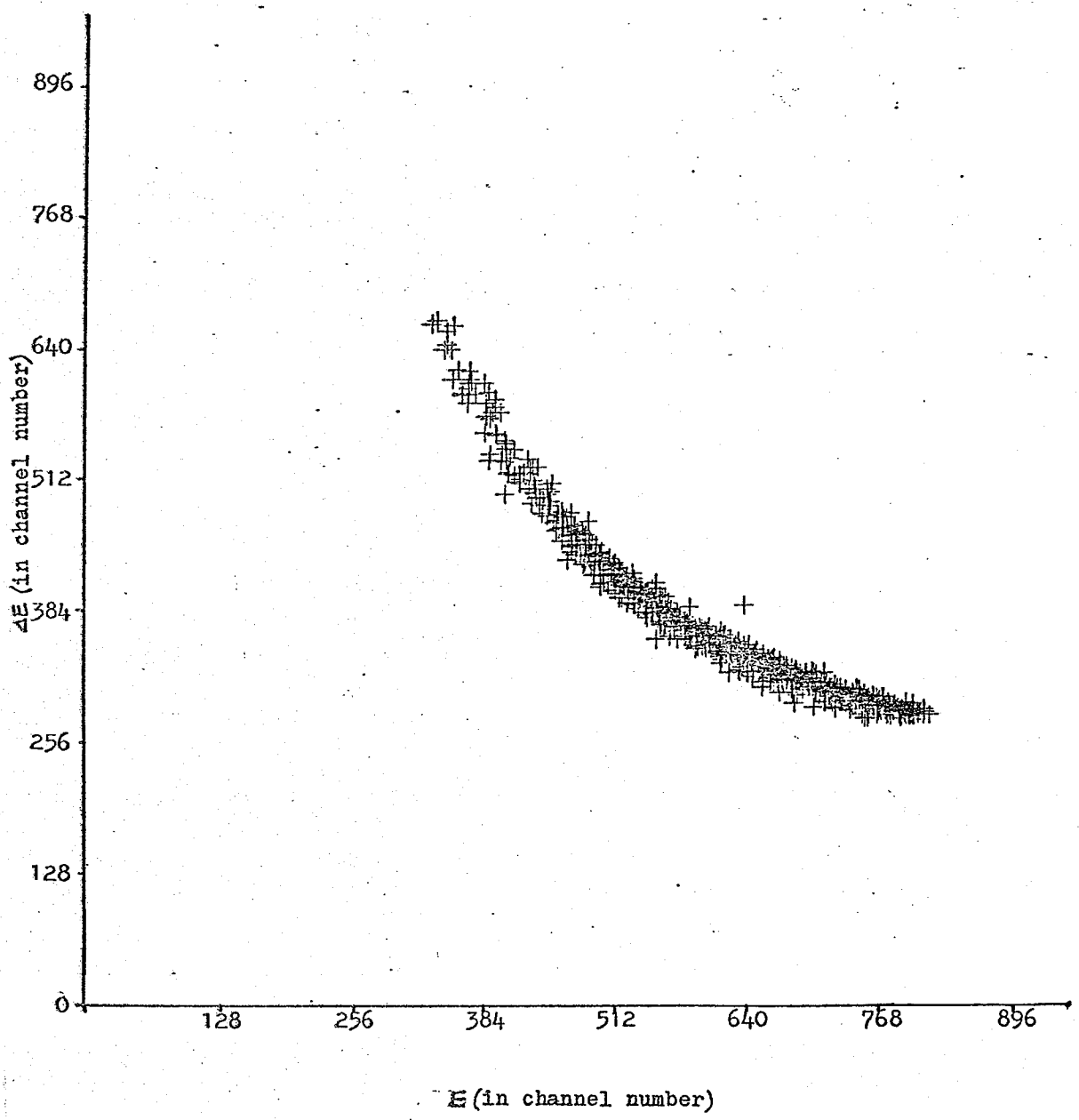
896
768
640
512
384
256
128
0
ΔE (in channel number)
128
256
384
512
640
768
896
E (in channel number)

Fig.5.2b

separation of particle types and with loci drawn about the alpha particle band, the other particles could be eliminated as shown in Fig.5.2b.

V.3 Technique and Analysis

The reaction mechanism leading to a four body final state such as $^{12}C(p,p\alpha)\alpha\alpha$ can be investigated by means of a Dalitz plot, (i.e. T_α vs T_p plot). A number of proton induced reactions on ^{12}C have a proton and three alpha particles in the final state. These reactions can be divided into three groups:

(1) $p+^{12}C \rightarrow p+3\alpha$

$p+^{12}C \rightarrow p+\alpha+^{8}Be \rightarrow p+3\alpha$

(2) $p+^{12}C \rightarrow p+^{12}C^* \rightarrow p+3\alpha$

$p+^{12}C \rightarrow \alpha+^{9}B^* \rightarrow p+3\alpha$

(3) $p+^{12}C \rightarrow {}^{5}Li+^{8}Be \rightarrow p+3\alpha$

All these reactions involve four bodies in the final state. However they can be distinguished on a Dalitz plot. Group (1) involves the direct production of either a three body or four body final state. If the three body final state is plotted on a Dalitz plot, the events fall on a locus as shown in Fig.2.2. For the four body final state however, the events can fall anywhere within a region limited by the four body continuum boundary. The four body final state might be considered as a series of three body loci with varying relative energies of the

undetected two body system. Four body final state events are allowed anywhere inside the boundary locus in the T_α vs T_p plot. Group (2) involves a two body reaction with sequential decay of one of the particles. When the data from such a reaction are plotted in a Dalitz plot, there will be concentrations of events at specific values of T_α or T_p depending on whether a proton or an alpha particle is produced. This is because of the fact that when a proton or an alpha particle is produced initially in a two body reaction, its energy has a definite value. This value corresponds to a constant value of either T_α or T_p in a Dalitz plot. Group (3) involves the two body reaction $p+^{12}C \rightarrow {}^{5}Li+{}^{8}Be$ followed by two body decays of ^{5}Li and ^{8}Be. Since this reaction involves initially a two body reaction, the energy of ^{5}Li is well defined and so is the breakup Q-value. These well defined values of ^{5}Li energies give rise to concentrations of points along the lines of constant $T_\alpha+T_p$ according to

$$T_\alpha+T_p = T_{Li}+Q$$

Here T_{Li} has a fixed value for a given ^{5}Li outgoing angle. The distribution of these events on a Dalitz plot is shown in Fig.5.3. The spread in the $^{12}C(p,{}^{5}Li)^{8}Be$ region is due to the mass uncertainty of ^{5}Li and the angle of breakup of ^{5}Li with respect to the direction of motion of the ^{5}Li.

The analysis of data made use of these features.

Fig.5.3

The distributions of the events due to different reaction mechanisms.

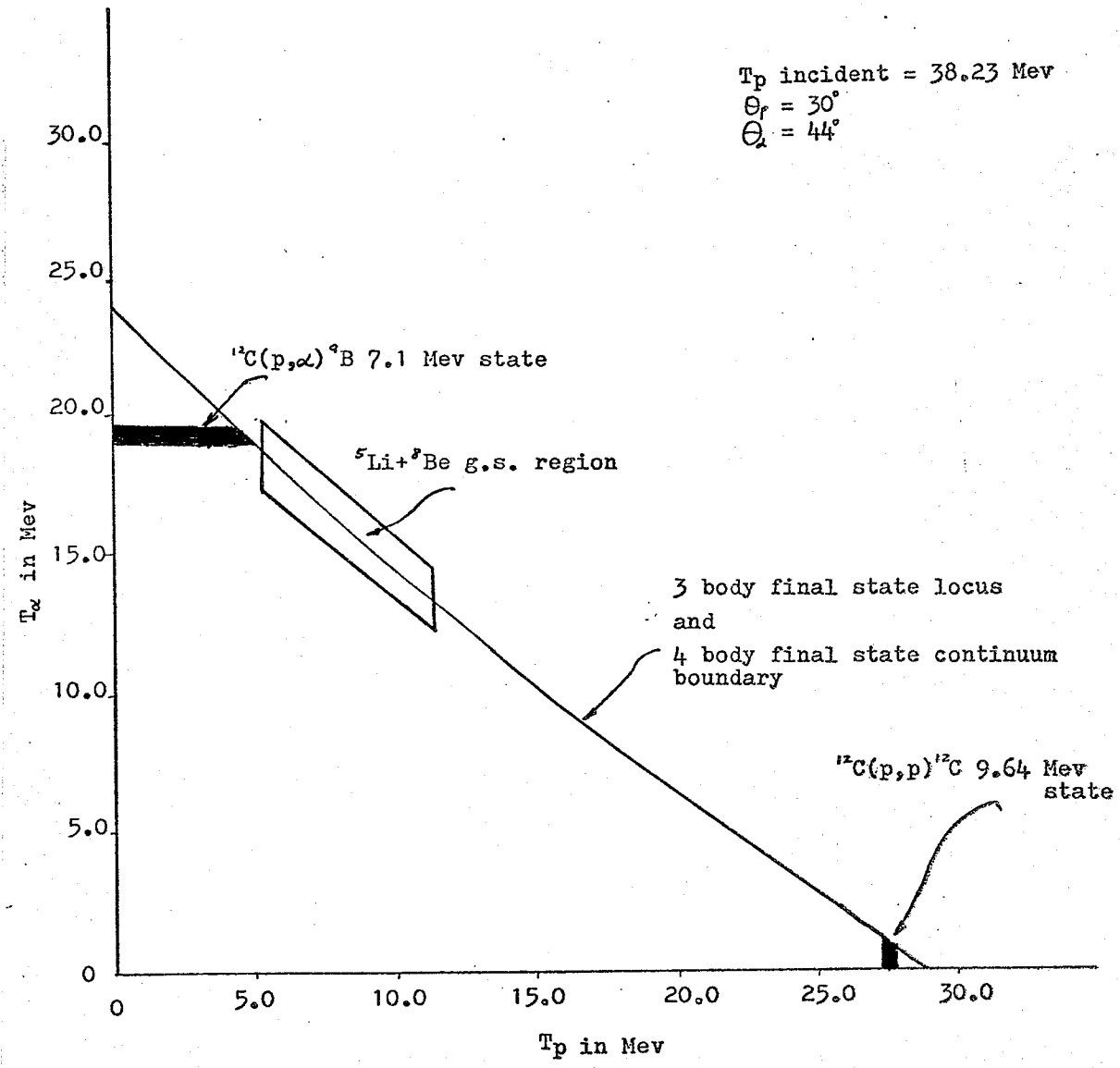
T_p incident = 38.23 Mev
θ_p = 30°
θ_α = 44°
$^{12}C(p,\alpha)^{9}B$ 7.1 Mev state
$^{5}Li+^{8}Be$ g.s. region
3 body final state locus
and
4 body final state continuum
boundary
$^{12}C(p,p)^{12}C$ 9.64 Mev
state
30.0
25.0
20.0
15.0
10.0
5.0
0
0
5.0
10.0
15.0
20.0
25.0
30.0
T_α in Mev
T_p in Mev

The analysis was carried out in three steps. The first step was to plot the data on a T_α vs T_p plot. The second step was to project the data onto the line with $T_\alpha = T_p$. If the events were mainly due to the reaction proceeding through ^{5}Li, then a peak should be observed in the neighbourhood of $T_\alpha + T_p = T_{^5Li} + Q$. The third step was to project the data onto the T_α and T_p axes. In these plots the effects due to sequential decays are emphasized.

V.4 The T_α vs T_p Plot

According to two body kinematics, if ^{5}Li breaks up into a proton and an alpha particle after the two body reaction $^{12}C(p,^5Li)^8Be$, then the sum of the proton and alpha particle energies falls on a straight line in the T_α vs T_p plot. This two body state corresponds to a resonance in the four body final state. The resonance should appear as a broad enhancement along the above mentioned straight line in the T_α vs T_p plot. Unfortunately results from the three body $^{12}C(p,p\alpha)^8Be$ reaction also fall very close to this line. There is however a difference in the shapes of the two body and three body distributions, which in principle at least permit the two and the three body reactions to be distinquished. This will be discussed in section V.5.b.

An attempt was made to observe directly such an enhancement on a scatter plot. The data plotted corres-

ponded to real events that had passed the test of particle identification. The scatter plots for all 3 proton detector angles (30°,40°, and 50°) are shown in Fig.5.4. The four body kinematic continuum boundaries from the calculations of equation (2.3) also are shown. These boundaries fall along the edge of the dense area in all the figures. Unfortunately the four body background is very strong and obscures any enhancement due to the two body $^{5}Li+^{8}Be$ final state.

V.5 Projections of Data onto Various Axes

The projections of data onto various axes are equivalent to summing the numbers of events associated with a certain variable. The data were projected onto the $(T_\alpha+T_p)$ axis, the T_α axis, and the T_p axis. The events, which did not pass the real coincidence test or the alpha particle locus test were excluded from the projections. The remaining events were true (p,α) coincidences due to ^{5}Li breakup plus the four body breakup of $^{12}C+p$, three body $(p,p\alpha)$ reaction on ^{12}C, and false coincidences. The proton and alpha particle energies from the group (2) reactions are shown in Table 5.1. The energies of protons from elastic or inelastic scattering to lowlying states of ^{12}C are higher than the energies of the coincident protons accepted in this experiment, thus eliminating an important source of random coincidences.

Fig.5.4

Scatter plots of T_α vs T_p. The four body continuum boundary and the three body final state locus are shown in the graphs. Since the Q-value of ^{8}Be breakup is 90 KeV, the three body locus is very close to the four body continuum boundary. Fig.5.4a.b.c show the scatter plots for $\theta_p = 30°$, $40°$, and $50°$ respectively. The events in these plots are real (random coincidence subtracted) and are within the alpha particle loci.

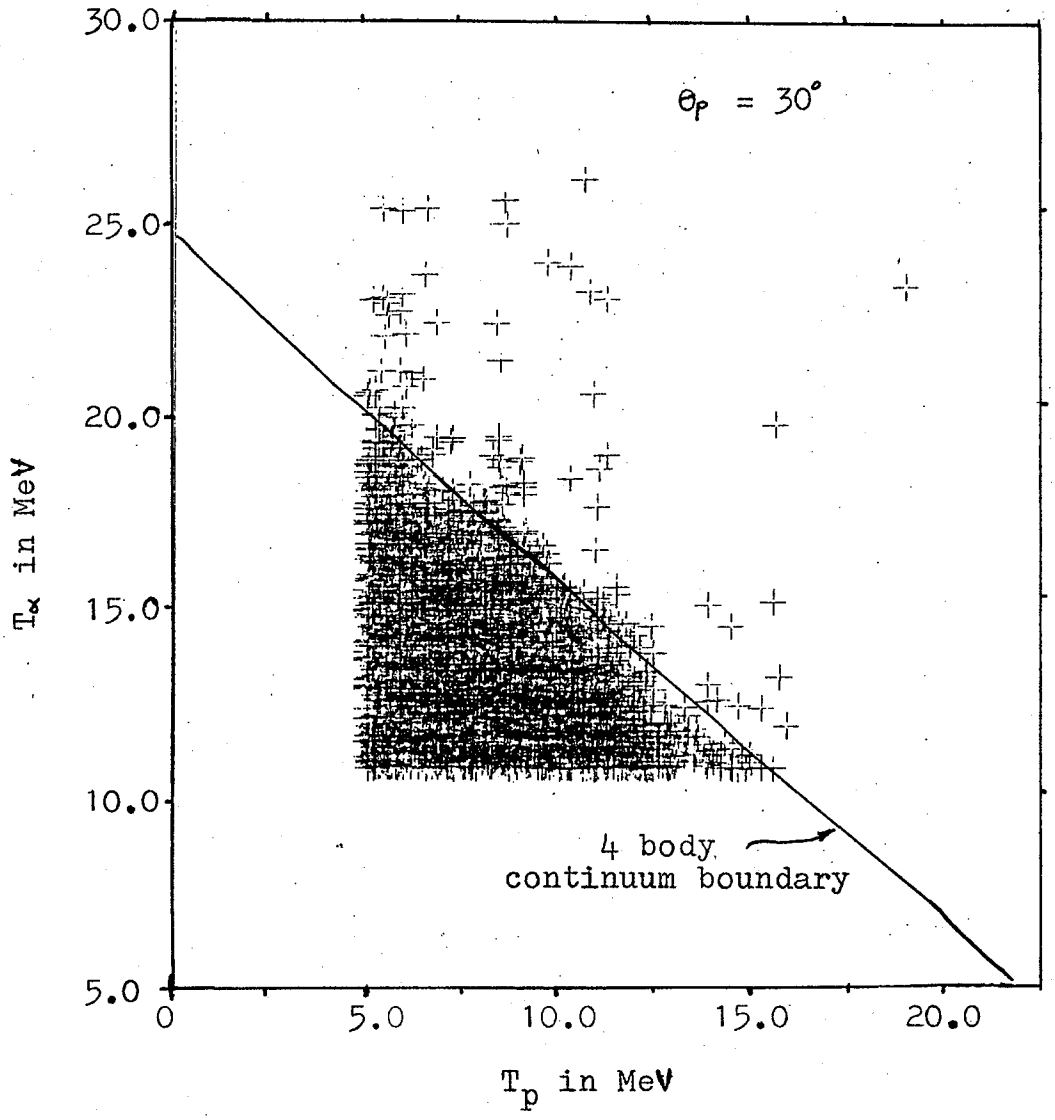
30.0
25.0
20.0
15.0
10.0
5.0
0
5.0
10.0
15.0
20.0
θ_p = 30°
4 body
continuum boundary
T_α in MeV
T_p in MeV

Fig.5.4a

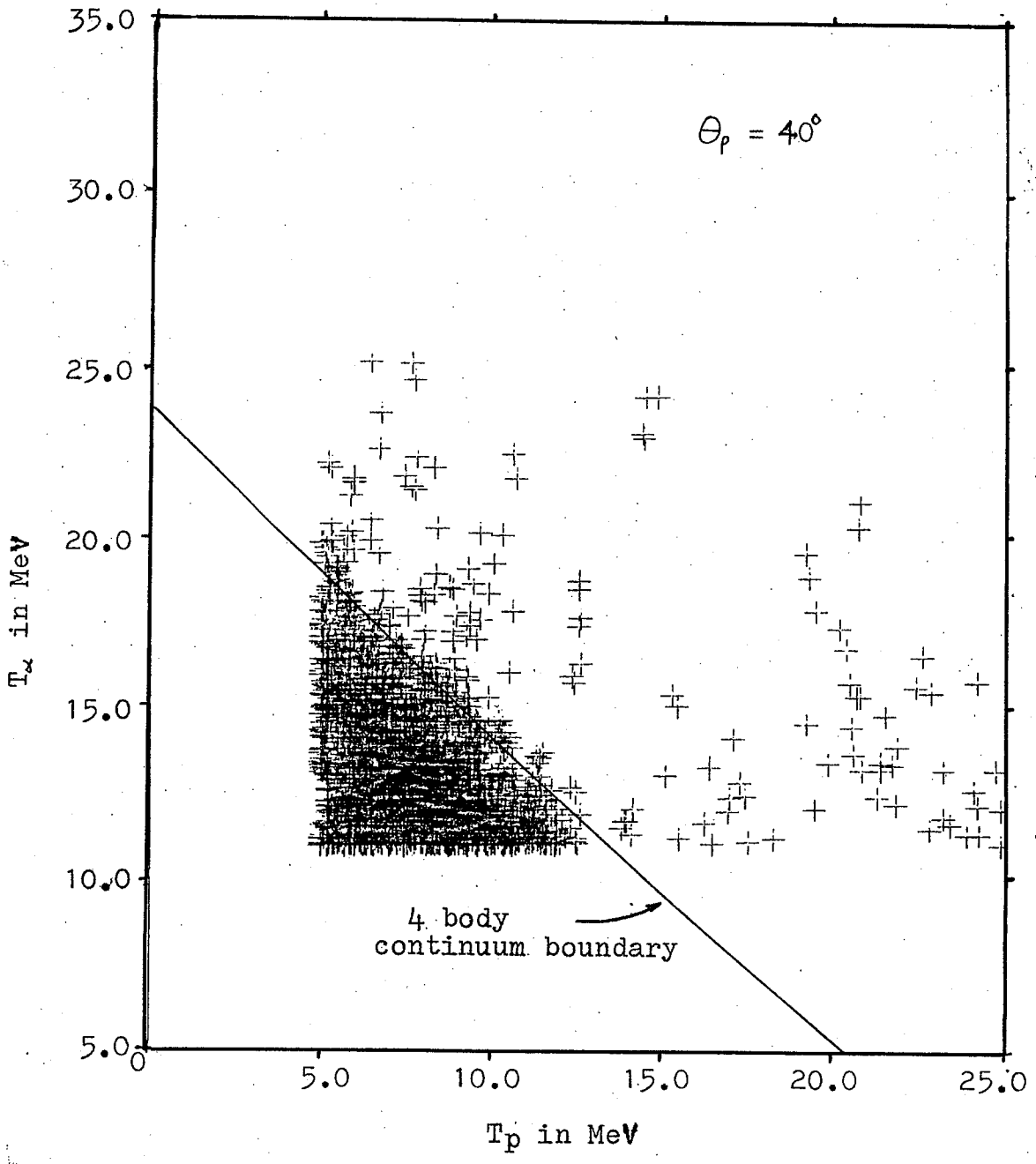
35.0
30.0
25.0
20.0
15.0
10.0
5.0
0
5.0
10.0
15.0
20.0
25.0
θ_p = 40°
4 body
continuum boundary
T_α in MeV
T_p in MeV

Fig.5.4b

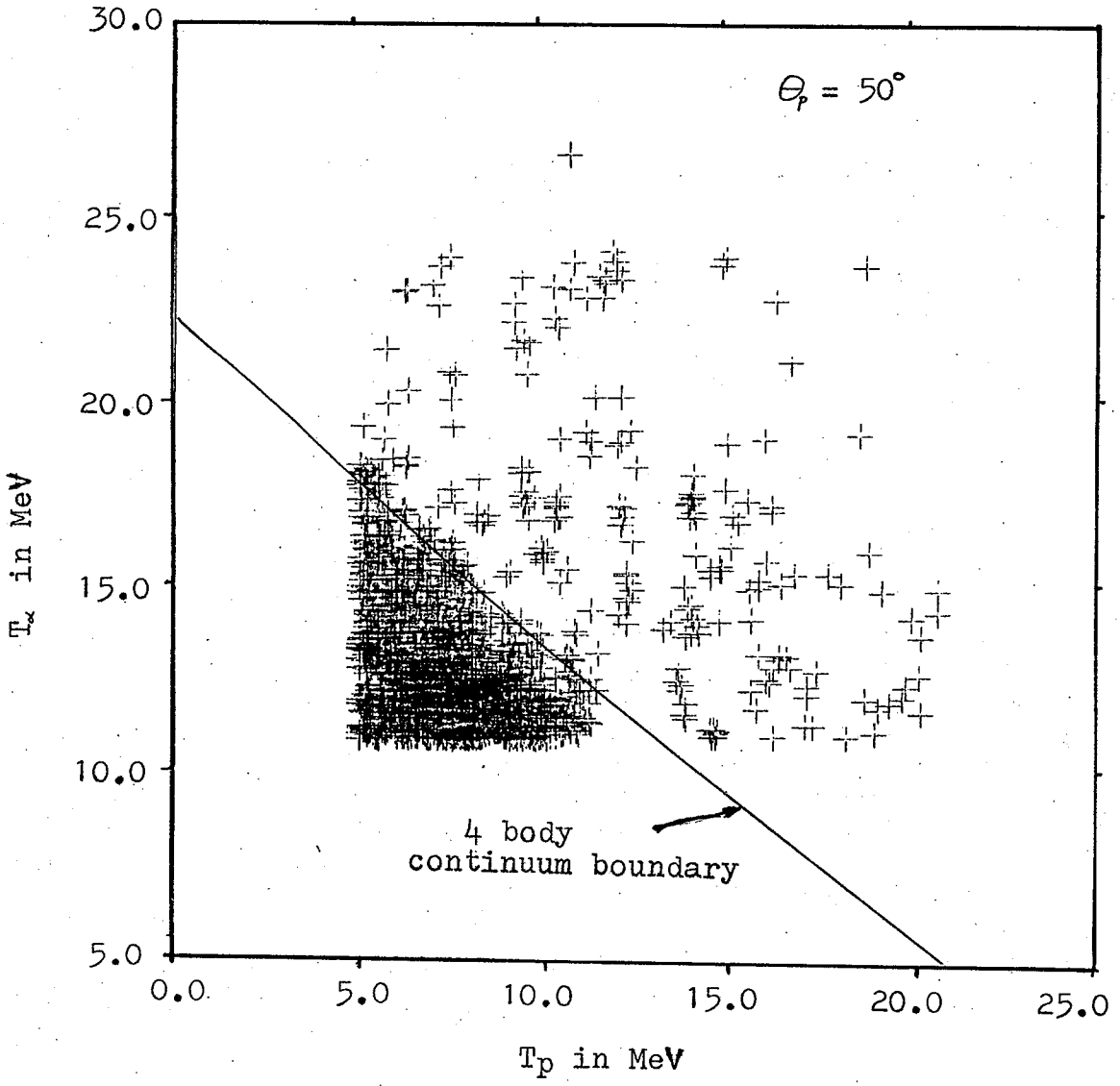
30.0
25.0
20.0
15.0
10.0
5.0
0.0
5.0
10.0
15.0
20.0
25.0
E_α in MeV
T_p in MeV
$\theta_p = 50°$
4 body
continuum boundary

Fig.5.4c

Table 5.1

The energies of different sequential decay reactions of group (2).

Reaction	Excited State in MeV	Proton energy in MeV θ_p =			α energy in MeV θ_p =		
		30°	40°	50°	30°	40°	50°
$^{12}C(p,\alpha)^{9}B$	1.5				24.0	23.1	22.1
	2.3				23.3	22.4	21.3
	7.1				19.4	18.6	17.6
$^{12}C(p,p)^{12}C$	4.4	33.0	32.4	31.6			
	7.7	29.7	29.2	28.5			
	9.6	27.8	27.2	26.5			

Only inelastic excitation of ^{12}C states above 24 MeV can contribute to sequential processes in the energy range in which $(p,^{5}Li)$ events should appear. However such states due to their high excitation are likely to be broad, and strongly overlapping, leading to a broad background in contrast to the narrow peaks of lowlying states.

V.5.a The Projection of Data onto the $T_\alpha+T_p$ Axis

The projection of data onto the $T_\alpha+T_p$ axis involves adding the numerical values of the kinetic energies of the coincident proton and alpha particle. If the proton and alpha particle were due to a $^{12}C(p,^{5}Li)^{8}Be$ two body reaction, then $T_\alpha+T_p$ should be a constant except for the ^{5}Li mass uncertainty. Therefore, a two body reaction should appear as an enhancement on the $T_\alpha+T_p$ axis in the vicinity of $T_\alpha+T_p=T_{Li}+Q$ where T_{Li} is obtained from a two body kinematic calculation. On the other hand if the proton and alpha particle in coincidence were due to a three body final state from $^{12}C(p,p\alpha)^{8}Be$, the events should correspond to a continuous locus on the T_α vs T_p plot. The ranges of $T_\alpha+T_p$ for the two body and the three body final states are shown in Table 5.2. It can be seen that the range of $T_\alpha+T_p$ for the three body final state overlaps the region corresponding to the two body reaction. Finally if the proton and the alpha particle in coincidence were due to the four body final state

Table 5.2

The comparision of the $T_\alpha+T_p$ value expected for a coincident proton and a alpha particle breakup, and the range of $T_\alpha+T_p$ for a three body final state from $^{12}C(p,p\alpha)^{8}Be$.

θ_p	θ_α	θ_{ξ_i}	$T_\alpha+T_p$ in MeV	Range of 3 body in MeV
30°	44°	39°	24.7±.2	24.5-26.1
40°	51°	46°	23.6±.2	23.4-24.8
50°	58°	54°	22.3±.2	22.1-23.3

reaction $^{12}C(p,p\alpha)\alpha\alpha$, the two undetected alpha particles would allow numerous possible combinations of T_α and T_p. However, phase space considerations suggest that the four body contribution should fall rapidly near the four body boundary making it possible to observe two body enhancements.

The spectra for $T_\alpha+T_p$ for all three proton detector angles are shown in Fig.5.5. It is observed that a small (and ambiguous) enhancement appears in each case near the expected values for a $^5Li+^8Be$ final state. There remains the problem of separating the two body and the three body events as they both appear within the small "peaks".

V.5.b The projection of Data onto the T_α and T_p Axes

It is also of interest to project data onto the T_α and T_p axes. The purpose of such projections is to distinguish two body and the three body effects. According to three body phase space calculations the projection of data onto either the T_α or the T_p axis should result in a very wide distribution as shown in Fig.5.6. If a small portion of the four body final state continuum were also included, the projection of the data would still result in a broad shape of similar nearly featureless character. In the present experiment since the ^8Be breakup Q value is only 95 KeV, the boundary of the four body continuum should be nearly superimposed on the three

Fig.5.5

The single histogram plots against $T_\alpha + T_p$. Fig.5.5a, b, c correspond to the plots of θ_p = 30°, 40°, and 50° respectively.

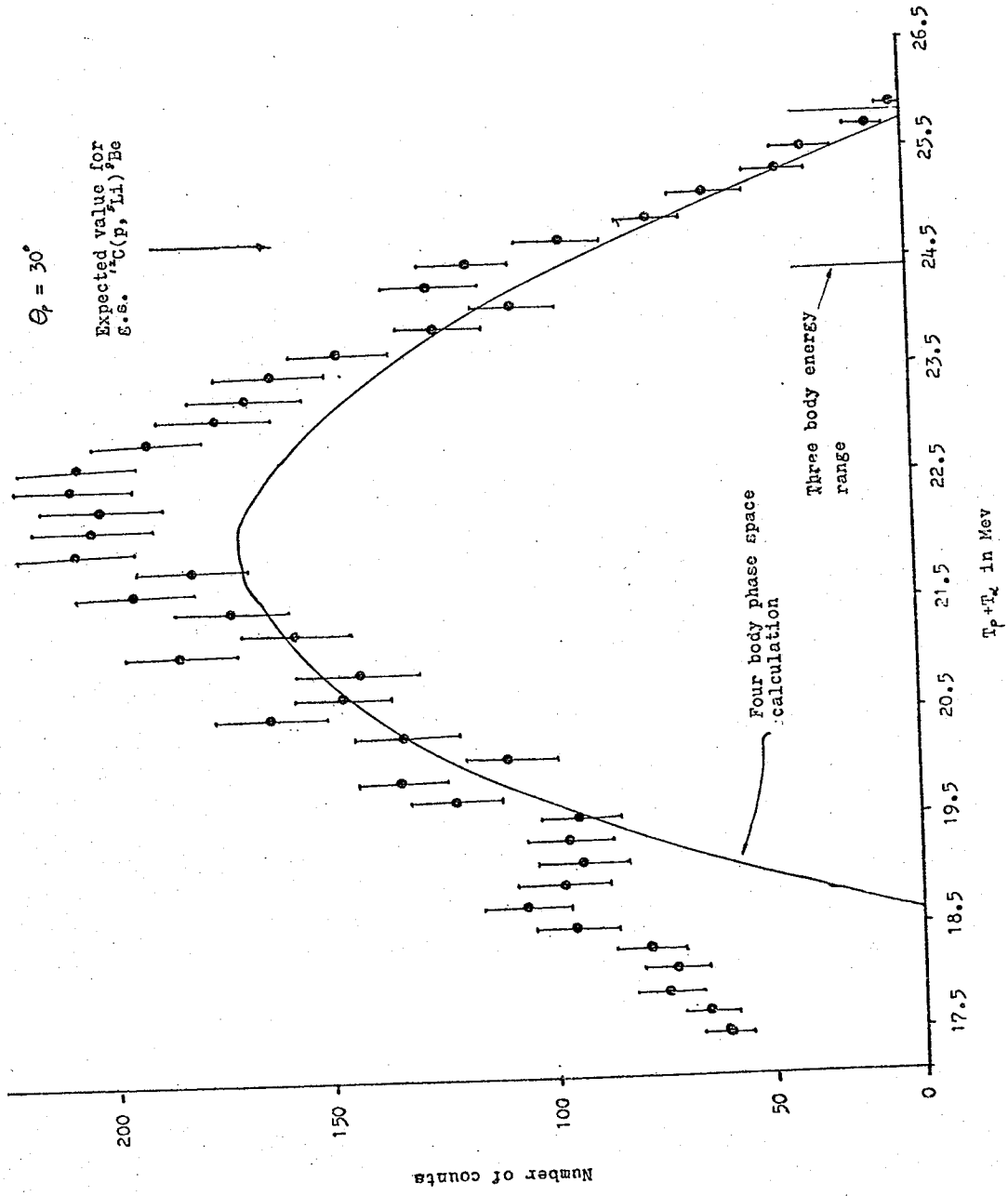
θ_p = 30°
Expected value for g.s. $^{12}C(p, {}^{7}Li)^{6}Be$
Three body energy range
Four body phase space calculation
$T_p + T_4$ in Mev
Number of counts
0
50
100
150
200
17.5
18.5
19.5
20.5
21.5
22.5
23.5
24.5
25.5
26.5

Fig.5.5a

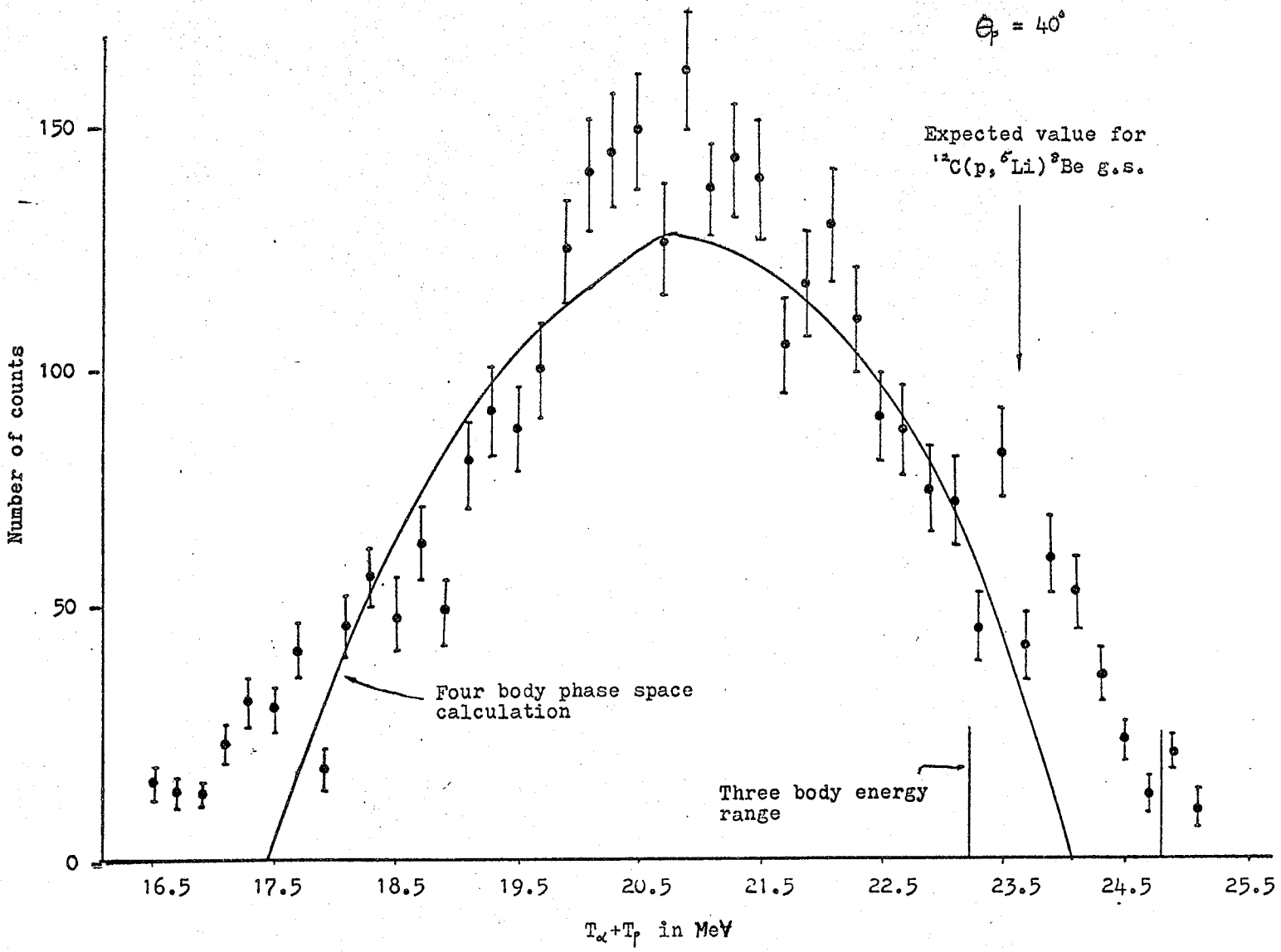
θ_p = 40°
Expected value for
$^{12}C(p,{}^6Li)^8Be$ g.s.
Four body phase space calculation
Three body energy range
Number of counts
150
100
50
0
16.5
17.5
18.5
19.5
20.5
21.5
22.5
23.5
24.5
25.5
$T_\alpha+T_p$ in MeV

Fig.5.5b

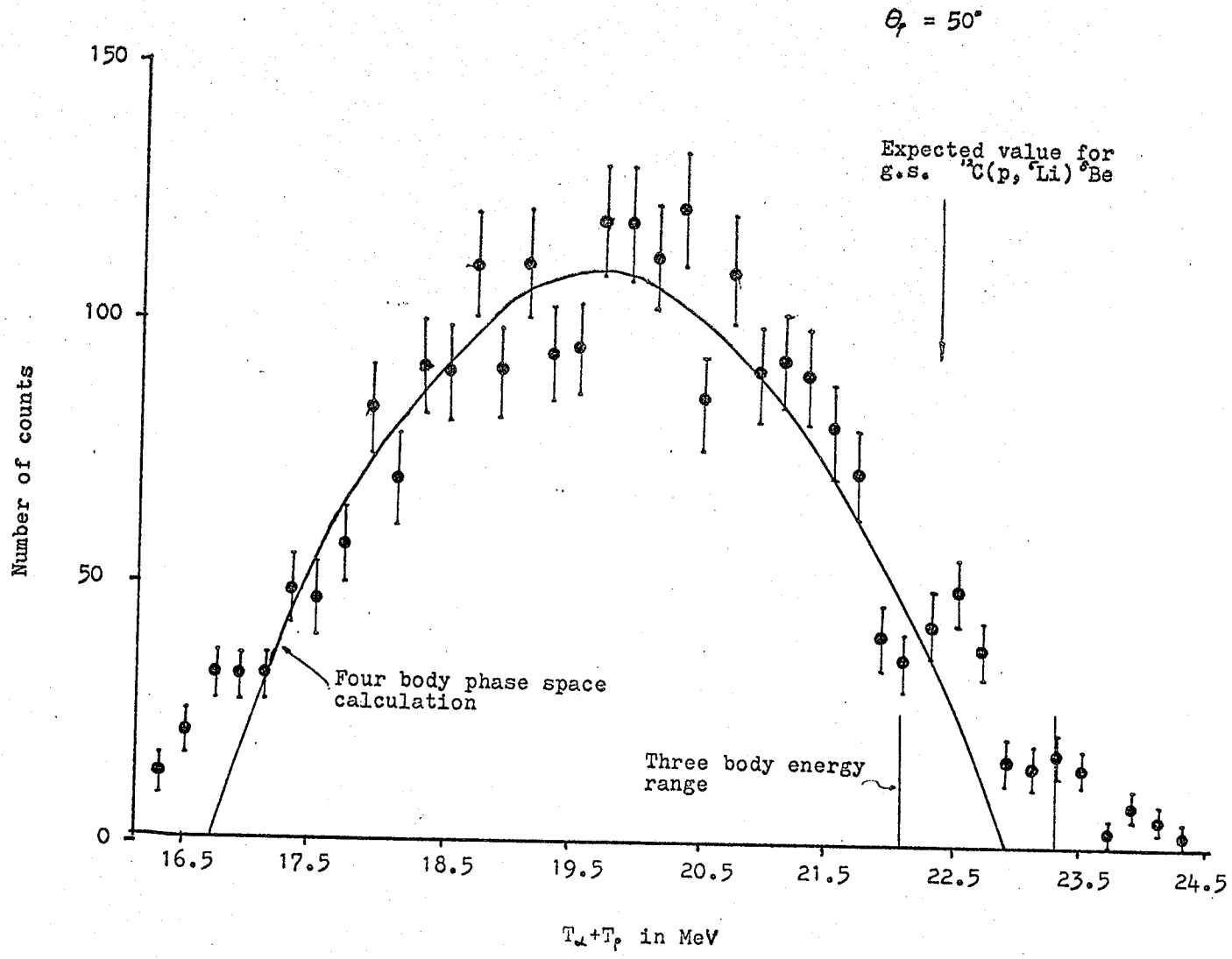
θ_l = 50°
Expected value for g.s. $^{12}C(p, {}^6Li)\,{}^8Be$
Four body phase space calculation
Three body energy range
Number of counts
150
100
50
0
16.5
17.5
18.5
19.5
20.5
21.5
22.5
23.5
24.5
$T_\alpha + T_p$ in MeV

Fig.5.5c

Fig.5.6a

The distribution of events on the T_p axis due to two body $^{12}C(p,^{5}Li)^{8}Be$, three body $^{12}C(p,p\alpha)^{8}Be$, and four body $^{12}C(p,p\alpha)\alpha\alpha$. The two body distribution on the T_p axis is from the Monte Carlo calculation and is shown at the bottom of the histogram. The three body and the four body phase space distributions have similar shapes and follow the curve marked " 3 body and 4 body phase space calculation".

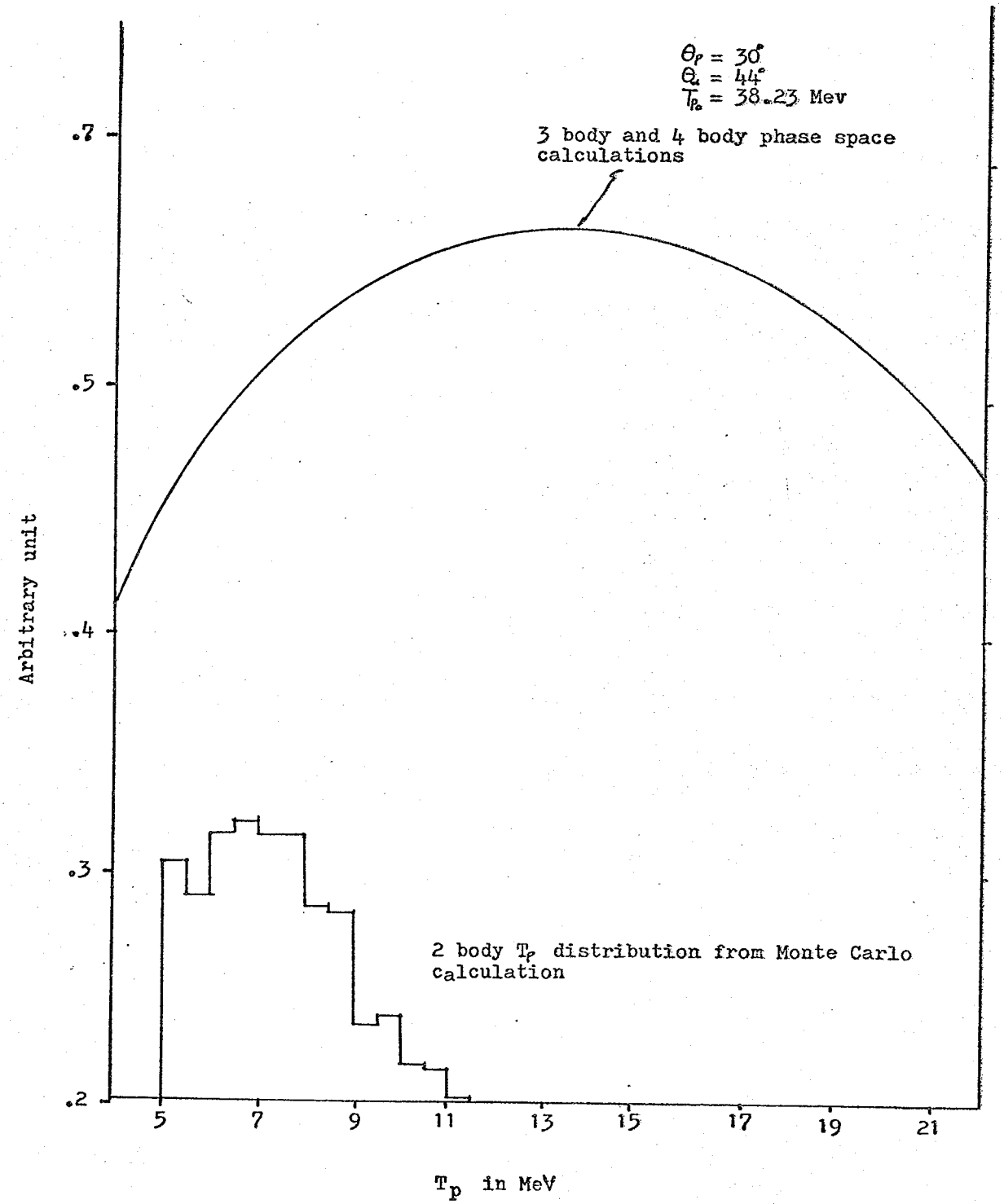
θ_p = 30°
θ_α = 44°
T_{p_0} = 38.23 Mev
3 body and 4 body phase space calculations
2 body T_p distribution from Monte Carlo calculation
Arbitrary unit
.7
.5
.4
.3
.2
5
7
9
11
13
15
17
19
21
T_p in MeV

Fig.5.6b

The theoretical two body, three body, and four body final state distribution on the T_α axis. The two body final state distribution is from the Monte Carlo calculation. The distributions of the three body and the four body final state are from the phase space calculation and have similar shapes.

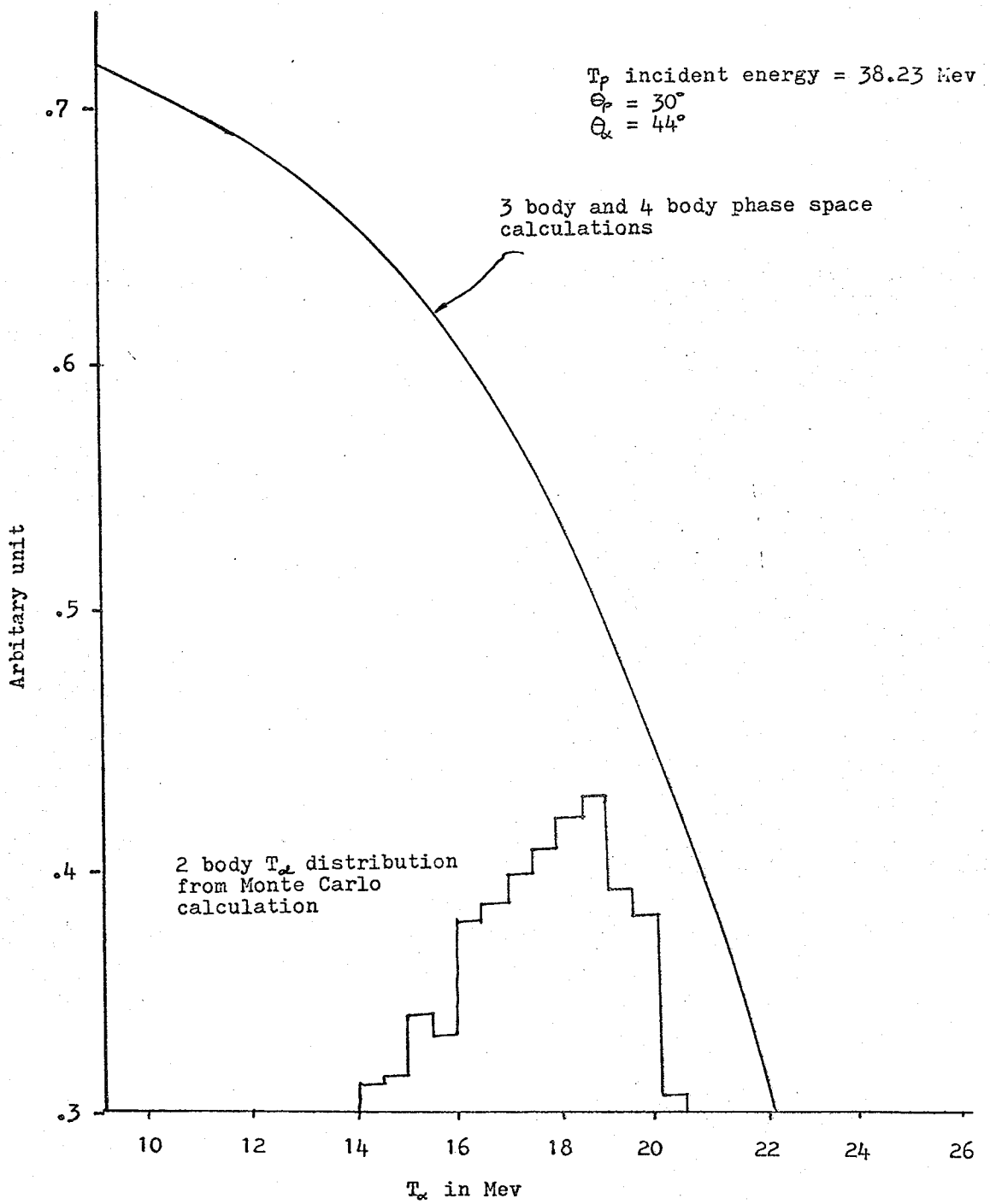
T_p incident energy = 38.23 Mev
θ_p = 30°
θ_α = 44°
3 body and 4 body phase space calculations
2 body T_α distribution from Monte Carlo calculation
Arbitary unit
.7
.6
.5
.4
.3
10
12
14
16
18
20
22
24
26
T_α in Mev

body locus. The shapes of projections of events from two, three, and the four body final state reactions onto the T_α and the T_p axes are shown in Fig.5.6. The two body shape was obtained from the Monte Carlo calculation. From this plot it is seen that events due to three body and the four body final states can possibly be resolved from the two body reaction. As mentioned above if the background is mainly due to the three body and the four body final states, the projection of data onto the T_α or T_p axis should appear as a broad distribution. However, if the reaction is due to the two body final state, the data should appear as an enhancement over the region given by the Monte Carlo calculation.

The projections of experimental data onto the T_α and the T_p axis are shown in Fig.5.7. In Figs.5.7b and 5.7c only data within a narrow range of $T_\alpha+T_p$ were plotted, the range was wide enough to include all (p,^{5}Li) and three body events populating ^{8}Be in its ground state but narrow enough to exclude most of the four body events. The range is delimited by two straight lines cutting across the T_α vs T_p plot as shown in Fig.5.8 for $\theta_p=30^o$. If the data projected onto the T_p axis are due mainly to reactions other than sequential decays, the experimental curve should be in the form of a broad peak on top of a wider distribution. Unfortunately the poor statistics obtained do not permit resolution of the two body

Fig.5.7a

The projections of the data onto the T_α and T_p axis without setting constraints which limit the events to be within the small enhancement as shown in Fig.5.5.

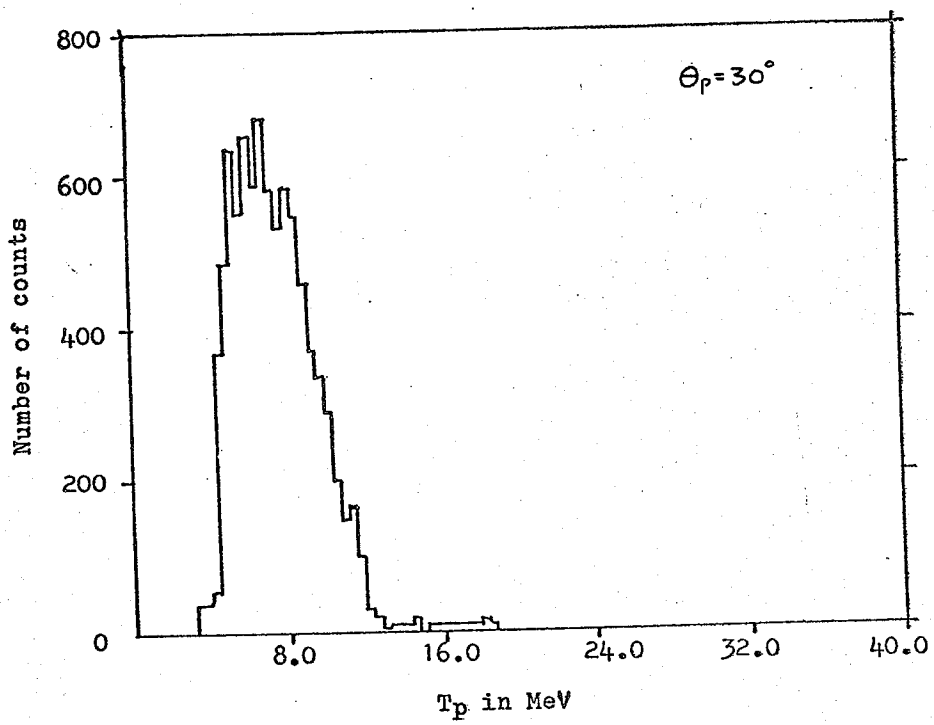
800
600
400
200
0
Number of counts
$\theta_p = 30°$
8.0
16.0
24.0
32.0
40.0
Tp in MeV

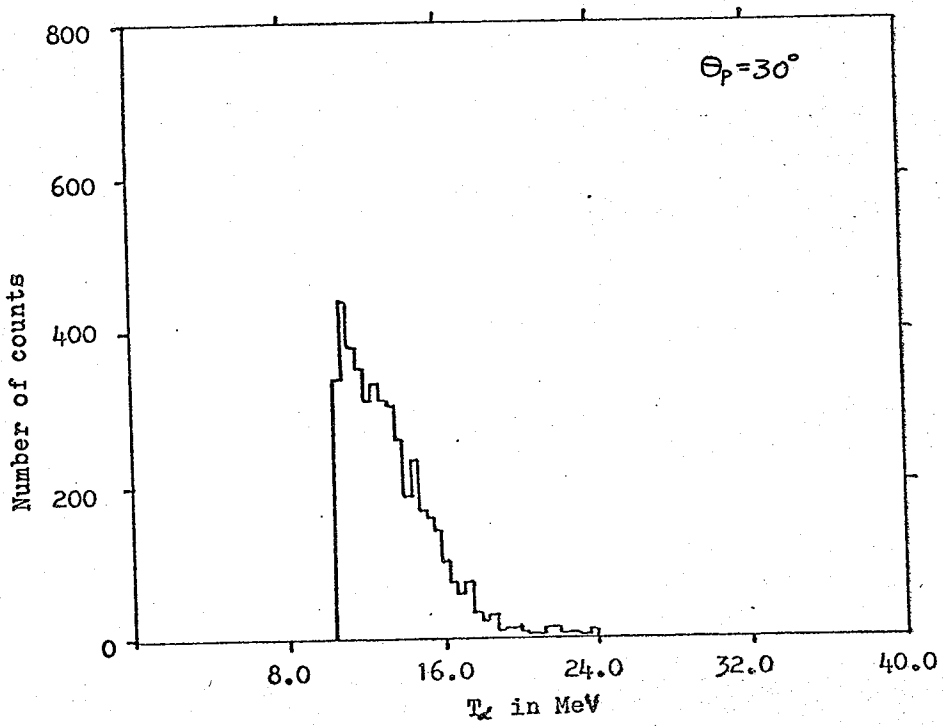
800
600
400
200
0
Number of counts
$\theta_p = 30°$
8.0
16.0
24.0
32.0
40.0
T_α in MeV

Fig.5.7b

The projections of experimental data within the small enhancement shown in Fig.5.5 onto the T_p axis. The dotted line is the shape of the two body distribution from the Monte Carlo calculation.

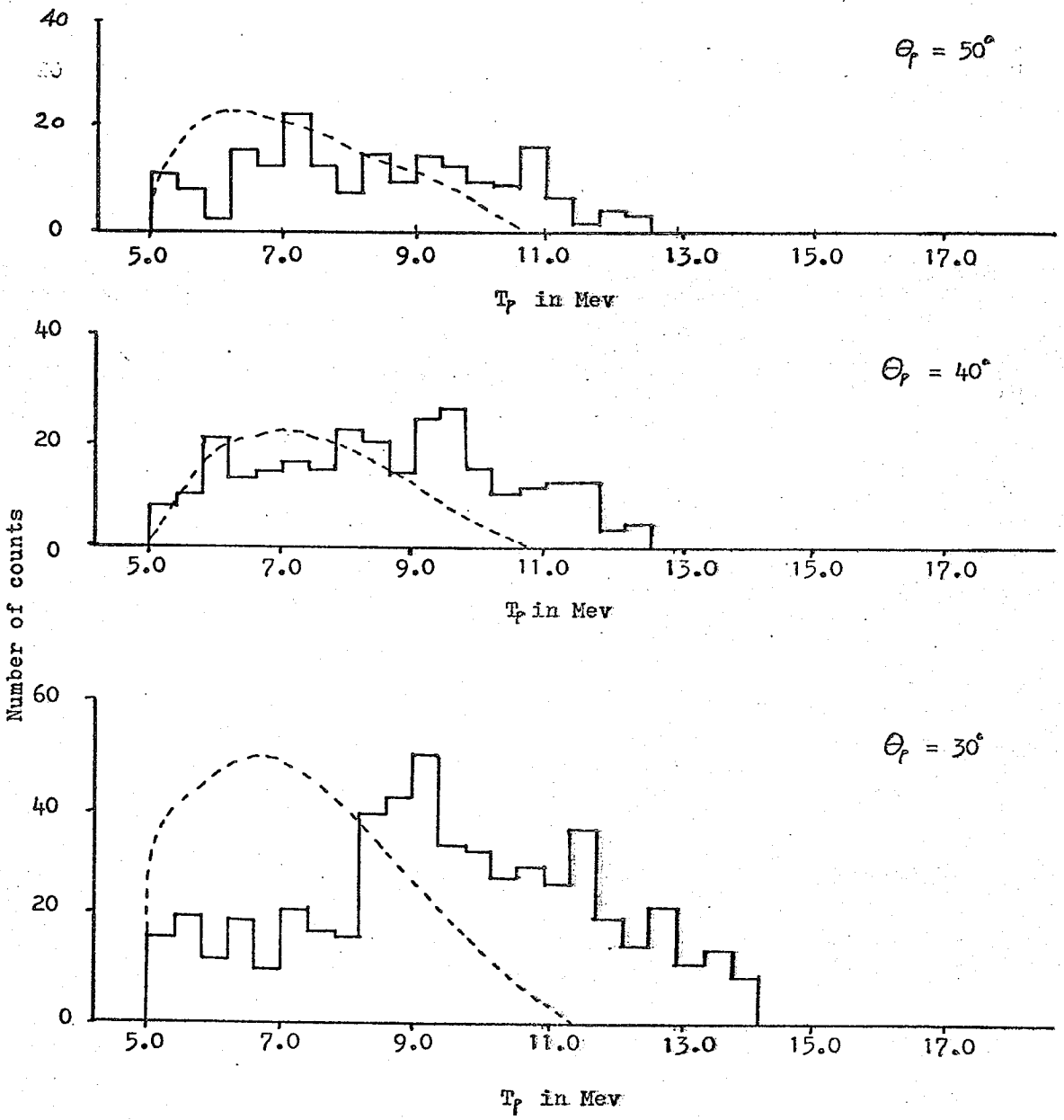
40
20
0
θ_p = 50°
5.0
7.0
9.0
11.0
13.0
15.0
17.0
T_p in Mev
40
20
0
θ_p = 40°
5.0
7.0
9.0
11.0
13.0
15.0
17.0
T_p in Mev
Number of counts
60
40
20
0
θ_p = 30°
5.0
7.0
9.0
11.0
13.0
15.0
17.0
T_p in Mev

Fig.5.7c

The projection of experimental data within the small enhancement shown in Fig.5.5 onto the T_α axis. The dotted line is the two body distribution shape obtained from the Monte Carlo calculation.

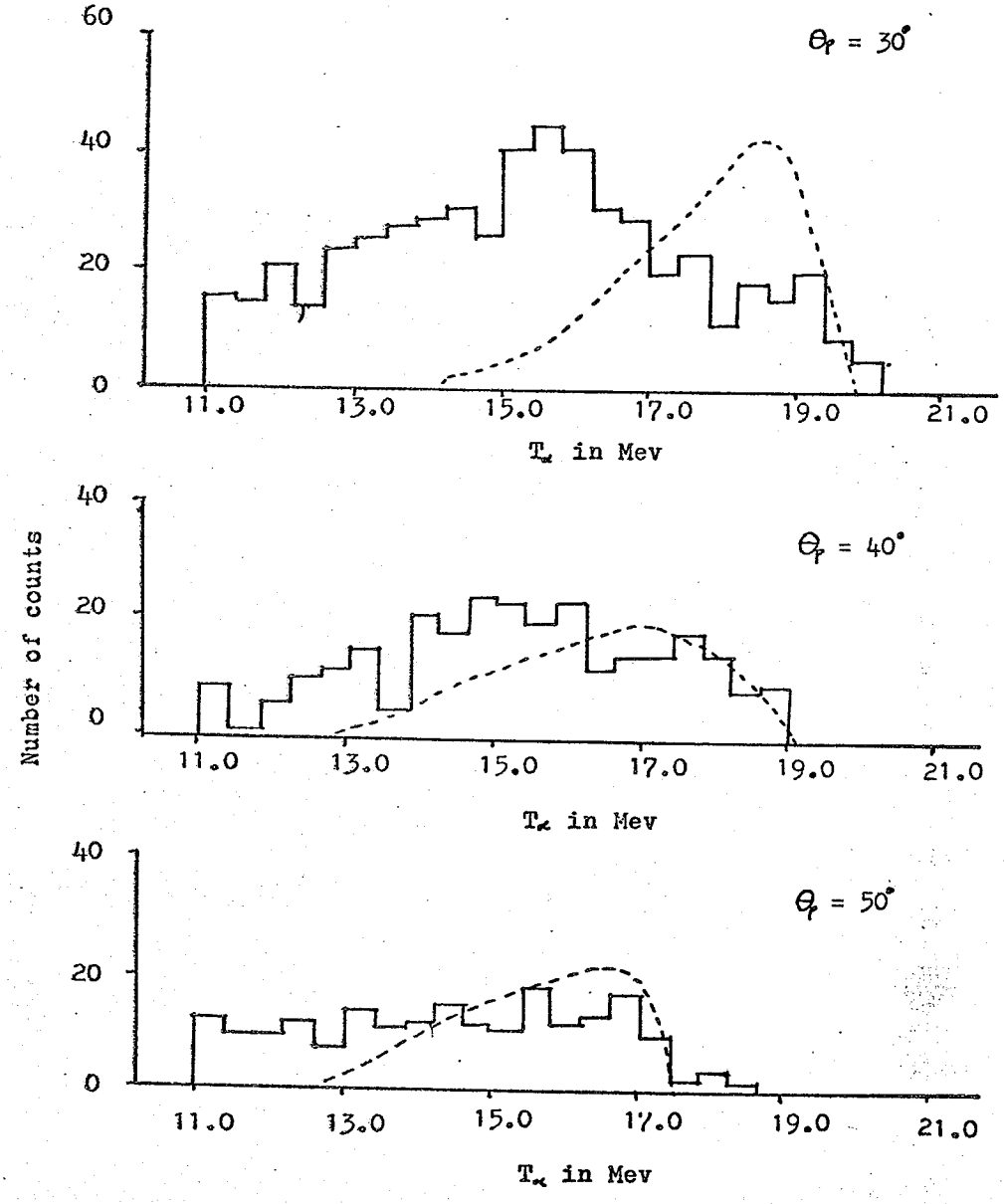
60
40
20
0
θ_p = 30°
11.0
13.0
15.0
17.0
19.0
21.0
T_α in Mev
40
20
0
θ_p = 40°
Number of counts
11.0
13.0
15.0
17.0
19.0
21.0
T_α in Mev
40
20
0
θ_p = 50°
11.0
13.0
15.0
17.0
19.0
21.0
T_α in Mev

Fig.5.8

The limits on $T_\alpha + T_p$ used in the projections of data onto the T_α and T_p axes. The limits were calculated to include $^{12}C(p,^5Li)^8Be$ events leading to ground state of ^8Be. The small enhancements noted on the high energy flanks of the distributions in Fig.5.5 are within these limits.

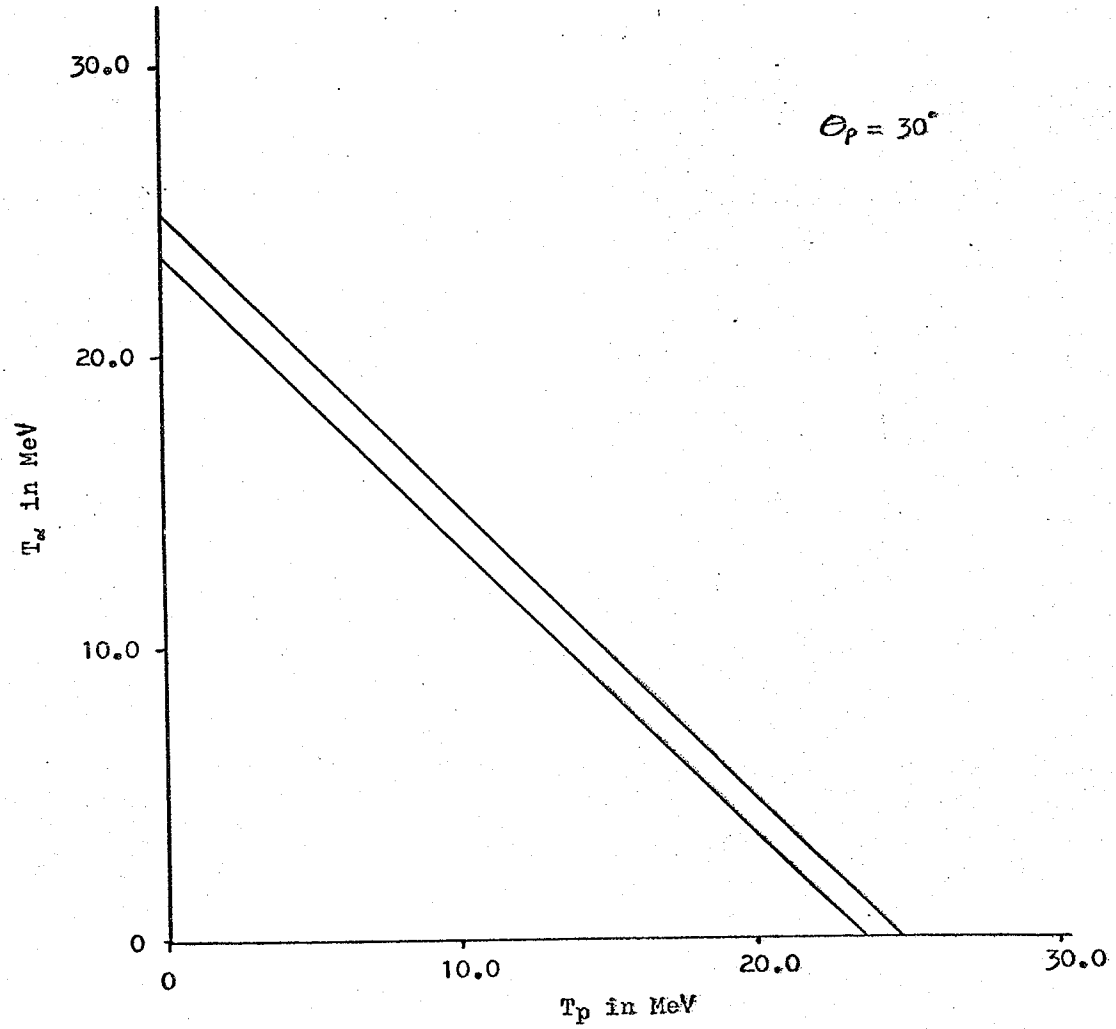
30.0
20.0
10.0
0
T_α in MeV
$\theta_p = 30^\circ$
0
10.0
20.0
30.0
T_p in MeV

reaction from the three and the four body final state reactions so that at best an upper limit for the cross section of (p,^{5}Li) reaction is obtainable. Figs.5.7b and 5.7c also show that the expected shapes of the two body final state do not match the experimental shape. This suggests that the differential cross section of the two body final state reaction is small.

V.6 The Upper Limits on the Cross Section

Since the data of the present experiment could not give definite proof of the presence of the $^{12}C(p,^{5}Li)^{8}Be$ reaction, only an upper limit on the cross section can be calculated. Any (p,^{5}Li) events present would be in the small peaks in Fig.5.5 along with three body and sequential events. The four body background may be roughly subtracted assuming its shape is known from the phase space calculations. The resulting spectra are plotted in Fig.5.9. The number of counts in each peak is of the order of 100. The uncertainties in the numbers of counts are large however due to uncertainty in subtraction of the four body background. Error bars are not shown since the major source of error is common to all points and is of the order of 100%. See Section V.7.

The experimental cross section for $^{12}C(p,^{5}Li)^{8}Be$ can be calculated using the formula:

$$\frac{d\sigma}{d\Omega} = \frac{Y}{NI\varepsilon_0}$$

Fig.5.9

The spectra obtained by subtracting the four body phase space curve from the spectra in Fig.5.5.

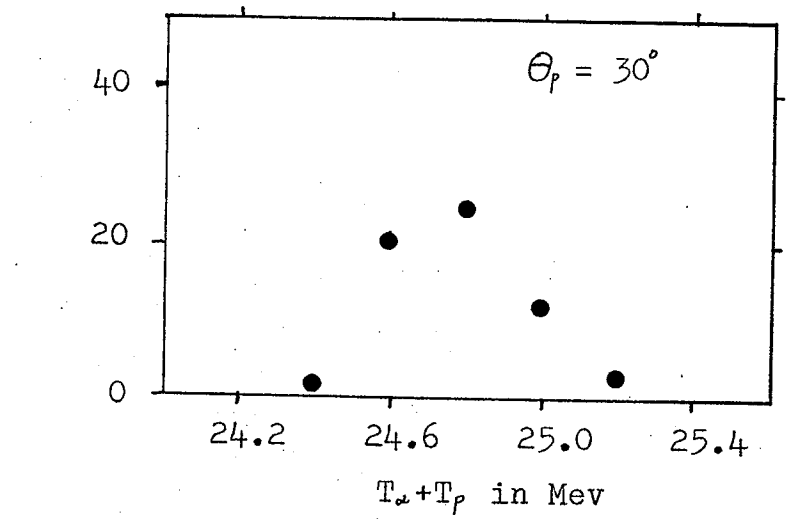
θ_p = 30°
40
20
0
24.2
24.6
25.0
25.4
$T_\alpha + T_p$ in Mev

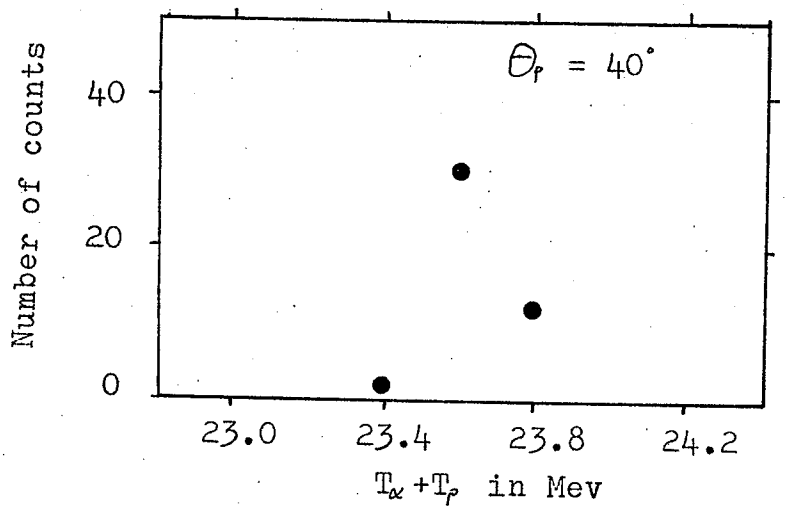
Number of counts
θ_p = 40°
40
20
0
23.0
23.4
23.8
24.2
$T_\alpha + T_p$ in Mev

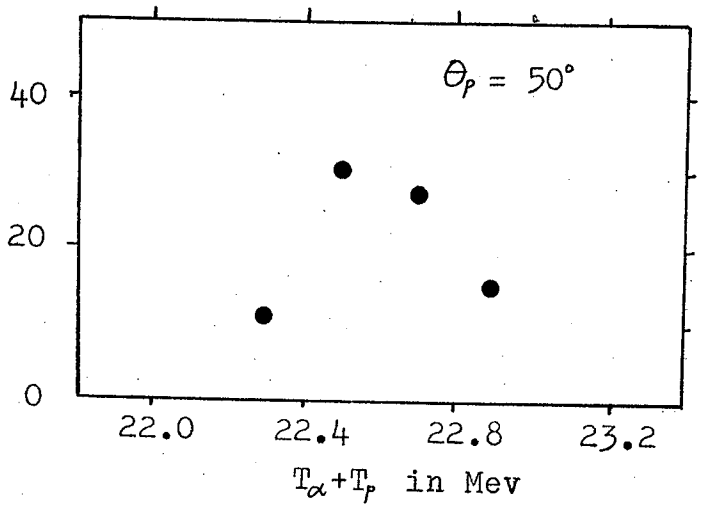
θ_p = 50°
40
20
0
22.0
22.4
22.8
23.2
$T_\alpha + T_p$ in Mev

where Y represents the number of counts in the peak as shown in Fig.5.9, in which all the events are assumed to be (p,^{5}Li) events.

ε_0 is the efficiency for detecting ^{5}Li as obtained from the Monte Carlo calculation,

N is the number of the target nuclei per unit area,

I is the total number of protons incident on the target.

The data for calculating the cross section along with the results are shown in Table 5.3.

V.7 Error

In this section the relative and absolute error in the cross section associated with this experiment will be discussed. The relative error is due mainly to the statistical uncertainties in the peak being considered, and contains in all cases contributions from both the 'real+random' and 'random' coincidence spectra. The error bars shown in Fig.5.5 represent these uncertainties. It can be seen that the uncertainty in the peaks is about 10%. However, in those peaks obtained by subtracting the four body phase space background, the error can be as high as 100%. This value is obtained by moving the four body curve within the statistical error bars on points where the four body background is expected to dominate. The other source of relative error is the dead time correction which was obtained by comparing the

Table 5.3

The data and results of the calculated cross section. The definitions of various symbols are explained in the text.

θ_p	θ_α	θ_{x_1}	ε_D	N	I	Y	$\frac{d\sigma}{d\Omega}$
			x10^{-5}	x10^{20}	x10^{15}		μb/SR
			in SR	n cm^2	counts		
30°	44°	39°	1.18	1.49	4.14	61	≤8.4
30°	51°	46°	1.16	1.49	3.26	45	≤7.9
50°	58°	54°	1.14	1.37	4.94	83	≤10.7

number of Faraday cup counts recorded by the computer and the number recorded in a fast scaler. This correction varied from 0.01% at θ =40° to 2.5% for θ =30°.

The major sources of absolute errors in the cross sections are

(1) the determination of target thickness (about 5%).

(2) the determination of the efficiency of detecting ^{5}Li, (about 5%).

There are also other minor sources of error such as the pileup correction and the target angle. These errors are neglected however since their contribution to the total error is much smaller than that of other sources. The errors on the values of Y (i.e. the peaks in Fig.5.9), and thus on the cross sections, are about 100%.

VI. Discussion and Conclusion

VI.1 Discussion

The upper limits on the cross section for the $^{12}C(p,^{5}Li)^{8}Be$ reaction obtained in the present experiment are about $(10\pm10)\mu b/sr$, these may be compared with the cross sections for the analogous $^{12}C(d,^{6}Li)^{8}Be$ reaction. With an incident deuteron energy of 52 MeV, the cross section for the $^{12}C(d,^{6}Li)^{8}Be$ reaction has been found to be about $(4\pm1)\mu b/sr$ in the angular range 40°-60° (EIC70). The cross section of the $^{12}C(p,^{5}Li)^{8}Be$ reaction may well be smaller than that of $^{12}C(d,^{6}Li)^{8}Be$ because the ^{5}Li is less bound than the ^{6}Li, the $^{12}C(p,^{5}Li)^{8}Be$ reaction therefore tending to go through more direct breakup channels than the $^{12}C(d,^{6}Li)^{8}Be$.

There are several ways in which this experiment might be improved. It is suggested that a different target should be used. The target should be chosen on the basis that competing reactions producing alpha particles have smaller cross sections. This would provide a smaller background and fewer random coincidences than in the present case.

It is also suggested that this experiment should be run at a higher incident proton energy. As shown in Fig.6.1 the separation angles for the proton and the alpha particle from ^{5}Li and the two alpha particles from

Fig.6.1

The separation angles plotted as a function of the incident proton energies.

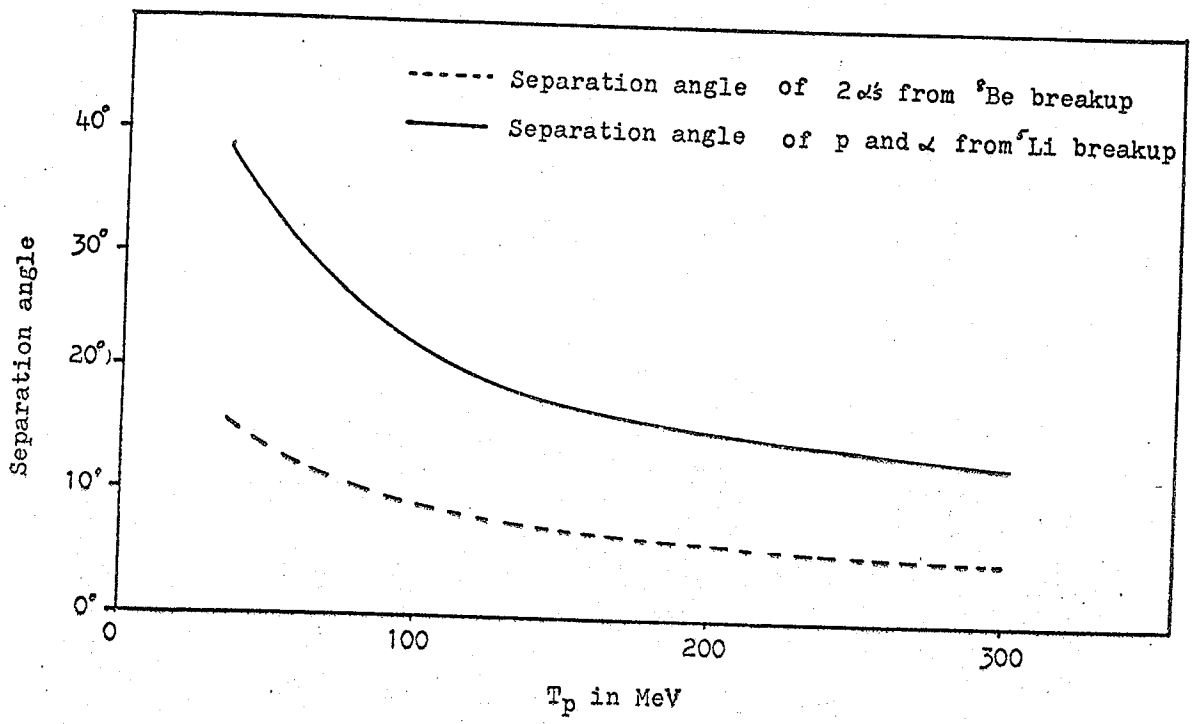
Separation angle of 2α's from ⁸Be breakup
Separation angle of p and α from ⁶Li breakup
Separation angle
40°
30°
20°
10°
0°
0
100
200
300
Tp in MeV

^{8}Be become smaller as the incident proton energy increases. As the separation angle between the proton and the alpha particle becomes smaller, it is possible to put two proton detectors one above and one below the plane as shown in Fig.3.5a. This would provide a larger solid angle for detecting the proton. The other advantage with higher incident proton energy is that the two alpha particles from the breakup of ^{8}Be might be detected. Since the separation angle between these two alpha particles is small, it would be possible to set up one detector telescope to detect the two alpha particles simultaneously. Since the two alpha particles are from the breakup of ^{8}Be, they would arrive at the ΔE detector almost simultaneously, and deposit twice the amount of energy as a single alpha particle in both the ΔE and E detectors. This would identify a ^{8}Be as opposed to an alpha particle. From two body kinematics, the ^{8}Be should have a fixed energy at a given angle. Therefore the sum of the energies of the two alpha particles from the ^{8}Be breakup should be constant except for effects due to the ^{5}Li mass uncertainty. The experiment might possibly, in fact, be run looking only for ^{8}Be nuclei, a (p,^{5}Li) reaction being indicated by an enhancement in the number of ^{8}Be nuclei at an energy corresponding to the emission of a single ^{5}Li particle. The detection of the proton and the alpha particle from the ^{5}Li (or at least the

alpha particle) would greatly reduce the background. Such an arrangement, would of course, introduce more technical difficulties in setting up the experiment.

VI.2 Conclusion

Although the present experiment shows no definite evidence of the $^{12}C(p,^{5}Li)^{8}Be$ reaction, it does not eliminate such a possibility. The difficulties associated with this experiment permit only an upper limit on the cross section to be obtained. The difficulties include the following in summary.

(1) It is anticipated that the reaction has a small cross section.

(2) The detection of the proton out of the scattering plane is not feasible in the present case. This limits the proton detector solid angle.

(3) It is also difficult to resolve the two body from the three body final state due to poor statistics and large three and four body background.

The upper limits on the cross section for the $^{12}C(p,^{5}Li)^{8}Be$ reaction populating ^{8}Be in its ground state are found in the present experiment to be approximately $(10\pm10)\mu b/sr$ in the angular range 30° to 50°.

References

ANK63 C.M.Ankenbrancdt and E.M.Lent, Rev.Sci.Instr. 34(63)647.

AUS70 N.Austern "Direct Nuclear Reaction Theories" (John Wiley & Sons 1970).

AVE63 L.N. Averina, B.I.Kerner, R.A.Nikulina, T.I. Sokolovskaya, and Yu.A.Tsirlin, Optics and Spectroscopy 15(1963)146.

BAK69 C.A.Baker, B.E.Bonner, I.M.Blair, F.P.Brady, J.A. Edgington, and V.J.Howard, Nucl. Instr. and Meth. 71(1969)117.

BAL64 V.V.Balashov, A.N.Boyarkina and I.Rotter Nucl. Physics 59(64)417.

Bal65 V.V.Balashov and I.Rotter Nucl. Physics 61(65)138.

BAU69 R.W.Bauer, G.Heymann, W.Kossler, N.S.Wall and C.R. Gruhn. Rev. Mod. Physics 37(65)369.

BEN65 R.S.Bender and E.Newman, Bull. Am. Physics Soc. 10(1965)602.

BER65 P.Beregi, N.S.Zelenskaja, V.N.Neudatchin, and Yu. F.Smirvo, Nucl. Phys. 66(1965)513.

BET67 K.Bethge, K.Meier-Evert, K.Pfeiffer and R.Bpck Phys. Lett. 24B(1967)663.

BIR51 J.B.Birks, Proc. Phys. Soc. A64(51)874.

BRA71 K.H.Bray, M.Jain, K.S.Jayaraman, G.LoBianco, W.T. H.Van Oers, and Y.I.Wu, Nucl. Phys. A163(1971)649.

BRO65 R.E.Brown, J.S.Blair, D.Bodansky. N.Cue and C.D. Kavaloski, Phys. Rev. 138(1965)B1394.

BUR66 J.J.Burgerjon, I.E.E.E. Trans. on Nucl. Science NS-13(1966)422.

COC67 M.Cocchi and A. Rota. Nucl. Instr. and Meth. 46(1967)136.

CRA66 R.M.CRaig,B.Hind, C.J.Dost and T.Y.Li Phys. Lett. 21(1966)177.

DAE64 W.W.Daehnick and L.J.Denes Phys. Rev. 136(1964)B1325.

DAE66 W.W.Daehnick and L.J.Denes, Bull. Am. Phys. soc. 11(1966)30.

DAN72 S.D.Angelo, F.de Nataristefani and P.Monacelli Nucl. Instr. and Meth. 103(1972)197.

DEH65 D.Dehnbard, D.S.Gemmel, and Z.Vager, Bull. Am. Phy. Soc. 10(1965)602.

DEN63 L.J.Denes and W.W.Daehnick, Bull. Am. Phys. Soc. 8(1963)25.

DEN65 L.J.Denes and W.W.Daehnick, Bull. Am. Phys. Soc. 10(1965)120.

DEN66 L.J.Denes, W.W.Daehnick and R.M.Drisko, Phys. Rev. 148(1966)1097.

DEN67 L.J.Denes and W.W.Daehnick, Phys. Rev. 154(1967)928.

DEV71 R.M.De Vires U.C.L.A. PHD dissertation (1971).

DON64 P.F.Donovan, J.V.Kane, C.Zupanciic, C.P.Baker and J.F.Mollenauer, Phys. Rev. 135(1964)B61.

DRA71 O.Dragim, G.G.Dussel, E.Magueda and R.P.J.Perazzo, Nucl. Phys. A167(1971)529.

EIC70 W.Eichelberger, R.D.Plieninger and E.Velten, Nucl. Phys. A149(1970)441.

EPS71 M.B.Epstein, J.R.Quinn, S.N.Bunker, J.W.Verba and J.R.Richardson, Nucl. Phys. A169(1971)337.

FER50 E.Fermi, "Nuclear Physics" P.142 (University of Chicago Press, Chicago, 1950).

GAL66 H.J.Gale and J.A.B.Gibson, J. Sci. Instr. 43(1966)224.

GAR52 G.F.J.Garlick and G.T.Wright, Phys. Soc. Proc. SeriesB65(1952)415.

GEM64 D.S.Gemmell, J.R.Erskine, and J.P.Schiffer, Phys. Rev. 134(1964)B110.

GER65 J.B.Gerhart, P.Mizera and F.W.Slee, Bull. Am. Phys. Soc. 10(1965)461.

GOO60 T.J.Gooding and H.G.Pugh, Nucl. Instr. and Meth. 7(1960) 189.

GOU64 F.S.Goulding, D.A.Landis, J.Cerny, R.H.Pehl, IEEE Trans. of Nuclear Science NS-11(1964) 388.

IGO63 G.Igo, L.F.Hansen, and T.J.Gooding, Phys. Rev. 131(1963) 337.

JAC70 D.F.Jackson "Nuclear Reactions" Chapter 9 (Methuen and Co. Ltd. 1970).

JAM63 A.N.James and N.G.Pugh, Nucl. Phys. 42(1963) 441.

JAY68 K.S.Jayaraman and H.D.Holmgren, Phys. Rev. 172(1968) 1015.

KEI70 G.Keil Nucl. Instr. and Meth. 89(1970) 111.

KUD65 Yu.A.Kudijarov, S.Matthies, V.G.Neudatchiu, and Yu.F.Smirvo, Nucl. Phys. 65(1965) 529.

KUI66 P.Kuijper, C.J.Tiesinga and C.C.Jonker, Nucl. Instr. and Meth. 42(1966) 56.

LAU66 T.Lauritsen and F.Ajzenberg-Selove, Nucl. Phys. 78(1966) 1.

MAT63 S.Matthies, V.G.Neudatchiu and Yu.F.Smirnov, Nucl. Phys. 49(1963) 97.

MCG71 R.L.McGrath, D.L.Hendric, E.A.McClatchie, B.G. Harvey and J.Cerny, Phys. Lett. 34(1971) 289.

MID68 R.Middleton, B.Rosener, D.J.Pullen, and I.Polsky, Phys. Rev. Lett. 20(1968) 118.

NEU65 V.G.Neudatchin and Yu.F.Smirov, Nucl. Physics 66(1965) 26.

NYB64 P.Nyborg and O.Skjeggestad, "Notes on Phase Space" in "Kinematics and Multiparticle Systems". Ed. M.Nikolic, (Gordon and Breach, 1964).

PER56 J.K.Pering and T.H.R.Skyrme, Proc. Phys. Soc. A69(1956) 600.

PIR74 C.Pirart, M.Boseman, P.Leleux, P.C.Macq, and J.P. Meulders, Phys. Rev. C10(1974) 651.

POT60 R.J.Potter and R.E.Hopkins IEEE Trans. Nucl. Sci. NS-7(60) 150.

SAK65 Y.Sakamoto, Nucl. Phys. 66(1965)531.

SAT64 G.R.Satchler, Proceedings of the Symposium on Nuclear Spectroscopy with Direct Reactions, Argonne 1964. Argonne National Laboratory Report ANL6878(1964).

SCH68 L.I.Schiff, "Quantum Mechanics", third edition. P.286(McGraw-Hill 1968).

SHE60 R.K.Sheline and K.Wildermuth, Nucl. Phys. 21(1960)196.

SHU49 W.A.Shurcliff, and R.C.Jones, J. Opt. Soc. Am. 39(1949)912. CERN Report 64-13(1964).

VAN73 W.T.H.Van Oers, M.Jain, S.N.Bunker, Nucl. Instr. and Meth. 112(1973)405.

WIL58 K.Wildermuth and T. Kananopolous
Nucl. Phys. 7(1958)150.
Nucl. Phys. 9(1958)449.

WIL66 K.Wildermuth and W.McClure, "Springer Tracts in Mordern Physics", Vol. 41. Ed. G.Hohler (Springer Verlag, Berlin-Vienna, 1966).

WRI53 G.T.Wright, Phys. Rev. 91(1953)1282.

Appendix

The Monte Carlo Method

The Monte Carlo method is used to reproduce the distribution of any function $\phi(x)$ on the x axis using random numbers. There are two classes of functions, namely, (1) the functions which cannot be integrated analytically, and (2) the functions which can be integrated analytically. These two classes of functions will be discussed separately in this Appendix.

Class (1) Functions:

Let x be any value between a minimum value, x_0, and a maximum value, x_{MAX}. $\phi(x)$ is then the value corresponding to x, and can take on values between ϕ_0 and ϕ_{MAX}, where ϕ_0 and ϕ_{MAX} are the minimum and the maximum values of $\phi(x)$ respectively as shown in Fig.A.1a. If a random number R_1 is chosen between 0 and 1, then there is a corresponding value of x_1 given by:

$$x_1 = R_1 (x_{MAX}) + (1-R_1) x_0 \qquad (A.1)$$

If a second random number R_2 is also chosen between 0 and 1, then a corresponding ϕ_{CAL} can be expressed as:

$$\phi_{CAL} = R_2 \phi_{MAX} + (1-R_2)\phi_0 \qquad (A.2)$$

Now with the x_1 value generated by equation (A.1), the

Fig. A. 1a

An arbitrary function $\phi(x)$.

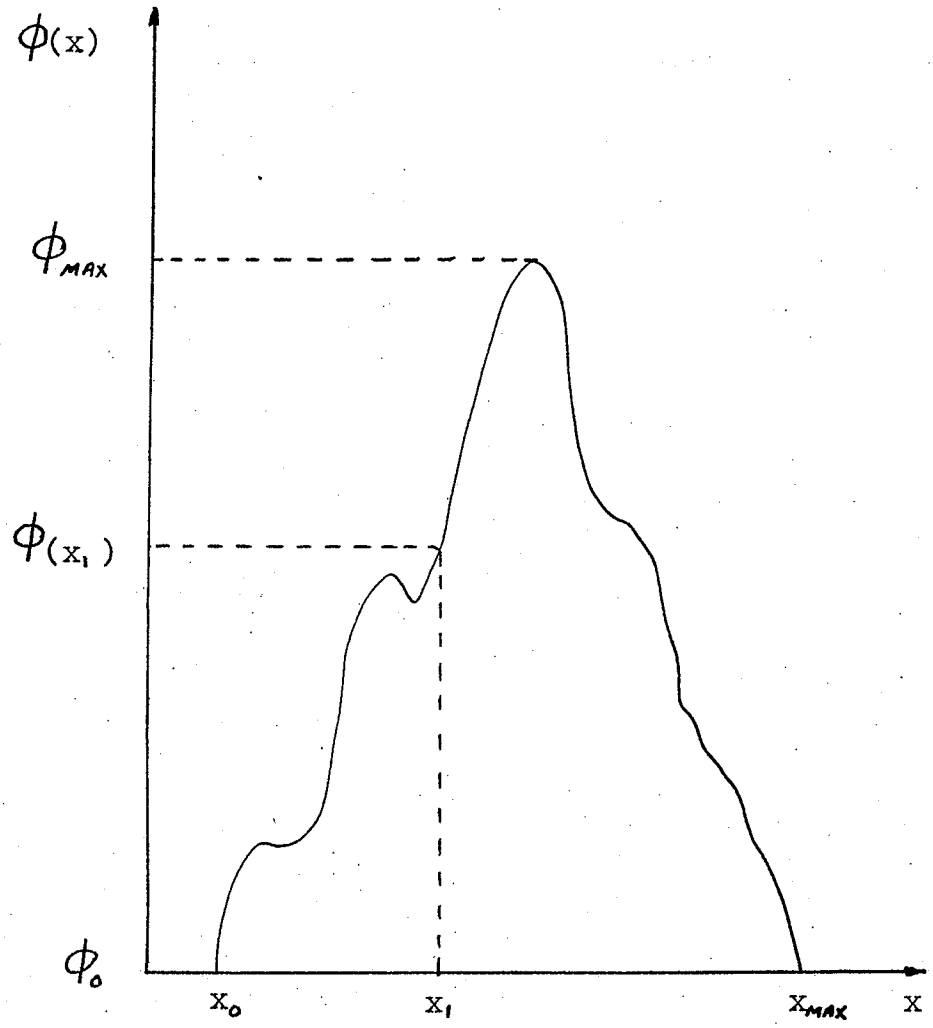
$\phi(x)$
ϕ_{MAX}
$\phi_{(x_1)}$
ϕ_0
x_0
x_1
x_{MAX}
x

value $\phi(x_1)$ can be calculated. Only the events with the following condition are accepted:

$$\phi_{CAL} \leq \phi(x_1) \qquad \text{(A.2b)}$$

The distribution of $\phi(x)$ on the x axis can be reproduced if many of different random numbers are generated. If only the events satisfying the condition imposed by equation (A.2b) are plotted, then the distribution of the numbers of events as a function of x has the form of $\phi(x)$. The distribution of ^{5}Li masses can be used as an example. Equation (3.2) gives the distribution of the ^{5}Li masses as

$$F(\Delta M^5_{Li}) = F_0 e^{-(\Delta M^5_{Li}/\Delta E)^2} \qquad (3.1)$$

If ΔM^5_{Li} has a cut-off width of 3 Mev, ΔE is obtained from equation (3.1), and F_0 corresponds to the maximum value of F, then ΔM^5_{Li} can be generated by using equation (A.1)

$$\Delta M^5_{Li} = R_1 \Delta M^5_{Li\,MAX} + (1-R_1)\Delta M^5_{Li_0} \qquad \text{(A.3)}$$

Here $\Delta M^5_{Li\,MAX}$ and $\Delta M^5_{Li_0}$ are the maximum and the minimum values of ΔM^5_{Li} allowed for practical reasons by the programmer. This value of ΔM^5_{Li} can then be substituted into equation (3.2) to obtain a value $F(\Delta M^5_{Li})$. Now a second random number R_2 is used to generate a F value according to equation (A.2):

$$F_{CAL} = R_2 F_o \qquad (A.4)$$

In this case the minimum value of F is assumed to be negigible. The value F_{CAL} is then compared to $F(\Delta M^2_{Li})$ obtained from equation (3.2). The distribution of the ΔM^2_{Li} obtained from the Monte Carlo calculation is shown in Fig.A.1b.

Class (2) Functions:

If the function $\phi(x)$ can be integrated, then a different technique can be used to generate values of x with the distribution of $\phi(x)$. The probability that events occur in a range dx centred about x as shown in Fig.A.2a is $\phi(x)\,dx$. This probability can be transferred into a rectangular distribution N(R) of the random number R as shown in Fig.A.1b. The area of the corresponding bars in the two figures should be the same. Since N(R) is a constant (=c say), and the areas are the same, then

$$\begin{aligned} N(R)\,dR &= \phi(x)\,dx \\ \int_0^{R_1} c\,dR &= \int_{x_0}^{x_1} \phi(x)\,dx \\ cR_1 &= \int_{x_0}^{x_1} \phi(x)\,dx \end{aligned} \qquad (A.5)$$

Since the upper limit of R is 1, and this corresponds to $x=x_{MAX}$, then

$$c = \int_{x_0}^{x_{MAX}} \phi(x)\,dx \qquad (A.6)$$

When (A.5) and (A.6) are combined:

Fig.A.1b

The distribution of $\Delta M\Sigma_i$.

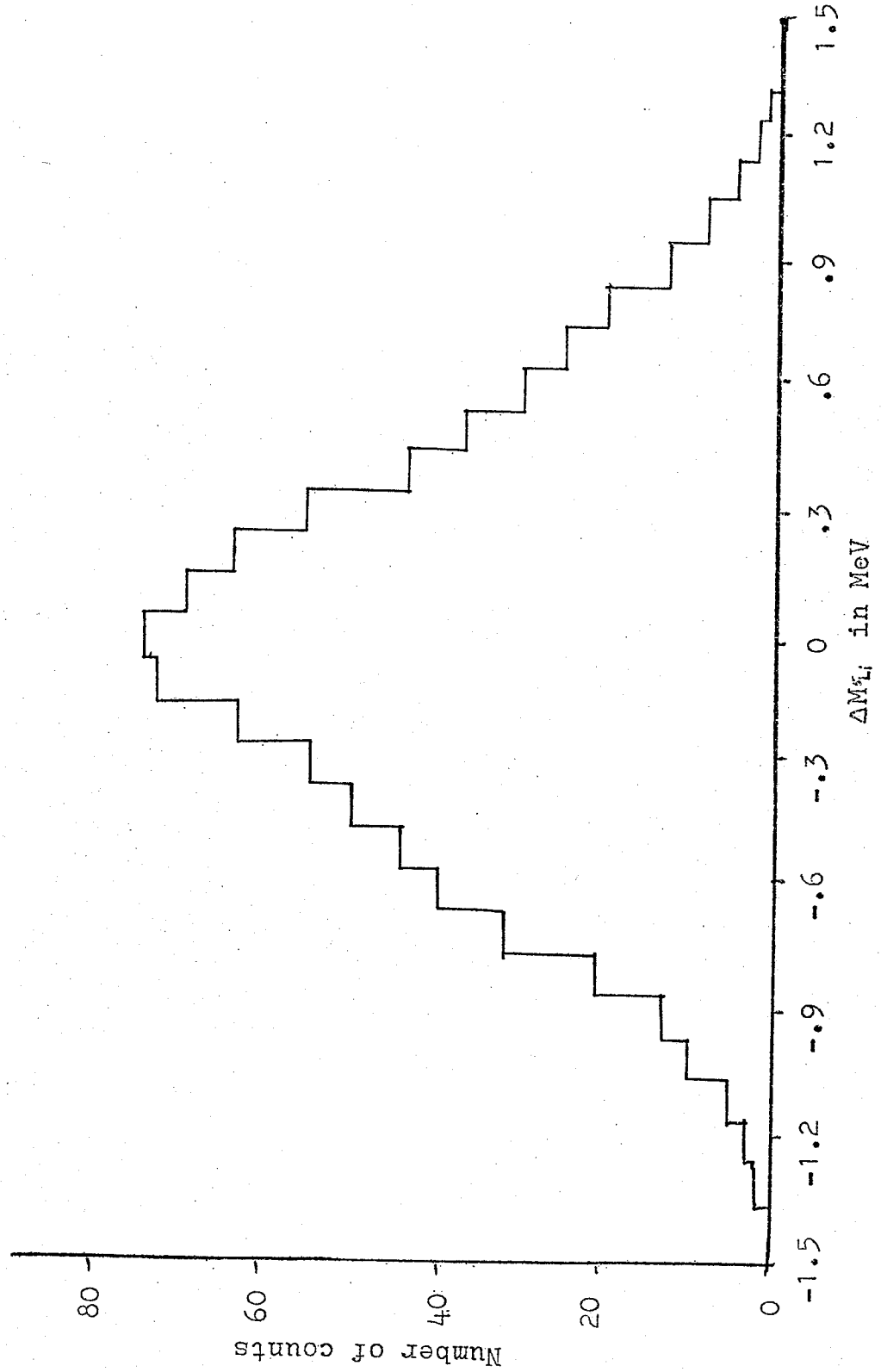
Number of counts
0
20
40
60
80
-1.5
-1.2
-.9
-.6
-.3
0
.3
.6
.9
1.2
1.5
$\Delta M_{^6Li}$ in MeV

Fig.A.2a

An arbitrary distribution $\phi(x)$.

Fig.A.2b

$\phi(x)$ is transferred to a rectangular distribution N(R). The areas inside the bars of Fig.A.2a and A.2b are the same.

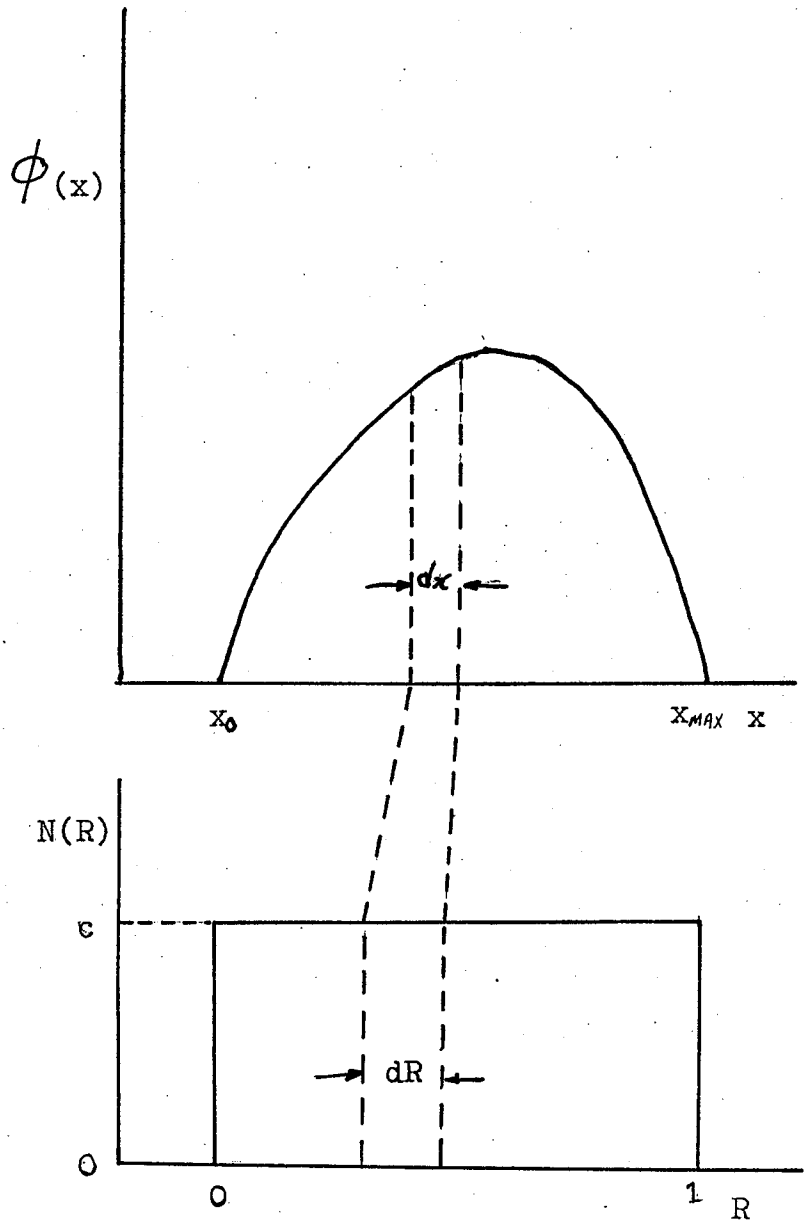
$\phi_{(x)}$
dx
X_0
X_{MAX} X
N(R)
c
dR
0
0
1
R

$$R_1 = \frac{\int_{x_0}^{x_1} \phi(x)\,dx}{\int_{x_0}^{x_{MAX}} \phi(x)\,dx} \qquad (A.7)$$

Using $\Phi(x) = \int \phi(x)\,dx$

then $\Phi(x_1) - \Phi(x_0) = R_1\Phi(x_{MAX}) - R_1\Phi(x_0)$

and $\Phi(x_1) = (1-R_1)\Phi(x_0) + R_1\Phi(x_{MAX})$

Therefore $x_1 = \Phi^{-1}\left[(1-R_1)\Phi(x_0) + R_1\Phi(x_{MAX})\right] \qquad (A.8)$

has the same distribution as $\phi(x)$ when R_1 is uniformly distributed in the interval 0 to 1.

By way of example consider the generation of the proton angle in the ^{5}Li breakup frame. Since the ^{5}Li is assumed to break up isotropically in this frame, the distribution of the number of protons as a function of θ_p' is proportional to $\sin\theta_p'$, i.e. $\phi(\theta_p') \propto \sin\theta_p'$. By using equation (A.8), the C.M. angle of the proton is related to a uniformly distributed random number R by

$$\cos\theta_p' = (1.0-R)\cos\theta_{p_0}' + R\cos\theta_{p_{MAX}}' \qquad (A.9)$$

or $$\theta_p' = \cos^{-1}\left[(1.0-R)\cos\theta_{p_0}' + R\cos\theta_{p_{MAX}}'\right]$$